## Department of Precision and Microsystems Engineering

Polymer nano manufacturing of a biomimicking surface used for kidney stone crystallization studies.

R.M.B. Pleeging

Report no   : 2019.003
Coach   : Dr. L. Sasso, Prof. Dr. Urs Stauffer
Professor   : Prof. Dr. Urs Stauffer
Specialisation : Micro and Nano Engineering
Type of report : Msc Thesis
Date   : 8 February 2019

TU**Delft** Delft University of Technology

Challenge the future
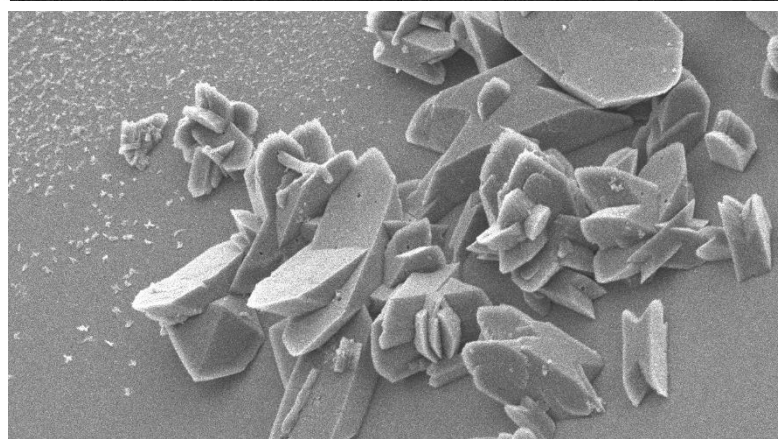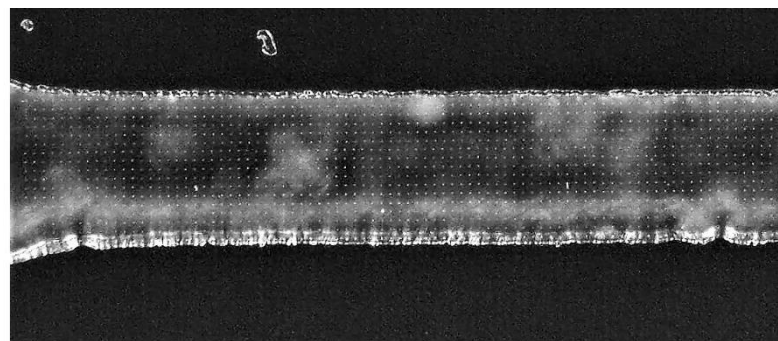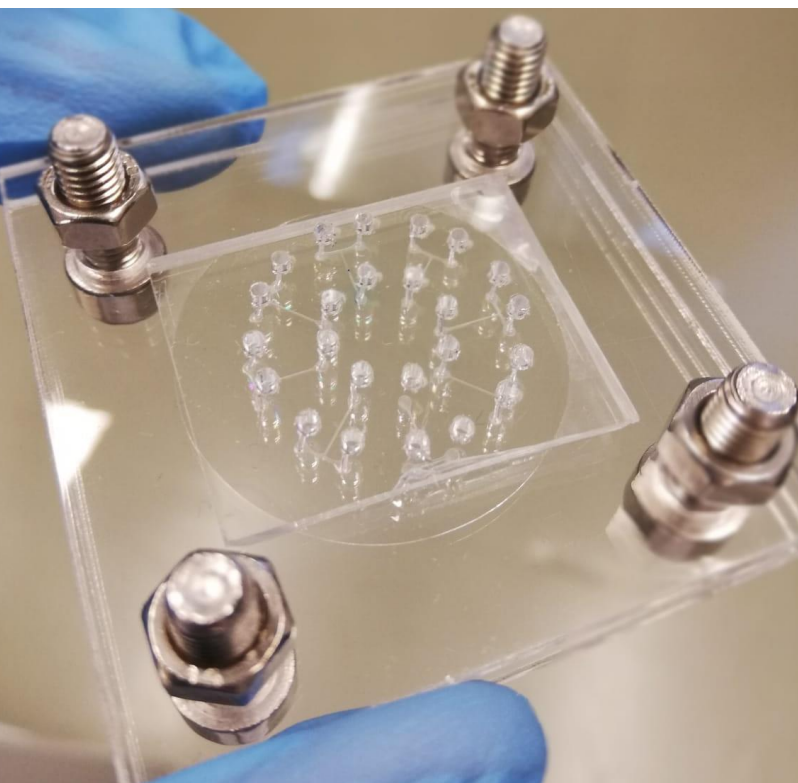
Polymer Nano Manufacturing of a Biomimicking Surface used for Kidney Stone Studies

by

R.M.B. Pleeging

to obtain the degree of Master of Science
at the Delft University of Technology,
to be defended on Friday February 8, 2019.

ŤUDelft

Preface

Before you lies the master thesis titled "Polymer nano manufacturing of a biomimicking surface used for kidney stone crystallization studies", the result of a year's work. During that year I developed a microfluidic device with incorporated surface morphologies that was used to crystallize calcium oxalate, the most common type of kidney stone. I would not have been able to do all the work presented in this report without the people that helped me, for which I am very grateful and who I would like to thank.

Our lab technicians Rob Luttjeboer, Harry Jansen, Patrick van Holst for giving me advice and train me to use the equipment. Special thanks to Spiridon van Veldhoven who allowed me to use a new 3D printing membrane to ensure that I could always produce good quality molds. He also designed and fabricated a custom sample holder for the critical point dryer, a machine also specially installed by the technicians. Burak Eral, Fatma Ibis, Sanan Suleymanli, Tsun Wang Yu and Priya Dhand of the Process & Energy Department for their help and thoughts regarding crystallization, preparing precursor solutions, showing me around the equipment and most of all for accepting me in their group. All my friends, family and colleagues who supported me during this research. Miranda Looman for her continuous support personally, technically and contentwise. Abhishek Sharma for his advice and teaching me countless tricks for the equipment. Justin Smid, Gijs van der Velden, Marc de Graaf and Ad Huisjes for making our office a joyful place. Luigi Sasso for his great supervision, motivation and tutoring for the most part of this research and Daniel Fan for his guidance and help during the last couple months. Urs Stauffer for taking up the supervision, listening to my findings and ideas and steering me to find the essence of the matters we discussed.

In this report I tried to capture most of my thoughts, experiments, results and conclusions. The report starts off with part of the literature study presented as an introductory chapter. This is followed by an extensive chapter on the fabrication theory. Then the epitome of this work is presented in the form of a Technical note, written in the style of and hoped to be published in the IOP Journal of Micromechanics and Microengineering. In Chapter 4 the method and results for the two-photon polymerization experiments are presented and discussed, followed by a chapter in which the stability of our structures is investigated. Chapter 6 is dedicated to the microfluidic device that was manufactured and tested. A conclusive chapter ends the main matter of this thesis. The report is closed with a personal reflection on the research. Most chapters have a corresponding appendix chapter aimed to provide more information on the particular matter.

R.M.B. Pleeging
Delft, January 23, 2019

Contents

List of Figures

List of Tables

<div style="text-align: right">

Chapter 1

Introduction

</div>

1.1. Motivation

The prevalence and incidence of kidney stone formation is increasing across the globe [1]. By the time a person reaches the age of 70, 11.0% of men will have had a kidney stone, against 5.6% of women [2]. In the United States, kidney stones cost over $5 billion annually in the private sector [3]. This includes both direct causes like hospitalization, as indirect causes like lost work time. As prevalence is increasing, these costs will only grow. The formation of kidney stones has both genetic and environmental factors [1]. Changes in genetics take a long time to appear and can not really explain the increased prevalence. Environmental factors are more likely to have caused this grow. Luckily the environment can be changed, i.e. changing your diet. Understanding of what exactly contributes to the formation of kidney stones is therefore of utmost importance.

Kidney stone disease is a major issue worldwide and it has been around for millennia, with the oldest descriptions of its symptoms and treatment dating back to the ancient Egyptians and Mesopotamia (around 3000 BCE) [4, 5]. The exact mechanisms that are involved in the formation of kidney stones are however still not fully understood. Most knowledge so far has been acquired by endoscopic examinations, biopsies and investigation of removed stones.

Nowadays, to study pathophysiology while circumventing the use of animals or material obtained from biopsies, the fabrication of fully functioning *in vitro* organs is pursued. Such an organ-on-chip (OOC) should be able to mimic the micro-environment *in vivo*, having critical tissue-tissue interfaces, spatiotemporal chemical gradients, and dynamic mechanical environments [6]. Previous research on kidney-on-chip (KOC) focused mainly on fabricating scaffolds, recreating the microfluidic properties and transitioning to more complex systems [7–9]. These studies have the goal of making a KOC that incorporates cells, to study drug delivery or nephrotoxicity. The literature on mimicking the kidney to study crystallization mechanisms is to our knowledge very scarce.

Studies on surface-induced crystallization and crystal nucleation have shown that surface morphology can play an important role in the rate at which crystals nucleate [10, 11]. If we want to apply these findings to the crystallization of kidney stones, a totally different kind of KOC is needed. This KOC should contain controlled morphological structures on a much smaller scale than individual cells, which are normally incorporated in OOC's. The goal of this research is to end up with an artificial kidney that has the same surface morphology as its biological counterpart. With this artificial kidney the relation of the microstructures of the kidney with the crystallization mechanisms that occur can be studied.

1.2. Biological background

1.2.1. Anatomy of the kidney

The kidney is a complex organ that plays many roles in the body. It regulates blood volume and pressure, osmolarity in the body and it produces many enzymes and hormones. Its most important role is filtering the blood plasma and eliminating waste.

The functional unit of the kidney is called the nephron and it is found in two parts of the kidney, the renal cortex and the renal medulla. The cortex has renal columns extending into the medulla, dividing it into renal pyramids. These pyramids end in a blunt point which is called the renal papilla. The papilla is the endpoint of the nephron. Urine drips out from the renal papilla, which is covered by a cap called the minor calyx,

collecting the urine. Several minor calyces meet and form the major calyx. Several major calyces converge into the renal pelvis. From here the urine leaves the kidney through the ureter. These different parts can be found in Fig 1.1a.

1.2.2. Anatomy of the nephron

The functional unit of the kidney consists of two main components:

- **Glomerus**: The filtering unit, letting fluid and waste products through but prevents blood cells and large molecules from passing.

- **Tubules**: The filtered fluid passes through several tubules, where water and other substances are reabsorbed.

The nephron consists of several tubules (see Fig 1.1b) through which the filtered fluid journeys and ultimately transforms to urine by the process known as tubular reabsorption. The fluid passes four distinct sections in the nephron:

1. The fluid that is filtered from the blood leaves the glomerus and enters the proximal convoluted tubule (PCT). The PCT is the part of the nephron where the largest variety of substances is reabsorbed: water, amino acids, glucose and ions [12].

   The PCT is lined with cuboidal epithelial cells. At the apical domain the cell membrane contains many microscopic protrusions, microvilli, which form a so called brush border. It increases the surface area of the cell membrane significantly which is beneficial for tubular reabsorption [13].

2. The fluid then enters the nephron loop, also known as the Loop of Henle. It can be divided into several areas, the descending limb and the ascending limb, each in turn consisting of a thin segment and a thick segment. Ions are actively transported through the membranes of the thick segments of the loop of Henle into the medullary interstitium, and they are impermeable to water. This causes the renal medulla to have a very high salinity with respect to the renal cortex. The thin segments lie in the renal medulla and they are very permeable to water. Because of the saline environment, water is passively transported into the medullary interstitium. Because the descending and ascending limbs flow in an opposite direction with respect to each other, they form a counter-current exchange system [12]. By changing the osmolarity of the renal medulla, the body can reabsorb more or less water based on the person's hydration.

   The thick descending limb of Henle is a continuation of the PCT. The thin segments are lined with squameous simple epithelium, which are flat epithelial cells that can provide rapid diffusion. The cell membrane does not contain protrusions. Just as the thick descending limb is a continuation of the PCT, the thick ascending limb is a continuation of the distal convoluted tubule [13].

3. The fluid flows into the distal convoluted tubule (DCT). This is the last part of the nephron. Here a variable amount of water and salts is reabsorbed, regulated by hormones like antidiuretic hormone [12].

   The DCT is lined with cuboidal epithelial cells, which are shorter than those of the PCT and do not have a distinguished brush border. They do have sparse microvilli. [13].

4. Several DCT's end up in the collecting duct (CD). Several collecting ducts merge into a papillary duct. At the end of each renal papilla, about 30 papillary ducts end and urine drains from there into the renal calyx [12].

   The CD is lined with cuboidal epithelium, but two distinct cell types can be distinguished. The majority of cells are principal cells containing one or two apical primary cilia, large protrusions from the cell which act as mechanosensors [14] or chemosensors [15]. The other cells are intercalated cells containing a brush border of short microvilli on the apical domain [13, 16].

(a)

(b)
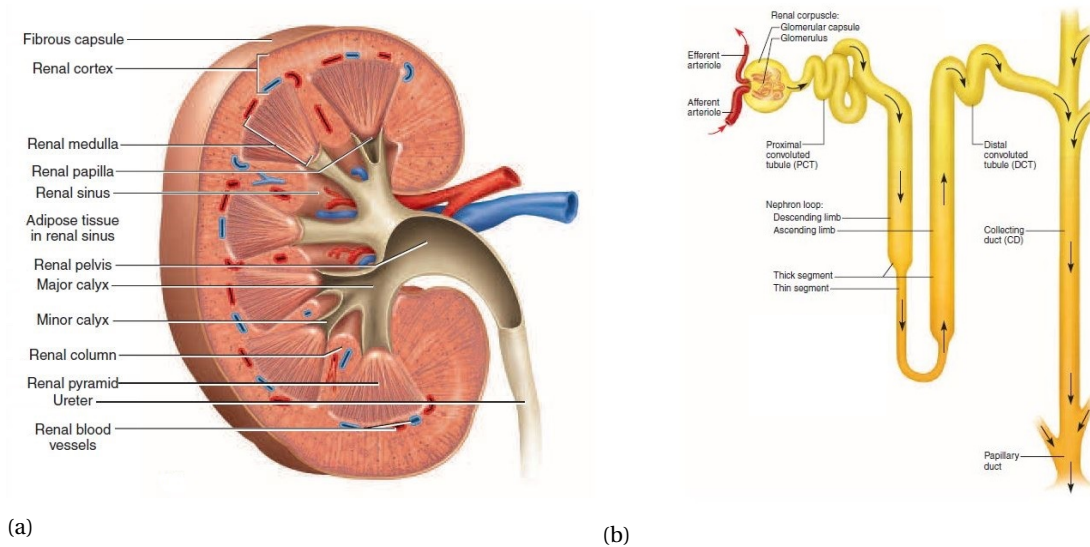
Figure 1.1: Anatomy of a) the kidney and b) the nephron, reproduced from [12].

1.2.3. Microvilli and cilia

As described, the cells lining the nephron contain cell membrane protrusions in the form of microvilli or cilia. Microvilli contain a core bundle of 20-30 actin filaments, enclosed by the cell membrane [13]. The Young's modulus of an individual actin filament was calculated in one research to be approximately 0.144 GPa with an uncertainty of one order of magnitude [17] and calculated in a second research to be approximately 1.8 GPa [18]. Based on this, the Young's modulus of a microvillus is assumed to be in the order of magnitude of about 1 GPa. Furthermore microvilli are not static structures but they exhibit a dynamic life: they grow and their length is regulated during their life-cycle [19]. Cilia consist of microtubules [13] which have a Young's modulus similar to that of the actin filaments of which the microvillus is constructed [20, 21]. Therefore the Young's modulus of a cilium is also assumed to be in the order of magnitude of 1 GPa.

Renal microvilli typically have a size of about 80 nm in diameter [13] and 1-3 μm in height [12]. A well developed brush border contains microvilli of about this size, packed in a dense hexagonal array with a remarkable uniformity in height and spacing [17, 22]. The spacing between microvilli varies with the flow rate, and is about 75 to 130 nm in the brush border [23, 24]. Microvilli can also appear as small bumps on the cell surface [16] having a relatively short length of 500 nm or less [25]. The cilium is much larger, having a diameter of about 250 nm [13] and a height of 7-10 μm [12]. In table 1.1 the dimensions for the different microprojections on the epithelial cells of the nephron are summarized.

1.2.4. Kidney stones

It is possible that a solid piece of material forms in the kidneys, a renal calculus or kidney stone. The formation of such renal calculi is called nephrolithiasis or kidney stone disease. A lot of factors play a role in the formation of kidney stones, but the main contributor is a high concentration of minerals in the urine. The mineral crystallizes, the crystals agglomerate and they form small stones. Under certain circumstances larger kidney stones can grow from there.

It is important to note that there are different types of kidney stones, named after the material that is crystallized. Very often, kidney stones contain several materials and not a specific one. Because most of the time small amounts of other crystal do not play an important role, the stone is named after its main component [26]. The different types of kidney stones are discussed in Appendix G.

The stones that are most often found, in approximately 80% of the cases, are calcium stones. Within the group of calcium stones, almost 90% is made of calcium oxalate [27]. Calcium oxalate monohydrate (COM) is the dominant form and appears more often than calcium oxalate dihydrate (COD). The majority of people who

Table 1.1: Type and dimensions of the microprojections on the apical domain of the epithelial cells in the nephron (diameter d, height h, spacing s).

Nephron segment	Type	d [nm]	h [μm]	s [nm]
PCT	brush border of microvilli [13]	80 [13]	1-3 [12]	75-130 [23, 24]
Thin segments of the loop of Henle	none [13]	-	-	-
DCT	sparse microvilli [13]	80 [13]	<0.5 [16]	varying [13, 19]
CD	primary cilium [13]	250 [13]	7-10 [12]	8000 [13]
	brush border of microvilli [13]	80 [13]	<0.5 [16]	75-130 [23, 24]

form COM stones show no systematic disease that causes the stones, and these people are named 'idiopathic calcium oxalate stone formers' (ICSF). It is therefore logical that most research is aimed at this particular stone forming group. COM crystalluria is found both in stone formers and healthy persons. The difference lies in the size of the crystals. Healthy people excrete mostly small particles, smaller than 12 μm, whereas ICSF show a much larger amount of bigger particles in their excretion, larger than 12 μm [28]. It was tested if supersaturation alone could explain this difference, but it was found that this was not the case. The possible explanation is that stone formers have less inhibitory factors that prevent crystal agglomeration than healthy subjects [28]. Another study showed that a high intake of animal proteins or sodium decrease the inhibitory ability of urine to calcium oxalate crystal agglomeration, giving a physiochemical explanation for this change in inhibition [29].

Everybody has crystalluria, but if crystals in the urine are small enough, they can pass harmlessly [28]. Crystal retention is the problem because the longer crystal aggregates can stay in supersaturated urine, the bigger they can grow, eventually leading to the size of stones. It can be imagined that if a crystal agglomerate grows too large, it can get stuck within a renal tubule. It was calculated that with the normal travel time through the kidney this indeed could happen [30]. The highest risk of happening is at the end of the collecting ducts that come from a nephron with a long loop of Henle or at the upward-draining sections of the nephron. This type of stone formation is known as free particle formation [31]. Fixed particle formation means that crystals adhere to a surface which acts as a nidus for the stone. A proposed mechanism for this fixed particle formation is that calcium oxalate crystals prefer to bind to regenerating or re-differentiating renal tubular cells, and that several crystal-binding molecules that are expressed at the luminal surface of these cells play an important role in this process [32]. This mechanism would lead to tubular nephrocalcinosis, the calcification of the renal tubules, and it should not be confused with interstitial nephrocalcinosis, calcification of the interstitium. The latter starts as precipitation of calcium phosphate in the basement membranes of the thin loops of Henle [33] expanding into the interstitium and eventually breaching the epithelial layer where it gets exposed to urine, where it acts as a nidus on which a stone can grow [34]. This type of calcification forms a hydroxyapatite (HA) plaque which is known as Randall's Plaque (RP).

Back in 1937 Alexander Randall made the original observation that kidney stones grow attached to these calcium phosphate plaques on the renal papilla [35–37]. Much later the direct correlation between the presence of RP and the occurrence of calcium stones was made [38]. Almost 10 years later, by studying stones that were obtained by percutaneous nephrolithosomy on ICSF patients, it was found that almost all attached stones were attached to RP [39]. By further studying the unattached stones, using morphological observations and micro-CT analysis, it was found that unattached stones had originated as attached stones to RP [40]. This leads to the conclusion that the primary growth of COM stones is on RP.

1.3. Approach to solution

As crystal nucleation often initiates at liquid-solid interfaces [41], study shows that certain morphological features on the surface of that interface can influence nucleation rates [10]. Diao et al used polymer films with differently shaped nanopores to study the effects on the crystallization of aspirin. They found that angular nanopores with a 15-120 nm diameter promoted nucleation, whereas spherical nanopores of the same size slowed down nucleation [11]. It seems that different morphological nanostructures can have varying effects on the nucleation rates of a crystal. In Section 1.2.3 it was described how the nephron also contains different morphological nanostructures. This research is aimed at studying the relationship between these structures and the crystallization of the most common type of kidney stone, calcium oxalate monohydrate (COM). Surface morphology is not the only factor playing a role in kidney stone crystallization. When zooming out and looking at the eventual goal of building an artificial kidney to study COM crystal formation mechanisms, more work is needed. Each step, listed *i-iv*, operates in a different field of study. Steps *i, ii* and *iii* focus on the nucleation and growth of COM crystals, whereas step *iv* is about crystal retention and stone growth.

  i *Nano fabrication*: Fabricating nanopillars from a polymer.
  COM stone formation starts with crystals nucleation in the nephron. Different segments of the nephron show different morphologies in the form of various microprojections on the cell membranes. These microprojections can be approximated as small pillars of varying length, diameter and spacing. By fabricating nanopillar arrays we can mimic these microprojections. To mimic the mechanical behavior of the microvilli and cilia, a material will be chosen that has a similar Young's modulus. This value is in the order of magnitude of 1 GPa, which leads to the material family of polymers [42]. Polymers are especially favorable due to their low cost, as well as the abundance of polymer micro- and nanofabrication methods [43, 44]. Furthermore they have already shown great promise in a lot of fields, including tissue engineering [45], microfluidic devices [46] and bioinspired materials [47].

  ii *Microfluidics*: Combining the different segments into a microfluidic chip.
  Organ-on-chip (OOC) technology enables us to mimic the microenvironmental conditions present *in vivo*, providing an opportunity to study the formation of kidney stones *in vitro*. A recent study has tried to capture some of the physiological conditions of the kidney in a biomimetic model to study kidney stone crystallization [48]. In that study Lafitte et al. proposed a microfluidic channel with dimensions matching the collecting duct of the human kidney, using physiological concentrations and flow rates. If we can include different surface morphologies in the microfluidic channel, this approach can be used to study the effect of the kidney surface morphology on crystallization of kidney stones.

  Furthermore it was found that certain diseases can drastically change the morphology inside the kidney, for example cause a partial or complete loss of the brush border in the PCT [49–52]. With a microfluidic chip these morphological changes inside the nephron can easily be reproduced and its effect can be studied.

  iii *Bio*: Functionalizing the surface with cell membrane proteins.
  From previous studies it was found that proteins in the body play a role in crystal formation or inhibition [29, 32]. To fully capture the crystallization mechanisms inside the kidney, adding these proteins to the model is therefore important.

  iv *Chem*: Covering a surface with Randall's Plaque.
  Randall's Plaque (RP) has shown to be the major factor in COM crystal retention leading to stone formation [38–40]. Covering a surface with RP and studying how COM crystals attach and grow from such a surface is therefore important and worthy to investigate.

Step *i*, which focuses on mimicking the nephron surface, is the logical starting point in the fabrication of the artificial kidney, because these surfaces have to be created in the first place. After step *i*, the steps *ii, iii* and *iv* can be chosen arbitrarily, as they focus on different aspects that play a role in crystal formation.

This research will focus on step *i* and *ii*: the fabrication of the different surface morphologies that mimic those found in the nephron, and combining them to build a microfluidic chip. This leaves step *iii* and *iv* for future work.

1.4. State of art: fabrication of polymer nanopillars

In this research the microprojections are approximated as nanopillars. The brush border is known to have a uniformity in height and packing density. The microvilli in the DCT are sparse, and because they experience a life cycle, the surface will constantly look different. A microvillus in one place will disappear whereas in another place a microvillus will appear. Over a larger area containing a great number of pillars, these changes average out. Therefore the surface of the DCT is assumed to contain a sparse but uniform packing density of microvilli.

The dimensions of the microprojections were summarized in Table 1.1. Based on this table, the fabrication method should be able to achieve nanopillars with:

- small diameters of 80 nm.

- varying aspect ratio's (AR), from 6 to 40.

- varying spacing distances, from as little as 75 nm to as big as 8 μm.

1.4.1. Methods

There is a plethora of literature to find on the fabrication of nanopillars and they contain a large variety of methods. Most used are methods like replica molding and nanoimprint techniques, which are already well established in polymer microfabrication [46]. A summary of nanopillar fabrication methods is presented in Table 1.2.

It has to be noted that the dimensions of the nanopillars mentioned in Table 1.2 are case-specific values, and do not represent the technique to its full extend. It would for example be possible, in the case of [53], to spin coat a thicker layer of SU-8 and subsequently etch, resulting in pillars of a greater height. The data gives however an indication of the possibilities that the particular technique offers.

Between the different methods, there is a lot of variety in the number of fabrication steps that have to be performed and the amount of equipment that is needed in order to obtain the end product. Because a large variety in dimensions is needed, not all fabrication methods will be suitable. Replica molding and nanoimprinting require a master mold or stamp with either a positive or negative imprint of the product. A common method makes use of the neat and controllable mechanism of highly uniform and hexagonally ordered nanopore formation in anodic aluminium oxide (AAO) to make the master [54–56]. For each design a separate master has to be made. The same holds for electron beam lithography that uses a mask to etch into a spin coated polymer film. When having to create a large variety of structures it is not convenient when for each structure a master or mask has to be made, or when a lot of fabrication steps and equipment is needed. On the other hand, the techniques that are mentioned do fulfill the dimensional requirements.

Table 1.2: Fabrication of nanopillars in literature, with *d* (pillar diameter), *h* (pillar height), *s* (pillar-to-pillar spacing), PUA (polyurethane acrylate), PMMA (poly(methyl methacrylate)), SU-8 photoresist, PETIA (pentaerythritol triacrylate), NPS (nanoengineered polystyrene), PDMS (polydimethylsiloxane), h-PDMS (hard polydimethylsiloxane), PU (polyurethane), AAO (anodic aluminum oxide).

Method		d [nm]	h [nm]	s [nm]	Material	Advantages	Disadvantages	Reference
Replica molding	Use AAO template as mold	45-200	40-2.000	60-300	PUA; h-PDMS; PU; TC-1622 epoxy	Controllable pore diameter and length	Bigger height means bigger diameter	[57] [58] [59]
	Use PDMS intermediate mold	500	9000	400	Epoxy DER 354; PDMS	PDMS mold is inexpensive and can be used multiple times	PDMS nanopillars can only have low AR of 6	[60]
Nanoimprint	Use a master to create stamp	50-200	150-600	50-300	SU-8; NPS	Controlled diameter and spacing; mass-replication technique	Lots of techniques used	[61] [62] [63]
	Use nanospheres to create stamp	100	1000	400	SU-8; PMMA	Periodicity and size of nanostructure independently controlled	Lots of techniques used	[64]
	Nanoimprint and pull stamp	450	19.000	~1000	PMMA	Create slanted pillars (70°); High AR (20-40)	Pull stamp with controlled speed	[65]
Phase separation	Spin coat polymer blend; Remove one polymer	200	300	~500	PMMA	Controllable shape, size and distribiution	Very low AR	[66]
Electron beam lithography	Etch a spin coated SU-8 film	50	1000	500	SU-8	SU-8 can be functionalized	Spacing no less than approximately half the height	[53]
3D direct laser writing	Using two-photon polymerization	750	6000	750	PETIA	Quick fabrication; Down to 100 nm resolution	Only use photosensitive polymers	[67] [68]

The two methods that deliver a direct product are phase separation and two-photon polymerization (2PP). The former is not able to reach high AR and although the latter was used for nanopillars of a large diameter, it is possible to reach 100 nm resolution with this technique [68]. 2PP is a technique that is very suitable for rapid prototyping [68, 69], giving the possibility of a high versatility in the design [70]. Because there is a lot of variation in the dimensions that are needed, 2PP is a promising technique. These arguments are summarized in Table 1.3, leading to the following conclusion:

2PP is the only one of the studied methods that delivers on both dimensional requirements and design variety whilst having a minimal number of fabrication steps.

Table 1.3: Grading of fabrication methods in Table 1.2. The grading is based on the pillar dimensions that are possible, the number of fabrication steps that are involved and the possibility to vary over a large range of dimensions.

Method	Grading		
	Dimensions	Steps	Variety
Replica molding	++	−	−
Nanoimprint	++	−	−
Phase separation	−−	+	+
Electron beam lithography	+−	−	−
3D direct laser writing (2PP)	++	+	+

1.4.2. Material

Because the nanopillars have to mimic the actual microprojections and because these structures have high AR, the material choice plays an important role. This choice will be made based on the Young's modulus, to achieve a pillar that has the same stiffness as the microprojections: in the order of magnitude of 1 GPa. Table 1.4 shows the Young's moduli for the materials that were used in Table 1.2. The polymer that was used by Buch-Månson et al. in the '3D direct laser writing using 2PP'-case was based on a formulation of their own and no data on its mechanical properties is available. Therefore a row is added with the Young's moduli of other photosensitive polymers that are used in 2PP.

Table 1.4: Young's Modulus E for the materials used in Table 1.2. Photosensitive polymers: IP-L 780, IP-G 780 and IP-dip.

Material	E [MPa]	Additional info	Reference
PDMS	0.05-1.79	Depending on mixing ratio	[71]
h-PDMS	9	A harder type of PDMS	[72]
PU	12.3		[59]
PUA	374	Type: 301RM	[57]
	451	Type: 311RM	
SU-8	2200	Average value of SU-8 photoresist.	[73]
PMMA	3370		[59]
NPS	5420		[63]
Epoxy	12.6	Type: TC-1622 (BJB enterprise)	[59]
	3000	Type: DER 354 (Dow Chemical)	[60]
PETIA	unknown	Own formulation of PETIA with Lucirin TPO as the photoinitiator	[67]
Photosensitive polymers	750-3500	Depending on laser power	[74]

Because microprojections are high AR structures, it is logical that its Young's modulus is around 1 GPa. Poly-dimethylsiloxane (PDMS) has a Young's modulus that is 3 to 5 orders of magnitude smaller. It was found that pillars made out of PDMS can only reach AR up to 6, whereas pillars made from stiffer materials could reach higher AR up to 18 [60]. This supports the decision to choose a material that has a similar Young's modulus as the original structure.

Table 1.4 shows that several polymers have a Young's modulus in the order of magnitude of 1 GPa: SU-8 photoresist, poly(methyl methacrylate) (PMMA), nanoengineered polystyrene (NPS), Epoxy resin DER 354 and the photosensitive polymers used in 2PP. These materials are found in all fabrication methods that were described in Table 1.2. The Young's moduli of the photosensitive polymers in 2PP depend on the laser power that is used during the printing procedure and thus by varying the laser power, their Young's modulus can be tuned [74]. Next to this tunability, these polymers also belong to the highest graded method in Table 1.3.

1.4.3. Two-photon polymerization
With the different fabrication methods summarized and graded, and looking at the different materials that can be used, the choice is made to use 2PP to fabricate the nanopillar arrays. In photopolymerization a photosensitive resin containing monomers, oligomers and a photoinitiator [70] is locally polymerized by the absorption of light [75]. In 2PP the photoinitiator needs to absorb two photons almost simultaneously to initiate the polymerization. The main difference between single and two photon polymerization is that the absorption of two photons is a non-linear process, having a quadratic dependency on the laser intensity [76]. This causes the polymerization only to occur within a very small central region of the focal point. By tracing the focal point through the resin, 3D structures can be written. The exact working mechanism of 2PP is extensively described in Chapter 2.

1.5. Summary of the literature and approach
To study the crystallization of kidney stones, most of the previous research made use of endoscopic examinations, biopsies and removed stones. By following a recent trend in the study of pathophysiology, using organ-on-chip (OOC) devices, one can study crystallization from the start of nucleation and without the need of human subjects.

It turns out that surface morphology plays an important role in the rate of nucleation of crystals. Within the nephron, four distinct segments can be distinguished that contain a different surface morphology, i.e. the cells in these segments contain microprojections of varying length, diameter and spacing. But there are other factors that also influence kidney stone crystallization. Proteins in the body can inhibit or promote crystal formation and kidney stones seem to grow attached to calcified regions within the kidney. As this is a time limited project, this research will only focus on the fabrication of the different surface morphologies and combining them into a microfluidic chip, leaving other crystallization factors open for future research.

The microprojections on the nephron surfaces are approximated as nanopillars. It was decided to use a polymer because polymers have a similar Young's modulus as the microprojections. This material choice is reassured by the fact that polymers show numerous favorable properties and have already proved their worth in a lot of different fields. With these choices made, a state of the art investigation on the fabrication of polymer nanopillars was performed. Because there is a large variety in both dimensions and spacing density, it was decided that 3D direct laser writing using two-photon polymerization (2PP) is the most suitable fabrication method. Also the polymers that are used in 2PP match the Young's modulus of the original structures that have to be mimicked. Therefor 2PP will be used for fabrication of the polymer nanopillars.

1.6. Initial planning and risk mitigation
1.6.1. Research goal
The research goal is to fabricate surfaces containing the nanostructures of the nephron and integrate them into a microfluidic chip, for the purpose of studying the relation of surface morphology and crystallization of kidney stones.

1.6.2. Research plan
The Gantt chart in Figure 1.2 contains the research plan and corresponding project planning. The planning is based on the number of hours that correspond to the 50 ECTS that will be credited for the research phase of this master thesis. The research plan is divided into four main tasks, which in turn contain subtasks, deliverables and milestones.
The first part of this research will focus on the fabrication of the different surface morphologies that mimic those found in the nephron. The surfaces will be made with the Photonic Professional GT (NanoScribe

WBS	Name (Task, Sub Task, Milestone, Deliverable)	Duration (weeks)	Start (week)	Finish (week)
1	Fabrication	11	7	17
1.1	Design the surface of each Nephron Segment (NS)	2	7	8
D1.1	The 4 different designs in SolidWorks			8
1.2	Optimize NanoScribe parameters	4	9	12
D1.2	Optimized parameters for each NS			12
1.3	Fabricate the 4 surfaces	5	13	17
D1.3	The 4 different surfaces			17
M1	Able to fabricate the NS's using 2PP			17
2	Crystallization	10	18	27
2.1	Set up protocol	2	18	19
D2.1	The action plan (what, why, how)			19
2.2	Test each NS	7	20	26
D2.2	Test results for 2 NS			21
2.3	Characterization of structures versus crystallization	7	21	27
D2.3	Validation of the results for the 2 NS			22
D2.4	Crystallization results for the 4 different surfaces			27
M2	Characterized crystallization for each NS			27
3	Nephron on Chip	11	36	46
3.1	Design fluidic system	4	36	39
D3.1	List of the relevant fluidic properties in biological nephron			36
D3.2	Design and COMSOL model of the full fluidic system			41
3.3	Build fluidic system	4	40	43
D3.3	The complete fluidic system			43
3.4	Validate fluidic system	3	44	46
D3.4	The results			46
M3	Built a working Nephron-on-Chip			46
4	Thesis	5	47	51
4.1	Writing draft	2	47	48
D4.1	Thesis draft			48
4.2	Finalizing thesis	3	49	51
D4.2	Final thesis manuscript			51
M4	Completed and handed in thesis manuscript			51

Figure 1.2: Gantt chart of the full project planning.

GmbH). The designs can be made using 3D CAD software like SolidWorks, and imported into DeScribe (NanoScribe GmbH) which transforms the design into a General Writing Language (GWL) script that is used as the print job for the NanoScribe. For each different design, the best parameters have to be found for an optimal result. When all surface morphologies can be fabricated, the first milestone is reached.

After the surfaces containing the different morphologies are fabricated, the relationship between the individual surface morphologies and the crystallization of COM will be studied. This part will be conducted at the Process & Energy department (P&E), in collaboration with a group that is already working on crystallization. When a characterization is made for each surface morphology, the second milestone of the project is reached.

When all surface morphologies can be fabricated they will be combined into a microfluidic chip. When the design is realized, (artificial) urine will be passed through the chip. Crystals will most likely form, and based on their size the chip can be validated by comparing this to data from literature. When a working microfluidic chip is built, the third milestone is reached and the thesis report can be written and finalized.

1.6.3. Risk mitigation

A risk mitigation will make sure that if a milestone can not be reached via the planned route, another direction can be taken. The milestone corresponding to the first task was to be able to fabricate the different surface morphologies. The first risk is related to the desired resolution that is needed for the fabrication of nanometer-sized pillars. When the resolution is not sufficient, the small diameters and the dense packing density can not be realized. If this is the case, it can be decided to scale up the design, leading to the same morphology although on a slightly bigger scale. A last resort could be to use a totally different fabrication method, which would lead to the loss of prototyping speed. Another risk relates to the aspect ratio's that are tried to be reached. High aspect ratio structures can either ground collapse due to the fact that they are not stiff enough, or laterally collapse due to adhesive forces acting between adjacent pillars. Mitigation would be to look for another material or to redesign and increase the pillar spacing. It is debatable if this redesigned surface would still mimic the nephron surface.

Regarding the crystallization study, it could be that the results that are obtained using the available equipment can not be used to characterize the relation of crystallization and the different surfaces. A different set-up should in this case be designed and built, which will cost extra time and resources. Also cystal nucleation is a stochastic event, which means that a great number of statistical measurements are needed for the results to be meaningful. This can require a lot of time and resources, which can be a problem for the time

limited nature of this research project. As the group at P&E is already working on crystallization, their help can be requested in performing the experiments.

To fabricate the microfluidic chip a lot of techniques and materials will be employed. Material availability should be checked and if necessary they should be pre-ordered. Employing multiple techniques also means utilizing more equipment. It is very likely that downtime of certain machines will be experienced. To be able to continue the work, a planning containing parallel tasks will be advantageous.

Chapter 2

Two-Photon Polymerization

In Appendix A the absorption of photons and how this leads to the formation of radicals is covered in depth. In this chapter the theory and process of two-photon polymerization (2PP) is presented.

2.1. Theory

The conventional way of photo-polymerization makes use of ultraviolet (UV) light to initiate a polymerization chain reaction within a resin containing monomers and photoinitiator. The absorption of a single UV photon delivers enough energy to trigger this event, but it can also be achieved by absorbing two near infrared (NIR) photons. The main difference between single-photon absorption (1PA) and two-photon absorption (2PA) is that the absorption rate in the latter is quadratically dependent on the laser intensity (see Eq. 2.1), whereas in 1PA it has a linear dependency [76]. In 2PP usually a Ti:Sapphire femtosecond pulsed laser is used that can produce ultrahigh-peak power [68]. Because of the short laser pulse of 100 fs and the high numerical aperture lens (NA) that is used, many photons pass through a very narrow volume in the focus in a very short amount of time.

The two photon absorption rate is given by Lee et al. [77] as:

$$\frac{dW}{dt} = \frac{8\pi^2\omega}{n^2C^2}I^2\text{Im}(\chi^{(3)}) \tag{2.1}$$

where ω is the frequency of light, n is the refractive index, C is the speed of light in vacuum, I is the laser intensity and Im(χ(3)) is the imaginary part of the 3th order susceptibility in the material polarization. The absorption rate of energy can also be expressed as the number of photons that are absorbed per unit time:

$$\frac{dn_{\text{photon}}}{dt} = \sigma_2 N F^2 \tag{2.2}$$

where N is the density of the photon absorbing molecules, F is the laser flux, $F = I/h\nu$ and σ_2 is the TPA cross-section which describes the measure of a material's two-photon absorption effectiveness. By combining Eq. 2.1 and Eq. 2.2 the expression for σ_2 can be derived:

$$\sigma_2 = \frac{8\pi^2 h\nu^2}{n^2C^2}\text{Im}(\chi^{(3)}). \tag{2.3}$$

The TPA cross-section is given in units of Göppert-Mayer (GM = 10^{-50} cm^{4}s/photon), who first proposed the theory of TPA in 1931 [78]. Because of the quadratic dependency on the laser intensity (see Eq. 2.1 and Eq. 2.2) combined with a ultrahigh-peak laser power, two-photon polymerization only occurs within a very small central region of the focal point, called the voxel (volume equivalent of a pixel) [68, 74]. The difference in volume where linear and nonlinear absorption take place is visualized in Fig 2.1. By directing the voxel along a 3-dimensional path through a photosensitive resin, the technique can be used for 3-D direct laser writing.

2.2. The setup: Photonic Professional GT

The setup that was used in this research is the Photonic Professional GT from Nanoscribe GmbH, displayed in Fig. 2.3. The NIR laser with a wavelength of 780 nm, is scanned through a resin with a set of pivoted galvano mirrors at a repetition rate of 80 MHz and pulse duration of 100 fs. The sample positioning system consists of

a motorized stage and a piezo stage. Large movements are done with the motorized stage whereas for precise positioning the piezo stage is used. Various objective lenses can be used to focus the laser beam. The choice of objective depends on the end product that one wants to write. For this thesis an objective lens of 63x magnification with a NA of 1.4 was used to achieve a very high resolution. With the chosen objective, two writing configurations can be used, conventional mode and dip-in (DiLL) mode. In conventional mode the objective is immersed in oil on one side of the glass substrate and the resin is located on the other side. In DiLL mode the objective lens is immersed directly in the resin and therefore needs to be cleaned after each print job. The two configurations are schematically presented in Fig. 2.2. The conventional mode is used in this research, because of the ease of use and cleanliness of the objective lens.
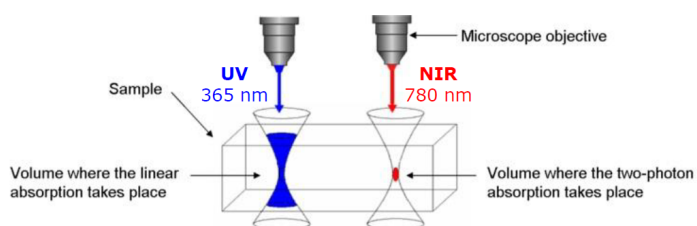
Figure 2.1: Difference in volume where linear and nonlinear absorption take place, reproduced from [79].
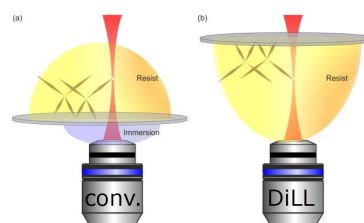
Figure 2.2: Conventional mode and DiLL mode configuration, reproduced from [79].
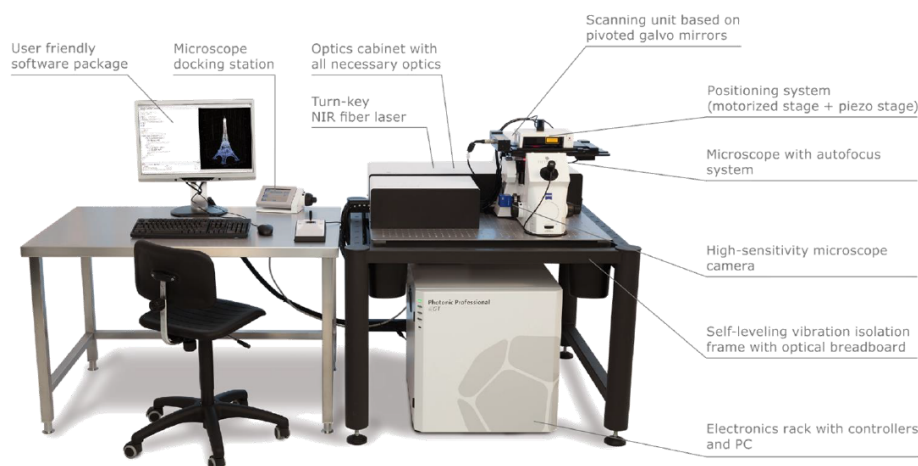
Figure 2.3: The Photonic Professional GT setup, reproduced from [79].

2.3. Material: IP-L 780

The material that was used in this research is IP-L 780 photoresist, provided by Nanoscribe GmbH. The substance application is given as follows: "UV-curable photoresist, which can be used particularly for two-photon absorption lithography" [80]. Nanoscribe GmbH offers a small variety of specially made photoresins: IP-L 780, IP-S, IP-Dip, IP-Q and IP-G 780. Depending on the application a suitable resin can be chosen. IP-L 780 is recommended for a high resolution with low shrinkage. The company does however not disclose the precise formulation of the resists. Therefore the Safety Data Sheet (SDS) is examined.

2.3.1. Material composition

From section 3 in the SDS we learn the actual composition of the resin:

1. > 95 %:   2-(Hydroxymethyl)-2-[[(1-oxoallyl)oxy]methyl]-1,3-propanediyl diacrylate (CAS: 3524-68-3, EG: 222-540-8, INDEX: 607-110-00-3)

2. < 5 %:   7-(Diethylamino)-3-(2-thienylcarbonyl)-2H-1-benzopyran 2-one (CAS: 77820-11-2, EG: –, IN-
DEX: –)

When searching for the substance identifiers in the online chemical database of Pubchem it is found that the
main compound is an acrylate that is mostly used under the name Pentaerythritol triacrylate (PETA), which is
a very commonly used acrylate in two-photon polymerization [81–84]. The second compound is also known
under the name 7-Diethylamino-3-thenoylcoumarin, although its uses were not found. The molecular struc-
tures of the compounds can be seen in Fig. 2.4. Regarding the structure of the second compound in Fig. 2.4b,
it strongly resembles the typical structure of a two-photon absorption dye normally used as photosensitizer,
as described by Lee et al. [85].

(a)   (b)
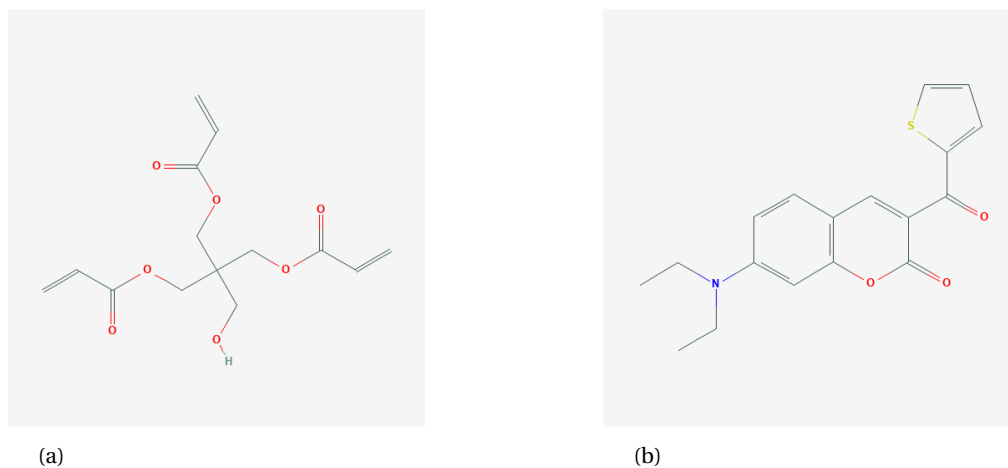
Figure 2.4: Figures show the molecular structures of a) Pentaerythritol triacrylate (PETA) and b) 7-Diethylamino-3-thenoylcoumarin.
Figures reproduced from [86, 87].

2.3.2. Material properties
Values for Poisson's ratio and Young's modulus of IP-L 780 and other IP-photoresists were derived from the
work by Lemma et al [74]. The values for Poisson's ratio and Young's modulus used in this research are 0.475
and 1.1-1.3 GPa respectively.

The surface energy of the material that is used in this research, IP-L 780, is not known. Because PETA is the
main component in IP-L 780 we used values of that material from literature: 41.2 mN/m [88]. In other lit-
erature acrylic specimens covered with photopolymerized acrylic based resins have a surface energy of 45
mN/m [89]. Therefore this seems to be an appropriate value for acrylic based photoresists.

2.4. Voxel size
The resolution in 2PP is equivalent to the voxel size, which depends on multiple variables. Some are writing
parameters like laser power, exposure time, NA of the objective and the distance between two voxels. The
distance in the x,y-plane and in the z-direction between voxels is called the hatching and slicing distance re-
spectively. Next to these, environmental variables like temperature and humidity also influence voxel size. In
this section equations are investigated to determine the size of the voxel.

It is assumed that the material will only polymerize when there is a certain amount of radicals produced by a
photoinitiator, i.e. a certain threshold radical density is exceeded. The radical density ρ can be solved using
Eq. 2.4 [90]:

$$\frac{\partial \rho}{\partial t} = (\rho_0 - \rho)\sigma_2 I^2 \tag{2.4}$$

where ρ_0 is the initiator particle density, σ_2 is the TPA cross-section and I is the laser intensity. This equation
strongly resembles Eq. 2.2 that solved for the number of absorbed photons, which makes sense as the pho-
toinitiator is in this case the photon absorbing molecule. Next it is assumed that the intensity profile of the

laser beam has a Gaussian distribution [85, 90]:

$$I(r_0, 0) = I_0 \exp\left(\frac{-2r_0^2}{\omega_0^2}\right) \tag{2.5}$$

where r_0 is the radius of the beam, I_0 is the beam intensity at the center in the focus plane and ω_0 is the radius of the beam in the focus plane. The value for I_0 can be derived by first calculating the average intensity at the focus plane using Eq. 2.6 [91]:

$$I_{\text{focus}} = \frac{P}{\pi \omega_0^2 \tau f h \nu} \tag{2.6}$$

where P is average power, τ is pulse width and f is repetition rate. With Eq.2.6 we can find the value for I_0 using Eq. 2.7 [91]:

$$I_0 = \frac{2e^2}{e^2 - 1} I_{\text{focus}} \tag{2.7}$$

The intensity of the laser along optical axis z is given by equation 2.8 [85]:

$$I(r_z, z) = \frac{2P_t}{\pi \omega(z)^2} \exp\left(\frac{-2r_z^2}{\omega(z)^2}\right), \quad \text{where} \quad \omega(z) = \frac{\lambda}{\pi \tan[\sin^{-1}(\text{NA}/n)]}\left(1 + \left(\frac{\lambda z}{\pi \omega_0^2}\right)^2\right)^{1/2} \tag{2.8}$$

where P_t is laser power, $\omega(z)$ is the radius of the focused beam along optical axis z, r_z is the distance along the radius axis, λ is the light wavelength, NA is the numerical aperture of the lens used, n is the index of refraction of the immersion oil.

The equations that were derived by Lee et al. [85] for the diameter of the voxel d_{voxel} (Eq. 2.9) and the height of the voxel h_{voxel} (Eq. 2.10) are:

$$d_{\text{voxel}}(P_t, t, \text{NA}) = \frac{\lambda}{\pi \tan[\sin^{-1}(\text{NA}/n)]}\left(\ln\left(\frac{4\pi^2 P_t^2 t(\tan[\sin^{-1}(\text{NA}/n)])^4}{E_{th}\lambda^4}\right)\right)^{1/2} \tag{2.9}$$

$$h_{\text{voxel}}(P_t, t, \text{NA}) = \frac{2\lambda}{\pi \tan[\sin^{-1}(\text{NA}/n)]^2}\left(\left(\frac{4\pi^2 P_t^2 t(\tan[\sin^{-1}(\text{NA}/n)])^4}{\lambda^4 E_{th}}\right)^{1/2} - 1\right)^{1/2} \tag{2.10}$$

where E_{th} is the threshold energy for polymerization.

Using Eq. 2.9 and Eq. 2.10 Lee et al. produced theoretical predictions of voxel diameter and height. The predictions for the voxel diameter are displayed in Fig. 2.5a. When we reproduce the results, the graph in Fig. 2.5b is obtained. The results clearly do not match. **It seems that the graph in 2.5a was in fact not obtained by Eq. 2.9.** In the next sections the equation will be further analyzed.

2.4.1. Dimensional analysis of equation by Lee et al.
When a dimensional analysis is performed on Eq. 2.9 it can be seen that there are residual units on the right hand side of the equals sign:

$$[m] = [m] * \left(\ln\left(\frac{\left[\frac{J}{s}\right]^2 [s]}{[J][m^4]}\right)\right)^{1/2} = [m] * \left(\ln\left(\underbrace{\frac{[J]}{[s][m^4]}}_{\text{residual}}\right)\right)^{1/2} \tag{2.11}$$

This indicates that **Eq. 2.9 is not correct** and is missing certain terms. When we look at the residual units in Eq. 2.11 it can be spotted that this residual resembles the units of the TPA cross section σ_2 ([cm^{4}s/photon]) and photon energy $h\nu$ ([J/photon]). We can cancel out the residual by inserting $\sigma_2/h\nu$ in Eq. 2.9. The equation is now dimensionally correct:

$$d_{\text{voxel}}(P_t, t, \text{NA}, \sigma_2) = \frac{\lambda}{\pi \tan[\sin^{-1}(\text{NA}/n)]}\left(\ln\left(\underbrace{\frac{\sigma_2}{h\nu}}_{} * \frac{4\pi^2 P_t^2 t(\tan[\sin^{-1}(\text{NA}/n)])^4}{E_{th}\lambda^4}\right)\right)^{1/2} \tag{2.12}$$

With Eq. 2.12 new theoretical predictions are made and plotted in Fig. 2.6b. They are compared to the results from Lee et al. in Fig. 2.6a. The theoretical predictions are now more in line with the two plots that are provided by Lee et al.
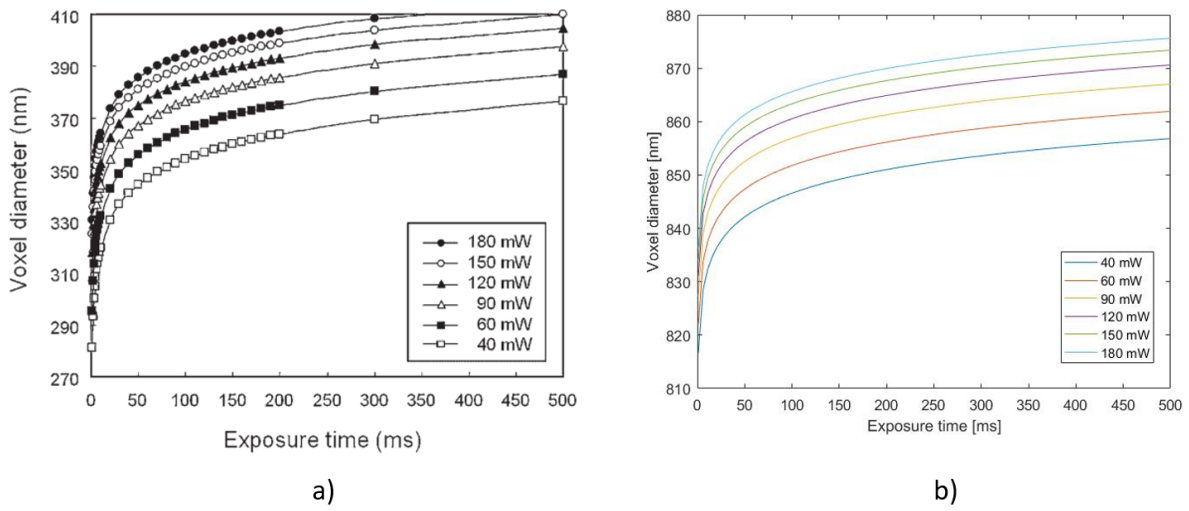
Figure 2.5: Comparing the theoretical predictions of voxel diameter a) made by Lee et al. [85] with b) results by the author using the same equation (Eq. 2.9) The value for threshold energy for polymerization is chosen conservatively to be in the order of magnitude of $10^{-5} W$. The difference in diameter for threshold energy values in the range of $10^{-4} - 10^{-6} W$ is about 20 nm.
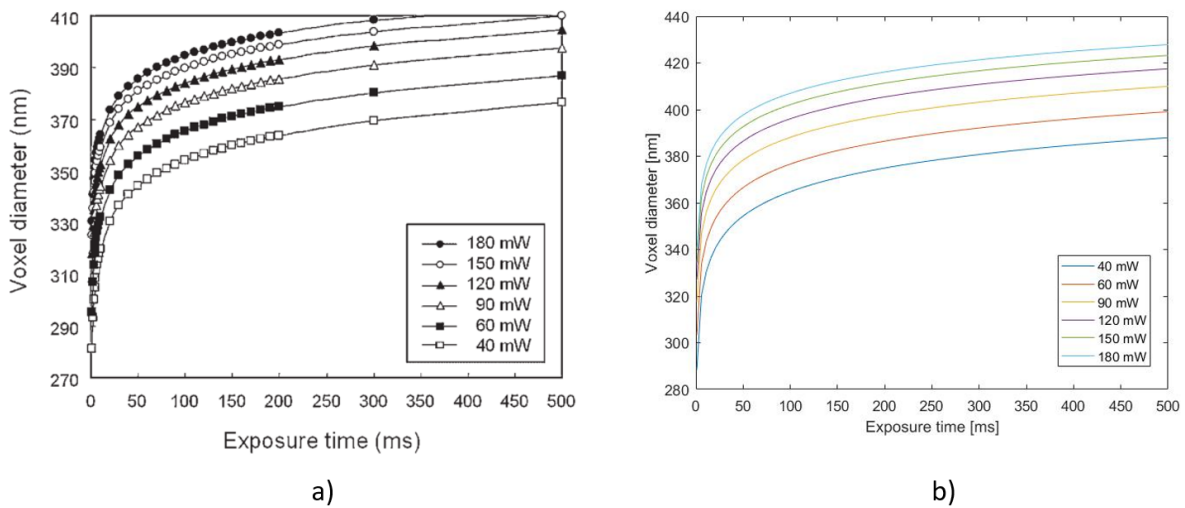
Figure 2.6: Comparing the theoretical predictions of voxel diameter a) made by Lee et al. [85] with b) results by the author using the improved equation (Eq. 2.13). The value for threshold energy is the same as in Fig. 2.5. The value for σ_2 is chosen to be 10^{-50} cm^{4}s/photon.

2.4.2. Qualitative analysis of equation by Lee et al.

The dimensional analysis already showed that Eq. 2.9 proposed by Lee et al. is not correct. We also did a qualitative analysis to find the missing terms.

When we reproduce the math (written down in Appendix. B) the mistake by Lee et al. becomes apparent. Inserting Eq. 2.5 in Eq. 2.4, solving the differential equation for a threshold radical density ρ_{th} and finally solve for $d_{voxel} = 2r_0$ we obtain:

$$d_{\text{voxel}} = \omega_0 \left(\ln \left(\frac{I_0^2 t \sigma_2}{\ln \left(\frac{\rho_0}{\rho_0 - \rho_{th}} \right)} \right) \right)^{1/2} \tag{2.13}$$

The difference between Eq. 2.9 and Eq. 2.13 is that the latter includes the TPA cross-section σ_2, which is an important factor for the material's proneness to TPA. Also the threshold for polymerization is rewritten by Lee et al. from a threshold radical density ρ_{th} to a threshold energy E_{th}. It is believed that during this rewriting a couple of terms are forgotten, which was also indicated by the dimensional analysis.

The relation for d_{voxel} in Eq. 2.13 is also found in other literature [90, 91]. From literature we learn that the term within the large logarithm actually represents the ratio of the peak dose to the threshold dose [92], or the ratio between peak intensity to threshold intensity [93].

It is now clear which terms to look for in Eq. 2.9 derived by Lee et al. First the terms within the logarithm in Eq. 2.9 are simplified to see what they actually represent (using the relation $I = P/A$):

$$\left(\frac{P_t^2 t 4\pi^2 (\tan[\sin^{-1}(\text{NA}/n)])^4}{E_{th} \lambda^4} \right) = \left(\frac{P_t^2 t}{A^2 E_{th}} \right) = \left(\frac{I_t^2 t}{E_{th}} \right)$$

The terms within the logarithm of Eq. 2.9 do not show the ratio of intensities, but rather the ratio of $I_t^2 t$ to the threshold energy E_{th}. Tan et al. provide an equation (Eq. 2.14) for a threshold dose ($F(L)$) (in energy per unit area) [92], with which we can simply transform the threshold energy to threshold intensity:

$$F(L) = \frac{E_{th}}{A} = \beta I_{th}^2 t L \quad \longrightarrow \quad \frac{E_{th}}{A \beta L} = I_{th}^2 t \quad \text{where} \quad \beta = \frac{\sigma_2 \rho_0}{h\nu} \tag{2.14}$$

where L is thickness of photoresist, E is energy, A is illuminated area, β is the two-photon absorption coefficient, I is laser intensity, t is exposure time and ρ_o is initiator particle density.

It strongly seems that the threshold energy introduced by Lee et al. in the original equation (Eq. 2.9) still has to be divided by the terms $A\beta L$ where $\beta = \frac{\sigma_2 \rho_0}{h\nu}$. This leads to the new equation for d_{voxel}:

$$d_{\text{voxel}}(P_t, t, \text{NA}, \sigma_2, \rho_0) = \frac{\lambda}{\pi \tan[\sin^{-1}(\text{NA}/n)]} \left(\ln \left(\underbrace{\frac{\sigma_2 \rho_0 AL}{h\nu}} * \frac{4\pi^2 P_t^2 t (\tan[\sin^{-1}(\text{NA}/n)])^4}{E_{th} \lambda^4} \right) \right)^{1/2} \tag{2.15}$$

The missing terms that were added in the dimensionally improved equation (Eq. 2.12) and the qualitatively improved equation (Eq. 2.15) are almost identical. The difference is the addition of the terms $\rho_0 AL$ in Eq. 2.15. Where Eq. 2.12 does not take into account the number of photons that are absorbed, Eq. 2.15 does cover this by including the density of photon absorbing molecules per unit volume. We therefore believe that Eq. 2.15 is a good correction of the original equation proposed by Lee et al. (Eq. 2.9)

2.5. Scanning speed versus exposure time

In all these equations the exposure time is used, indicating a stationary laser beam. We however used a scanning laser beam to write structures. We can use the approach by Tan et al. that uses scanning speed and repetition rate to derive the exposure time [92]. First the effective number of pulses N_{eff} is calculated, using scanning speed v, repetition rate f and radius of the focused beam ω_0. Then N_{eff} is divided by f to yield exposure time t [92]:

$$t = \frac{N_{\text{eff}}}{f} = \sqrt{\frac{\pi}{2}} \frac{\omega_0}{v} \tag{2.16}$$

The repetition rate is known to be 80 MHz [94]. The radius of the focused beam ω_0 can be calculated using Eq. 2.17 [91]:

$$\omega_0 = \frac{\lambda}{\pi \text{NA}} \sqrt{n^2 - \text{NA}^2} \tag{2.17}$$

where n is the refractive index of the immersion oil. This gives a spot size radius of $\omega_0 = 0.104$ um.

The exposure time corresponding to scanning speed ranging from 1 mm/s - 15 mm/s, the range that is also used in this research, is calculated and presented in Fig. 2.7.
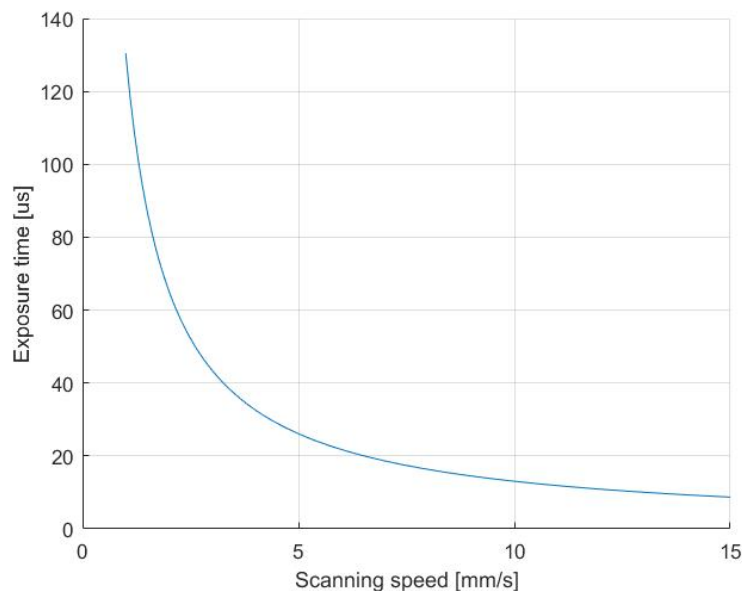
Figure 2.7: Exposure time calculated using Eq. 2.16.

2.6. Conclusions and recommendations

In this chapter we dived deep into the theoretical background of 2PP. There is a plethora of literature on the matter, but most equations show important parameters that were not known in our research group. Further research has to be conducted to find the missing parameters, to be able to link the experimental data to theoretical models and to gain a better understanding on the two-photon polymerization process. The two parameters that are missing are related to the material (IP-L 780):

1. TPA cross-section σ_2, to know the material's effectiveness to two photon absorption.

2. Threshold radical density ρ_{th}, initiator particle density ρ_0 and threshold energy for polymerization E_{th}, to be used in the voxel size calculations.

Because these parameters were unknown, a good approximation of the voxel size and therefore the resolution, could not be made. We had to depend on the experimental results we have gathered. The theory could however be used to check certain trends that are identified from experiments.

Next it was shown that the equations to theoretically approximate the voxel diameter (Eq. 2.9) and height (Eq. 2.10) proposed by Lee et al [85] were missing important terms. A dimensional analysis already showed which terms these could be, after which they were found with a qualitative analysis. The two analyses agreed well on the missing terms and a correct equation to calculate the voxel diameter was proposed (Eq. 2.15).

Chapter 3

Technical Note - IOP Journal of Micromechanics and Microengineering

On the following pages our Technical note is presented, written in the format of the IOP Journal of Micromechanics and Microengineering.

Polymer Nano Manufacturing of a Biomimicking Surface used in Kidney Stone Crystallization Studies

R.M.B. Pleeging[1], L. Sasso[1], H.B. Eral[2], U. Staufer[1]

[1] Delft University of Technology, Dept. of Precision and Microsystems Engineering, Delft, 2628CD, The Netherlands
[1] Delft University of Technology, Dept. of Process and Energy, Delft, 2628CD, The Netherlands

ABSTRACT

Kidney stone disease is an increasing worldwide issue. The current lack of understanding of the exact mechanisms involved is partially due to the need for experimental instrumentation able to mimic the microenvironmental conditions present in vivo. As crystal nucleation often initiates at liquid-solid interfaces, the interface morphology plays a significant role in the rate of nucleation. Within the nephron, the functional unit of the kidney, four distinct segments can be distinguished that contain different surface morphologies. Particularly, the cells lining these segments contain protrusions in the shape of nanopillars that vary in length, diameter and spacing. Exploiting the opportunities provided by organ-on-chip technology, we designed and manufactured a microfluidic device proposed to increase our understanding of the relation between kidney surface morphology and kidney stone crystallization. We used two-photon polymerization to fabricate surfaces that contain the nephron morphologies in a material possessing a Young's modulus matching the value of the biological structures. After optimizing design and process parameters like laser power and scanning speed, we manufactured nanopillars with diameters in the range of 150-250 nm and aspect ratios up to 100, with which we can mimic the protrusions in the nephron. The fabricated cilia were incorporated in the microfluidic device, which was used to crystallize calcium oxalate.

Keywords: Kidney stones, two-photon polymerization, biomimicry.

1 Introduction

Kidney stone disease has an increasing prevalence worldwide [1] and already costs the private sector five billion dollars annually [2]. The disease has been treated for several millennia [3,4] and a great deal of knowledge on stone growth has been acquired by biopsies and examination of removed stones. But because of this post factum approach, there still is a current lack of understanding of the exact mechanisms that drive stone formation. The historical void of experimental instrumentation able to mimic the microenvironmental conditions present in vivo has only recently been filled by the emergence of organ-on-chip (OOC) technology, providing us with an opportunity to study the formation of kidney stones in vitro. A recent study has tried to capture some of the physiological conditions of the kidney in a biomimetic model to study the crystallization of the most common type of kidney stone: calcium oxalate (CaOx) [5]. In that study Lafitte et al. proposed a microfluidic channel with dimensions matching the collecting duct of the human kidney, using physiological concentrations and flow rates. Crystallization is however an intricate process influenced by many factors, amongst which are the surface characteristics of the solid-liquid interface. In heterogeneous nucleation theory it is stated that crystals often nucleate at this interface [6] and a recent study shows that the surface morphology of the interface can promote or hinder nucleation [7]. Within the nephron, the functional unit of the kidney, four distinct segments can be distinguished that contain different surface morphologies: the proximal convoluted tubule (PCT), the thin segments of the loop of Henle, the distal convoluted tubule (DCT) and the collecting duct (CD). Particularly, the cells lining these segments contain protrusions or microprojections called microvilli and cilia, shaped as nanopillars that vary in length, diameter and spacing. The relation between nephron surface morphology and kidney stone formation has to our knowledge not yet been studied.

Here we propose a rapid and facile approach to fabricate polymer nanopillar arrays, using two-photon polymerization (2PP), to mimic the surface morphology of the different nephron segments. This fabrication method can encompass the large dimensional variety of the microprojections and is a direct fabrication method, i.e. it does not require expensive master molds or multiple fabrication steps. 2PP exploits the non-linear dependency of a material's two-photon absorption rate on the incident light intensity [8]. This causes the polymerization only to occur within a very small central region of the focal point, called the voxel (volume equivalent of a pixel) [9,10]. By directing the voxel along a three-dimensional path through a photosensitive resin, the technique can be used for 3D direct laser writing. Using a polymer even adds more resemblance to the microprojections as its Young's modulus lies in the same range of that of the microprojections, around 1 GPa [11–14]. Moreover polymers are especially favorable due to their low cost and proved worth in many fields like tissue engineering [15], microfluidic devices [16] and bioinspired materials [17].

The microprojections found on the cell membranes in the different segments of the nephron were approximated as nanopillars with certain dimensions. To mimic these microprojections using 2PP, we aimed to write nanopillar arrays with 1) a minimum pillar diameter, 2) a minimum pillar-to-pillar spacing and 3) a maximum aspect ratio (AR). These three targets were compared with the characteristic microprojection dimensions. A microfluidic device was fabricated in which the written nanopillars were incorporated and used to crystallize CaOx.
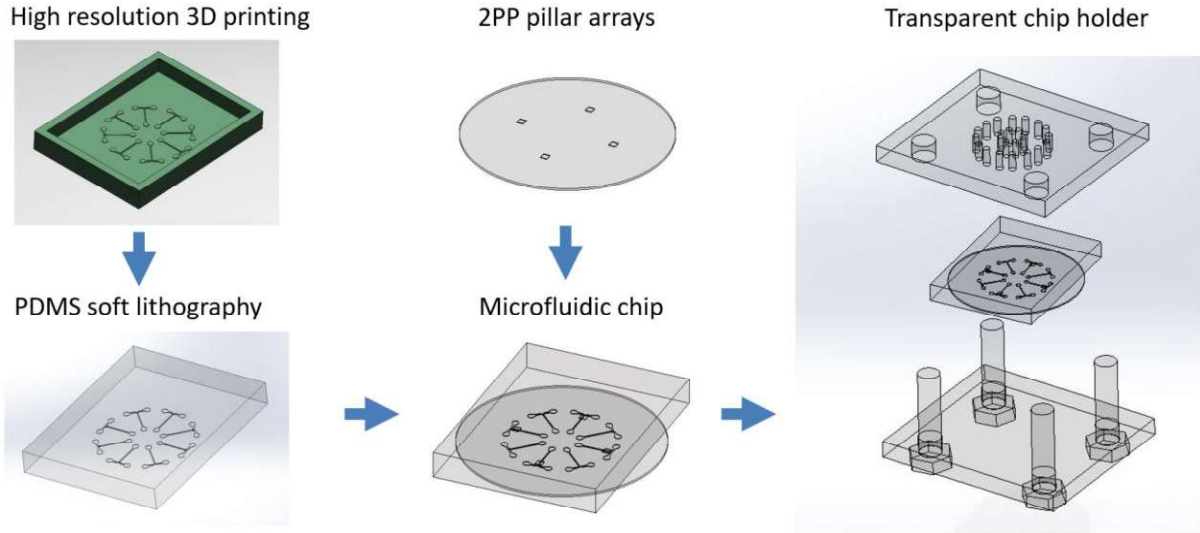
Figure 1: Fabrication steps of the microfluidic device.

Renal microprojections: cilia and microvilli

Renal microvilli typically are about 80 nm in diameter [18] and 1-3 μm in height [19] for a well developed brush border. The spacing between microvilli varies with the flow rate in the tubule, and is about 75 to 130 nm in the brush border [20, 21]. Microvilli can also appear as small bumps on the cell surface [22] having a relatively short length of 500 nm or less [23]. The cilium is much larger, having a diameter of about 250 nm [18] and a height of 7-10 μm [19]. The Young's modulus of both the microvillus and cilium is assumed to be in the order of magnitude of about 1 GPa [11–14]. The dimensions of the cilia and microvilli are summarized in the left hand side of Table 1.

2 Experimental

Fabrication of the nanopillars

For the fabrication of the nanopillars we used the Photonic Professional GT (Nanoscribe GmbH) in conventional mode with an objective lens of 63x magnification and numerical aperture of 1.4. First a glass cover slip (Menzel-Gläser) with diameter 30 mm and 0.17 mm +/- 0.01 mm thickness was rinsed with acetone (Merck KGaA) and wiped with a soft cloth. The cover slip was then rinsed with 2 propanol (IPA, Honeywell Riedel-de-Haën) and again wiped with a soft cloth. The cover slip was placed on the sample holder and fastened with tape. On the bottom of the glass cover slip a droplet of immersion oil (Immersol 518 F, Zeiss) was placed, on the top a droplet of IP-L 780 (Nanoscribe GmbH). Using the computer software Describe 2.5.3 (Nanoscribe GmbH) a job-file was created that builds an array of 100 nm diameter pillars in a layer-by-layer fashion. The height and spacing of the pillars and the size of the pillar arrays was varied throughout the experiments. One pillar slice consisted of a line around the circumference of the pillar, filled in with five lines with 20 nm hatching distance. The layers were placed on top of each other at 50 nm slicing distance. The scanning speed and laser power were optimized for our structures. The job-file was executed with Nanowrite 1.8.12 (Nanoscribe GmbH). After completion the cover slip was placed in a custom made holder and immersed for 25 minutes in Propylene glycol monomethyl ether acetate (PGMEA, Sigma-Aldrich) followed by an immersion for 5 minutes in IPA.

Critical point drying of the nanopillars

A critical point dryer (Emitech K850) was used to dry the glass cover slip after immersion in IPA to circumvent surface tension. The capillary forces caused by the surface tension of the rinsing liquid during air drying cause the pillars to collapse, which is not desirable.

Measuring the nanopillars

To inspect and measure the written pillars, the glass cover slip with structures was sputter coated (SC7620, Quorum Technologies) with a 6 nm layer of gold/palladium (Au/Pd) and imaged with a scanning electron microscope (SEM, Jeol JSM-6010LA) using a 45° sample holder. Measurements were made to calculate mean diameter and standard deviation (SD). In this paper SD is indicated with a ± value. The spacing in between two pillars was calculated using the predetermined center-to-center spacing and the measured mean diameter.

Manufacturing the microfluidic device

The fabrication steps of the microfluidic device are presented in Fig. 1. High resolution 3D printing (EnvisionTEC Micro Plus Hi-res) was used to fabricate a mold from photocurable resin (HTM140, EnvisionTEC). The mold contained the negative versions of eight 100 μm high and 150 μm wide microchannels. After printing, the mold was immersed in IPA to remove uncured HTM140 and subsequently UV flooded (Photopol Curing Unit).

Polydimethylsiloxane (PDMS) elastomer and curing agent (Sylgard 184, Dow Corning) were mixed in a 10:1 ratio, poured in the mold and cured. After curing the PDMS was cut with a scalpel around the edges of the mold and peeled out. Holes for the inlets and outlets were punched with a 23G blunt end needle.

The chip was assembled in a cleanroom environment by combining the PDMS component with a glass cover slip. PE-10 tubing was inserted in the inlets and outlets and the chip was placed in a custom chip holder. This chip holder consisted of a top and bottom part of laser cut transparant acrylate hold together with four bolts and nuts (M5). With this holder we could make a reversible watertight seal between the glass and PDMS.

3 Results

The Photonic Professional GT (Nanoscribe GmbH) was used to write various polymer nanopillar arrays in order to find the 1) minimum pillar diameter, 2) minimum pillar-to-pillar spacing and 3) maximum aspect ratio (AR). To circumvent the surface tension of the rinsing liquid during drying, the samples were critical point dried with $CO2$. Fig. 2a-2c show the resulting nanopillar arrays and the results are included on the right hand side of Table. 1. The dimensions were measured and here presented in the following notation: *mean ± standard deviation.*

1. Nanopillars were written with a diameter of 145 nm ± 4 nm. These pillars were spaced at a center-to-center spacing of 500 nm and a height of 692 ± 8 nm. The pillars were written in an array of 20 μm x 20 μm, resulting in 1681 pillars. The laser power and scanning speed were 7.5 mW and 3 mm/s respectively.

2. The smallest spacing was achieved by writing a nanopillar array with a center-to-center spacing of 400 nm. This array contained nanopillars with a diameter of 243 nm ± 8 nm, leading to a pillar-to-pillar spacing of 157 nm ± 8 nm. This array measured 24 μm x 24 μm and contained 4096 pillars. The laser power and scanning speed were 7.5 mW and 3 mm/s respectively.

3. The maximum AR was found by printing pillars with increasing height. The pillars had a diameter of 254 nm ± 17 nm and were written with a laser power of 8 mW and a scanning speed of 3 mm/s. Up to a height of 25 μm the pillars remained upright, giving them an AR of approximately 100. Above this height the pillars ground collapsed.

When we compare the dimensions of the renal microprojections with the pillar dimensions we obtained using 2PP, we can clearly see that the primary cilium, located in the collecting duct of the nephron, has dimensions that can easily be reproduced using our approach. A nanopillar array was written with these dimensions to mimic the primary cilia, shown in Fig. 2d. The pillars measured 251 nm ± 22 nm in diameter, 7514 nm ± 116 nm in height and 8 μm in spacing and do therefore indeed mimic the renal cilia, both in terms of morphology and topography (shape and size). 2PP was could however not be used to fabricate pillars in the small size range of microvilli. The obtained minimum diameter of 145 nm ± 4 nm is almost twice the diameter of a microvillus (80 nm) and the obtained smallest spacing of 157 nm ± 8 nm only approaches the largest spacing we find for a brushborder of microvilli (130 nm). The written nanopillar arrays approach but do not match the actual sizes of microvilli. Thus although the surface morphology can be mimicked, the biological structures are slightly smaller.

Another feat that our approach offers is that we can exploit the layer-by-layer writing fashion and change the writing parameters throughout the pillar itself. This is not possible with the 'import-STL' function of Describe (Nanoscribe GmbH), that automatically creates a job-file for any imported 3D CAD model. The diameter of the pillars was varied by keeping the design diameter at 100 nm and vary the laser power. By changing the laser power throughout the length of a pillar, the shape of that pillar could be manipulated.

The microfluidic chip consisted of a polydimethylsiloxane (PDMS) component with multiple microchannels closed off with a glass cover slip. The nanopillar arrays written with 2PP on the glass cover slip were encapsulated by the walls of the microchannels. The width of those arrays was wider (400 μm) than the width of the microchannel (150 μm) to account for inaccurate positioning. To remain a watertight seal the microfluidic chip was placed in a transparent chip holder. The device is presented in Fig. 3. There was no leakage between the PDMS and glass up to a flow rate of 200 μL/min which is far above physiological flow rates (1 μL/min) [5]. As the surface tension during drying of the pillar arrays caused collapse, filling the chamber with fluid posed the same problem. When the channel was filled with water, the surface tension pushed down the pillars. This was not the case when ethanol was used, which can be explained by alcohols having a lower surface tension. The channel was first filled with ethanol, which was then replaced with water. This made sure the pillars remained upright when the channel was filled with water. However any bubble traveling through the microchannel introduces another liquid-gas phase boundary, i.e. surface tension. Therefore the microfluidic setup should be improved with bubble traps.

For a first experiment we used aqueous solutions of calcium and oxalate at 8.0 mM as precursors, pumped through the microchannel at 1 μL/min for two hours. Afterwards the chip was demounted, the crystals were observed with an SEM and the crystal phase was determined based on the shape. The majority of crystals was calcium oxalate monohydrate but also individual calcium oxalate dihydrate crystals were spotted (see Fig. 4). The transparent device also enabled us to observe and image a particular microchannel during crystallization. With this an induction time could be derived. When precursors were used at physiological concentrations, 12.0 mM and 0.40 mM for respectively calcium and oxalate precursors [25], we could see crystals forming in the microchannel starting at 165 seconds. These results were too premature for any conclusion and were solely used as a proof of principle.

Table 1: On the left hand side: the dimensions for the various microprojections in the nephron, approximated as nanopillars with a certain diameter d, height h and pillar-to-pillar spacing s. On the right hand side: the measured diameter d, height h and pillar-to-pillar spacing s of the arrays that were written with 2PP to find the 1) minimum pillar diameter, 2) minimum pillar-to-pillar spacing and 3) maximum pillar aspect ratio, of which images are presented in Fig. 2. Measurements are presented as *mean ± standard deviation*. The written cilia clearly mimic the dimensions of the renal primary cilia.

Renal microprojections						Two-photon polymerization				
Segment	Type of protrusion	d [nm]	h [μm]	s [nm]		Array	d [**nm**]	h [nm]	s [nm]	Figure
PCT	brushborder of microvilli [18]	80 [18]	1-3 [19]	75-130 [20, 21]		1.	145 ± 4	692 ± 8	355 ± 4	Fig. 2a
Loop of Henle	none [18]	-	-	-		2.	243 ± 8	1.022 ± 9	157 ± 8	Fig. 2b
DCT	sparse microvilli [18]	80 [18]	<0.5 [22]	varying [18, 24]		3.	254 ± 17	≈ 25.000	≈ 25.000	Fig. 2c
CD	primary cilium [18]	250 [18]	7-10 [19]	≈ 8.000 [18]		cilia	251 ± 22	7.514 ± 116	≈ 8.000	Fig. 2d
	brushborder of microvilli [18]	80 [18]	<0.5 [22]	75-130 [20, 21]						

(a)

(b)

(c)

(d)
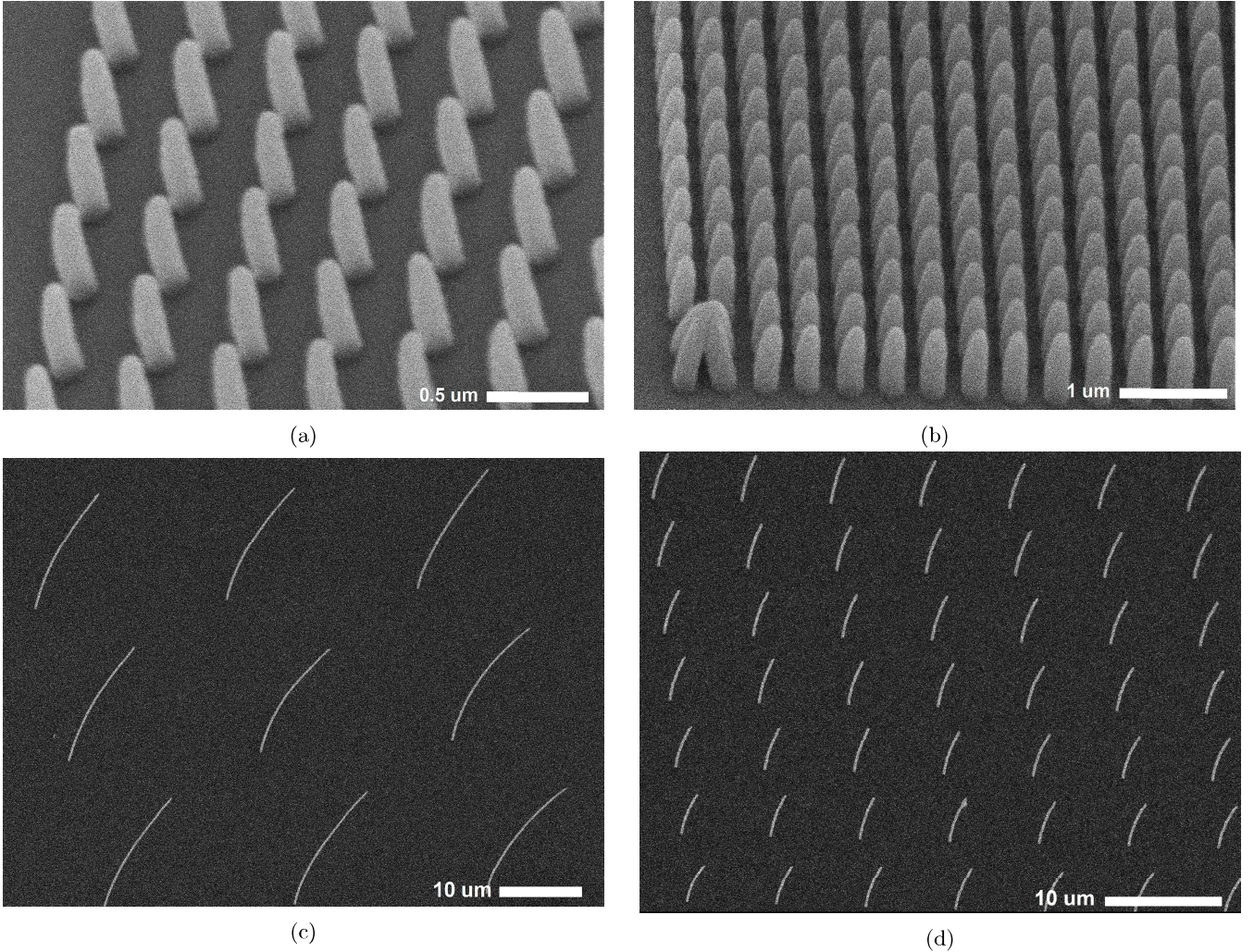
Figure 2: SEM images of the written nanopillar samples on a 45° sample holder, showing a) minimum pillar diameter of 145 nm ± 4 nm, b) minimum pillar-to-pillar spacing of 157 nm ± 8 nm and c) maximum AR of approximately 100, having a pillar diameter of 254 nm ± 17 nm and a height of 25 μm. Figure in d) shows the pillar array that was written to mimic the primary cilium in the collecting duct. With a diameter of 251 ± 22 and a height of 7.514 ± 116 the written cilia do indeed mimic the renal cilia. Scalebars are a) 0.5 μm, b) 1 μm, c) 10 μm, d) 10 μm.
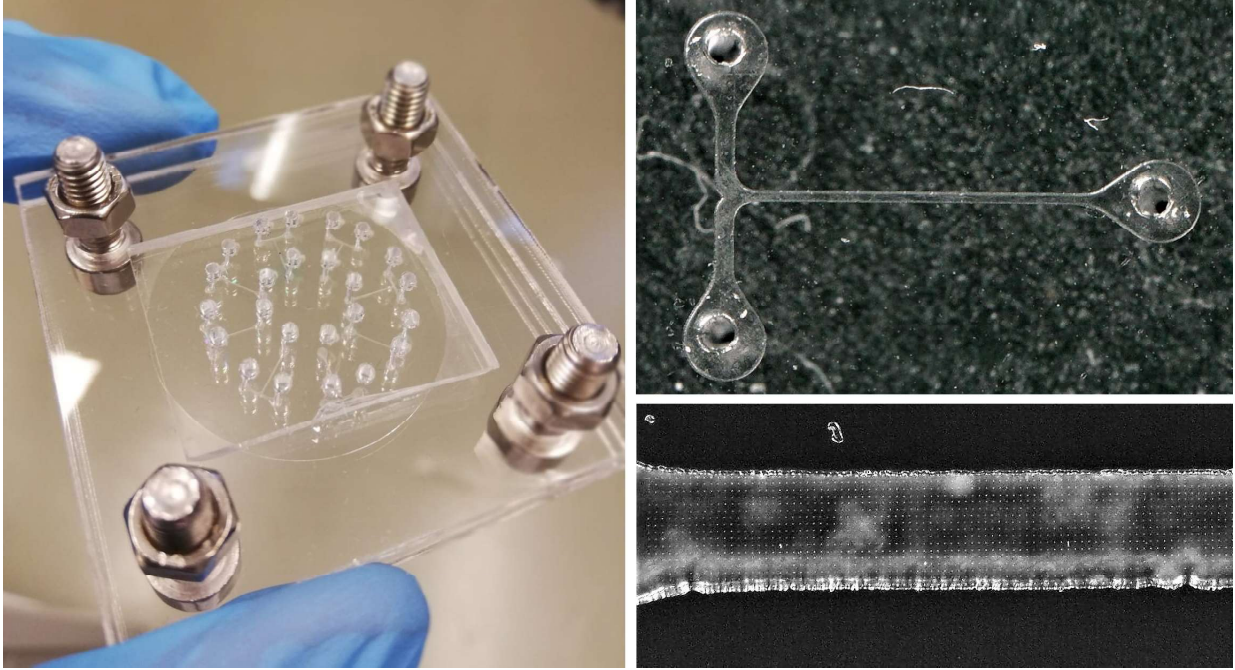
Figure 3: The transparent microfluidic device containing eight microfluidic channels (left). One of the eight microfluidic channels with two inlets and one outlet (top right). The array of printed cilia inside the microfluidic channel (bottom right).

4 Reproducibility

While the writing parameters were kept constant for all experiments, the reproducibility of results proved to be very cumbersome. The nanopillar arrays in Fig. 2 were all printed with a laser power of 7.5 mW or 8 mW, but have different diameters. It is believed that this was caused by a decrease in laser dose, probably due to growing misalignments within the optical path. Because of this decay in laser dose it is important to always perform a dose test before a printing job is initiated.

5 Conclusions

We presented a direct fabrication method to fabricate nanopillar arrays that can be used to mimic the morphology of the cell membrane surfaces found in the human nephron. Using two-photon polymerization we were able to write nanopillars with a minimum diameter of 145 nm $\pm$ 4 nm, nanopillar arrays with a minimum spacing of 157 nm $\pm$ 8 nm and nanopillars with an aspect ratio of up to 100, having a diameter of 254 nm $\pm$ 17 and a height of approximately 25 μm. With this we achieved to print nanopillars that 1:1 resemble the primary cilia found in the collecting duct of the human nephron. Also we have successfully integrated the printed cilia into a microfluidic chip and crystallized CaOx on chip. The chip dimensions combined with a surface morphology adds another step in making a device resembling the human nephron.

6 Future outlook

Our work is now aimed at improving the microfluidic setup and gaining particular insight on the influence of kidney surface morphology on kidney stone formation. The stochastic nature of crystallization bids us to perform many experiments to support any claim with statistics. As there are multiple morphologies found in the nephron, the number of experiments is substantial. Our microchip contains eight separate microchannels which decreases fabrication time. Performing experiments in parallel is hoped to decrease the experimentation time.
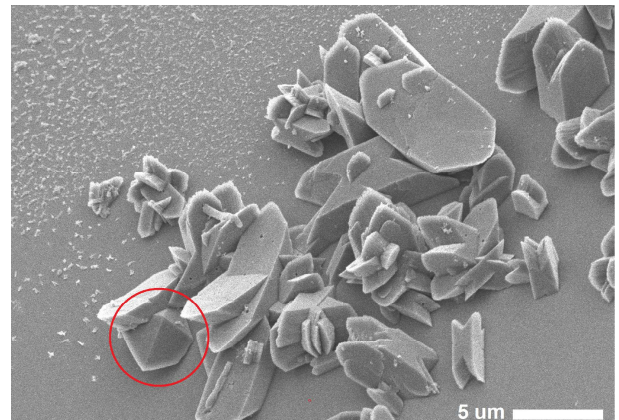
Figure 4: CaOx crystals formed in the device after two hours, using calcium and oxalate precursor solutions (8.0 mM) at a flow rate of 1 μL/min. Majority of the crystals is COM, encircled an individual COD crystal.

5

References

[1] V. Romero, H. Akpinar, and D. G. Assimos, "Kidney stones: a global picture of prevalence, incidence, and associated risk factors.," *Reviews in urology*, vol. 12, no. 2-3, pp. e86–96, 2010.

[2] C. S. Saigal and G. Joyce, "Direct and indirect costs of nephrolithiasis in an employed population: Opportunity for disease management?," *Kidney International*, vol. 68, pp. 1808–1814, 2005.

[3] J. Shah and H. N. Whitfield, "Urolithiasis through the ages," *BJU International*, vol. 89, no. 8, pp. 801–810, 2002.

[4] A. Tefekli and F. Cezayirli, "The history of urinary stones: in parallel with civilization.," *TheScientificWorldJournal*, vol. 2013, p. 423964, nov 2013.

[5] G. Laffite, C. Leroy, C. Bonhomme, L. Bonhomme-Coury, E. Letavernier, M. Daudon, V. Frochot, J. P. Haymann, S. Rouzière, I. T. Lucas, D. Bazin, F. Babonneau, and A. Abou-Hassan, "Calcium oxalate precipitation by diffusion using laminar microfluidics: toward a biomimetic model of pathological microcalcifications," *Lab Chip*, vol. 16, no. 7, pp. 1157–1160, 2016.

[6] D. Turnbull, "Kinetics of Heterogeneous Nucleation," *The Journal of Chemical Physics*, vol. 18, no. 36, pp. 198–1103, 1950.

[7] Y. Diao, T. Harada, A. S. Myerson, T. Alan Hatton, and B. L. Trout, "The role of nanopore shape in surface-induced crystallization," *Nature Materials*, vol. 10, no. 11, pp. 867–871, 2011.

[8] S. Maruo, O. Nakamura, and S. Kawata, "Three-dimensional microfabrication with two-photon-absorbed photopolymerization," *Optics Letters*, vol. 22, no. 2, p. 132, 1997.

[9] K. S. Lee, R. H. Kim, D. Y. Yang, and S. H. Park, "Advances in 3D nano/microfabrication using two-photon initiated polymerization," *Progress in Polymer Science (Oxford)*, vol. 33, no. 6, pp. 631–681, 2008.

[10] E. D. Lemma, F. Rizzi, T. Dattoma, B. Spagnolo, L. Sileo, A. Qualtieri, M. De Vittorio, and F. Pisanello, "Mechanical Properties Tunability of Three-Dimensional Polymeric Structures in Two-Photon Lithography," *IEEE Transactions on Nanotechnology*, vol. 16, no. 1, pp. 23–31, 2017.

[11] P. Guo, A. M. Weinstein, and S. Weinbaum, "A hydrodynamic mechanosensory hypothesis for brush border microvilli," *Am J Physiol Renal Physiol*, vol. 279, pp. F698–F712, 2000.

[12] H. Kojima, A. Ishijima, and T. Yanagida, "Direct measurement of stiffness of single actin filaments with and without tropomyosin by in vitro nanomanipulation.," *Proceedings of the National Academy of Sciences*, vol. 91, no. 26, pp. 12962–12966, 1994.

[13] M. Kikumoto, M. Kurachi, V. Tosa, and H. Tashiro, "Flexural Rigidity of Individual Microtubules Measured by a Buckling Force with Optical Traps," *Biophysical Journal*, vol. 90, no. 5, pp. 1687–1696, 2006.

[14] D. B. Wells and A. Aksimentiev, "Mechanical properties of a complete microtubule revealed through molecular dynamics simulation," *Biophysical Journal*, vol. 99, no. 2, pp. 629–637, 2010.

[15] P. X. Ma, "Biomimetic materials for tissue engineering," *Advanced Drug Delivery Reviews*, vol. 60, no. 2, pp. 184–198, 2008.

[16] H. Becker and C. Gärtner, "Polymer microfabrication technologies for microfluidic systems," *Analytical and Bioanalytical Chemistry*, vol. 390, no. 1, pp. 89–111, 2008.

[17] C. Zhang, D. A. Mcadams, and J. C. Grunlan, "Nano/Micro-Manufacturing of Bioinspired Materials: a Review of Methods to Mimic Natural Structures," *Advanced Materials*, vol. 28, no. 39, p. 8566, 2016.

[18] T. Lazar, "Histology and Cell Biology: An Introduction to Pathology," *Tissue and Cell*, vol. 34, pp. 5–8, dec 2002.

[19] Saladin, *Anatomy and Physiology: The Unity of Form and Function*. McGraw-Hill, 5th ed., 2009.

[20] H. Sakaguchi and Y. Suzuki, "Fine structure of renal tubule cells," *Keio Journal of Medicine*, vol. 7, 1958.

[21] S. Weinbaum, P. Guo, and L. You, "A new view of mechanotransduction and strain amplification in cells with microvilli and cell processes.," *Biorheology*, vol. 38, no. 2-3, pp. 119–142, 2001.

[22] H. Hücker, H. Frenzel, and D. Skoluda, "Scanning electron microscopy of the distal nephron and calyx of the human kidney," *Virchows Archiv B Cell Pathology*, vol. 18, no. 1, pp. 157–164, 1975.

[23] J. Gorelik, A. I. Shevchuk, G. I. Frolenkov, I. A. Diakonov, M. J. Lab, C. J. Kros, G. P. Richardson, I. Vodyanoy, C. R. W. Edwards, D. Klenerman, and Y. E. Korchev, "Dynamic assembly of surface structures in living cells.," *Proceedings of the National Academy of Sciences of the United States of America*, vol. 100, pp. 5819–22, may 2003.

[24] C. Sauvanet, J. Wayt, T. Pelaseyed, and A. Bretscher, "Structure, Regulation, and Functional Diversity of Microvilli on the Apical Domain of Epithelial Cells," *Annu. Rev. Cell Dev. Biol*, vol. 31, pp. 593–621, 2015.

[25] C. N. LaFratta and T. Baldacchini, "Two-photon polymerization metrology: Characterization methods of mechanisms and microstructures," *Micromachines*, vol. 8, p. 101, mar 2017.

Experimental: Using Two-Photon Polymerization to Write Nanopillar Arrays

The setup and working principles that were used to print nanopillar arrays are described in detail in Chapter 2 and Appendix A. First an optimization of the writing parameters was achieved through many experiments and nanopillar measurements. Several iteration steps were performed, in which was tried to fine-tune the writing parameters to achieve a desirable diameter and height. Later, when diameters in the right regions could be achieved, the spacing was investigated to try and mimic the brush border of microvilli. The iterations are presented in Appendix F, each with a set of design parameters, design choices, observations, data analysis and a short discussion towards the next iteration. To avoid the pillars from collapsing during evaporation of the rinsing liquid after printing, we used critical point drying. The working principles are described in more detail in Chap. 5 and Appendix C. In this chapter the design choices are motivated and observations are presented. The results can be found in the paper in Chapter 3.

4.1. Design of the nanopillar arrays

At first the pillar arrays where designed using CAD software (SolidWorks 2017, DS SolidWorks Corp.) and imported in the Describe software (Nanoscribe GmbH) using the 'Import STL' tool. With this tool the writing parameters could be chosen for the whole structure, as well as the hatching and slicing distance. This stands for respectively the horizontal and vertical distance between voxel lines. There are a couple of downsides to this approach.

- The whole structure is written with the same writing parameters. The necessity of being able to vary parameters throughout the same structure will be discussed in Section 4.4.1.

- For every change in diameter, height or spacing a new CAD model has to be created. This is very time-consuming and tedious.

- For every change in hatching or slicing distance the design has to be newly imported in the software to give it new parameters.

Therefore a Graphical User Interface (GUI) was made using Matlab 2016b (The MathWorks, Inc) that outputs code used in the software to build one layer of a pillar with a certain diameter and hatching distance (see Fig. 4.1). By stacking and placing these pillar slices, we could very easily build pillar arrays with a certain spacing and slicing, demonstrated in Fig. 4.2. The arrays are built up by first writing the bottom slices for all pillars in the array and building the array vertically upwards with slices until the right height is reached.

4.2. Printing the pillar arrays

The first objective was to look for a workable range of the laser dose, which is a combination of writing parameters laser power and exposure time. Because the laser is scanned through the resin with galvano mirrors, the exposure time was varied by using different scanning speeds. We converged towards a usable working range of writing parameters by performing multiple iterations of parameter optimization. This parameter optimization was performed by printing our design in a large array with varying laser powers and scanning speeds. Such a parameter optimization array is presented in Fig. 4.3. Within the scanning speed range of 1 mm/s to 20 mm/s recommended by Nanoscribe GmbH [94] it was found that in the upper half op this regime the cross-sectional shape of the pillar became oval shaped instead of circular. For the lower scanning speeds we found that below a laser power of 7 mW, no polymerization occurs and from 22 mW upwards the resin

(a)   (b)
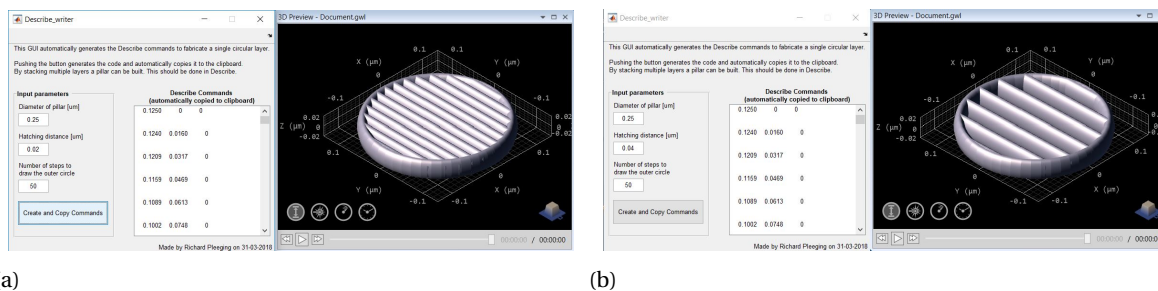
Figure 4.1: Figures showing the Matlab GUI on the left and the Describe preview on the right for a 250 nm diameter pillar with a) hatching distance of 0.02 μm and b) hatching distance of 0.04 μm.
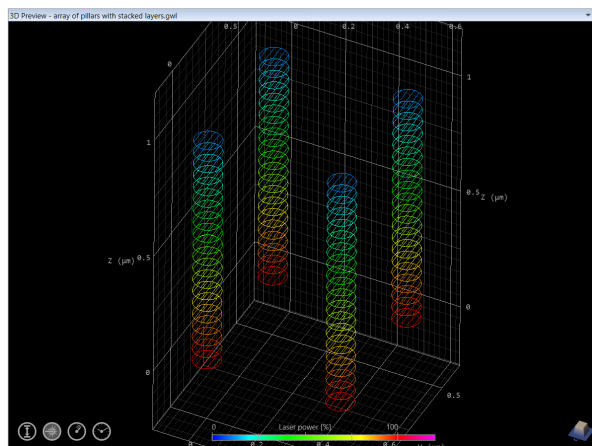
Figure 4.2: Figure shows the stacking and placing of pillar slices to built a 2 x 2 pillar array in DeScribe. By using this stacking approach the writing parameters could be varied throughout the pillar itself. Here the laser power is gradually decreased from base to top, red being high and blue low laser power.

heats to a level where it starts to burn and boil. Also several hatching and slicing distances were tried, after which a fixed set of working values was chosen for consistency throughout the research. The values used were a hatching distance of 20 nm and a slicing distance of 50 nm.

4.3. Measuring and inspecting the printed nanopillar arrays

4.3.1. Scanning electron microscope imaging for nanopillar measurements

To inspect and measure the written pillars, a scanning electron microscope (SEM, Jeol JSM-6010LA) using a 45° sample holder was used after the pillars were sputter coated (SC7620, Quorum Technologies) with a 6 nm layer of gold/palladium (Au/Pd). Multiple samples were prepared and of each three pillars were measured at three different locations along the length of the pillar. The measurements were either made during imaging using the provided software InTouchScope (Jeol, Ltd.) or later using the image analysis software Fiji. These measurements were used to calculate mean diameter and standard deviation. The spacing in between two pillars was calculated using the predetermined center-to-center spacing and the measured average diameter.

4.3.2. Keyence digital microscope imaging for nanopillar inspection

Regarding the future use of the written structures in crystallization experiments, it is not desirable to have them covered with Au/Pd. However it has to be checked whether the pillars, after drying, stand upright or not. A method was found to see the larger (250 nm diameter) pillars using a tilted digital microscope (Keyence VHX-6000) and making use of the included software. With the 'multi-light' tool a composite image was constructed by combining the images made with different light-sources. From these composite images we were indeed able to see whether the pillars stood upright or not. We can clearly see from the images in Fig. 4.4 the difference in height of the pillar arrays.

More densely packed pillars (below 1 μm) could not be seen with any microscope other than a SEM. However
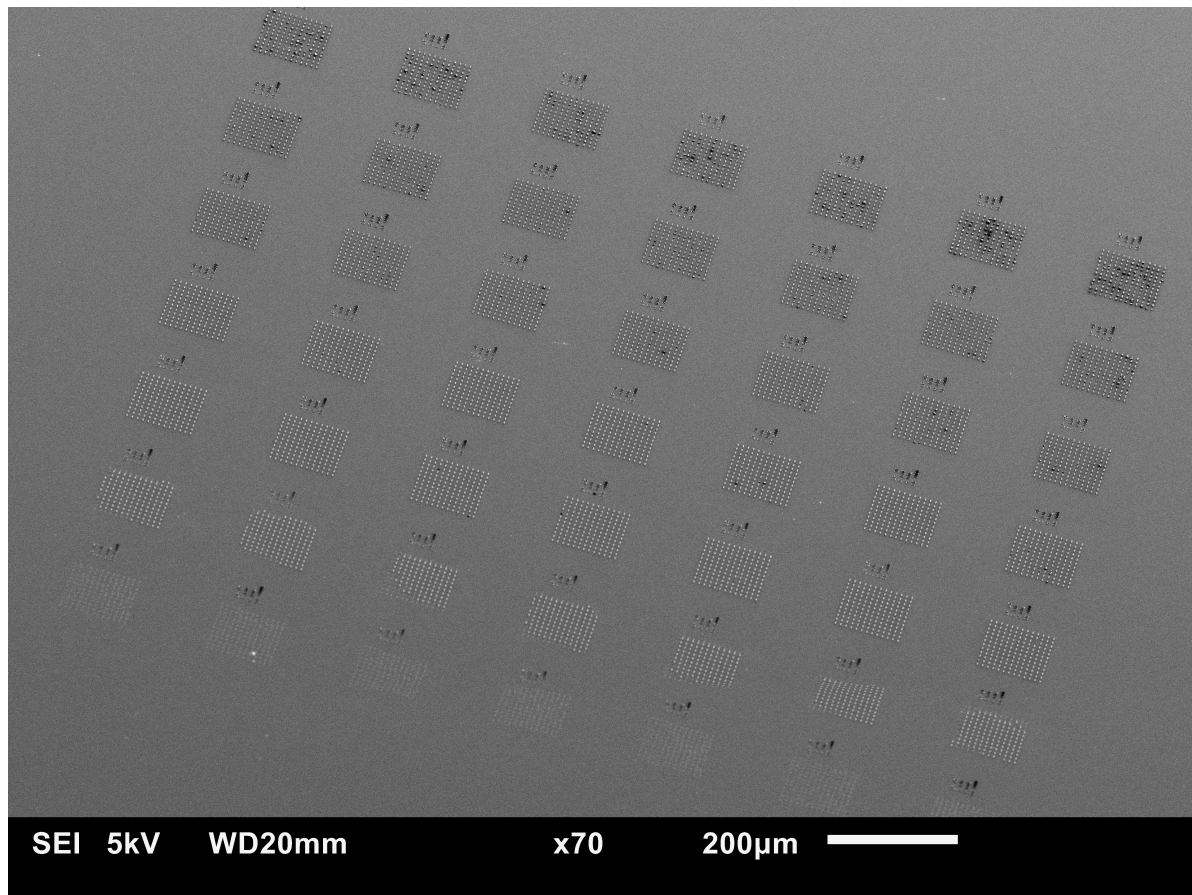
Figure 4.3: An example of a parameter optimization for a nanopillar array. The laser power was varied from 7.5 mW (bottom row) to 22.5 mW (top row), scanning speed was varied from 1 mm/s (right column) to 13 mm/s (left column). It can be seen that for the lowest laser power (bottom row) the structures are less defined and smaller than the highest laser power (top row). However it can also be seen that at the highest laser power some pillars are burned. Although we would expect more burned pillars for the lower scanning speeds (right column) than for the higher scanning speeds (left column), this seems to be not the case.

the spacing distance of the pillars influenced the color the array appeared to have optically. When the array had a uniform color, it meant that there was no pattern collapse. If there were dots or blurs in the color, the pillars were collapsed. This is presented in Fig. 4.5. For both arrays the pillar diameters are 250 nm and height is 1000 nm. The center-to-center spacing was 400 nm for the first array and 500 nm for the second. With the Keyence the individual pillars could not be seen, however a change in color indicated the difference in pillar spacing. In the first array some pillars were locally collapsed, which was clear to see with the SEM but could also be seen with the Keyence as being black blurs. The second array did not contain collapsed pillars, indicated with a uniform color when looking with the Keyence and confirmed with the SEM. The Keyence digital microscope was therefore a good tool to check if the nanopillars were upright, without the need of coating the nanopillars with Au/Pd.
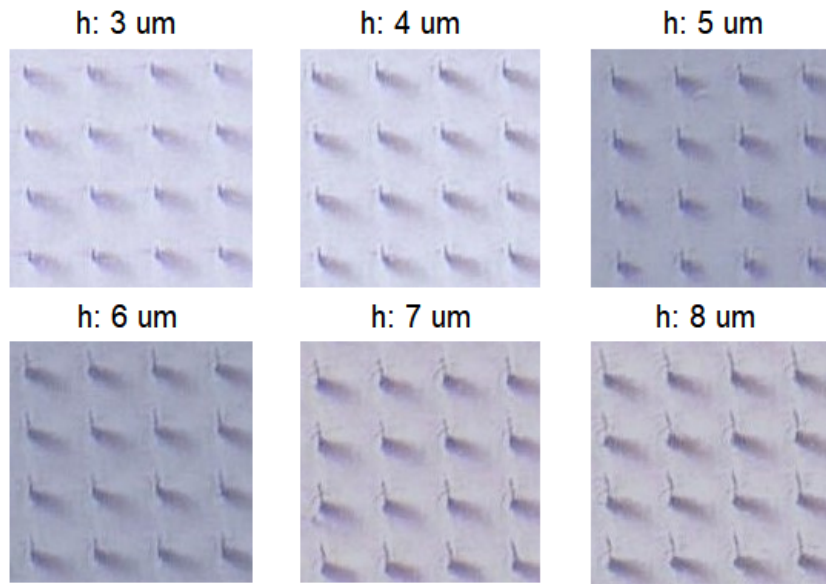
Figure 4.4: Figure shows nanopillar images made using the multi-light tool of the Keyence digital microscope when placed under an angle of 15°. The diameter for all pillars is around 250 nm. The height of the pillars is increasing for each array. We can indeed see this difference for the varying heights, meaning that this tool can be used to check the pillars uprightness and relative height.
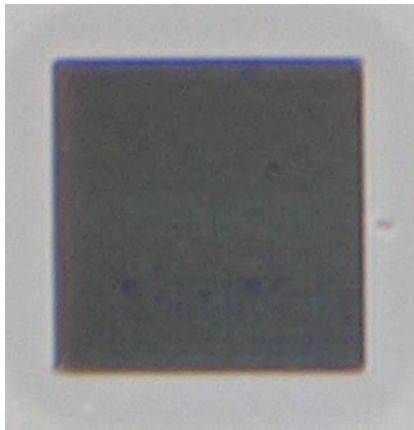
(a) Array 1: Keyence.
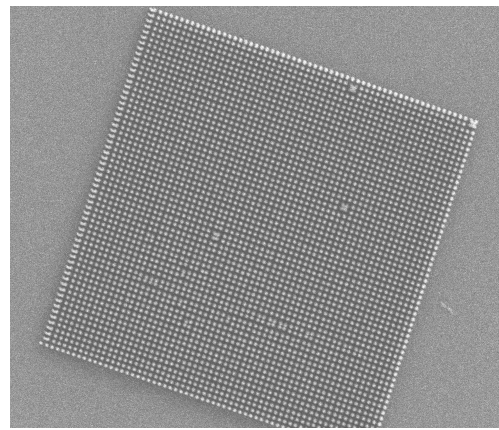
(b) Array 1: SEM.
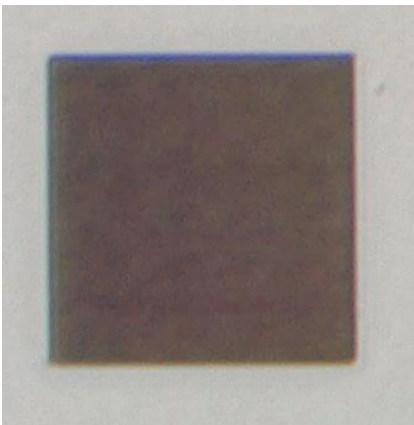
(c) Array 2: Keyence.
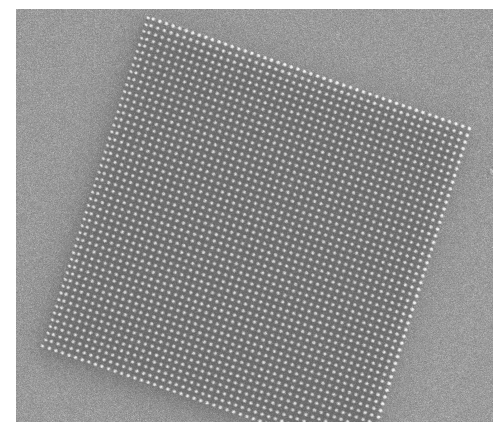
(d) Array 2: SEM.

Figure 4.5: Figure shows two different 25 μm wide nanopillar arrays, both imaged using a Keyence digital microscope (a and c) and a scanning electron microscope (SEM, b and d).

4.4. Factors that influence the pillar diameter

The resolution that can be achieved with two photon polymerization is directly linked to the size of the voxel. To summarize from Chap. 2, the variables that influence the voxel size are:

1. **Writing parameters**
   Parameters like laser power, exposure time and numerical aperture of the objective affect the electron density at the focal point, influencing the probability of radical formation and thus polymerization [77].

2. **Material properties**
   Properties of the resin, like two photon absorption effectiveness and the density of radical molecules define the very beginning of radical formation [90]. The amount of dissolved oxygen within the resin determines if the polymerization chain reaction is quenched, even before radical-radical termination ends the chain reaction. This can reduce the voxel size and lead to higher resolutions [83].

3. **Ambient conditions**
   These are environmental variables like temperature and humidity [73, 95]. The influence also became apparent during this research, however a direct correlation was not found.

In this research the diameter of the pillars was varied by adjusting the laser power and the scanning speed (i.e. exposure time).

4.4.1. Laser power and scanning speed versus pillar diameter

The diameter of the voxel has a logarithmic dependency on the photon flux (i.e. the laser beam intensity or the laser power) and exposure time [77, 90, 91]. The diameter of a fabricated nanopillar strongly depends on the voxel diameter. The graphs presented in Fig. 4.6 show measured diameters versus the used laser power for various scanning speeds. The measurements do indeed show a logarithmic dependency on the laser power, indicated with the logarithmic trend lines. The R^2 values show a good fit ($R^2 = 0.97$ and higher) to the experimental data. The laser power does correctly follow the theoretical trend. However in Chap. 2 we found that some parameters are missing to make good predictions.

(a)   (b)

(c)   (d)
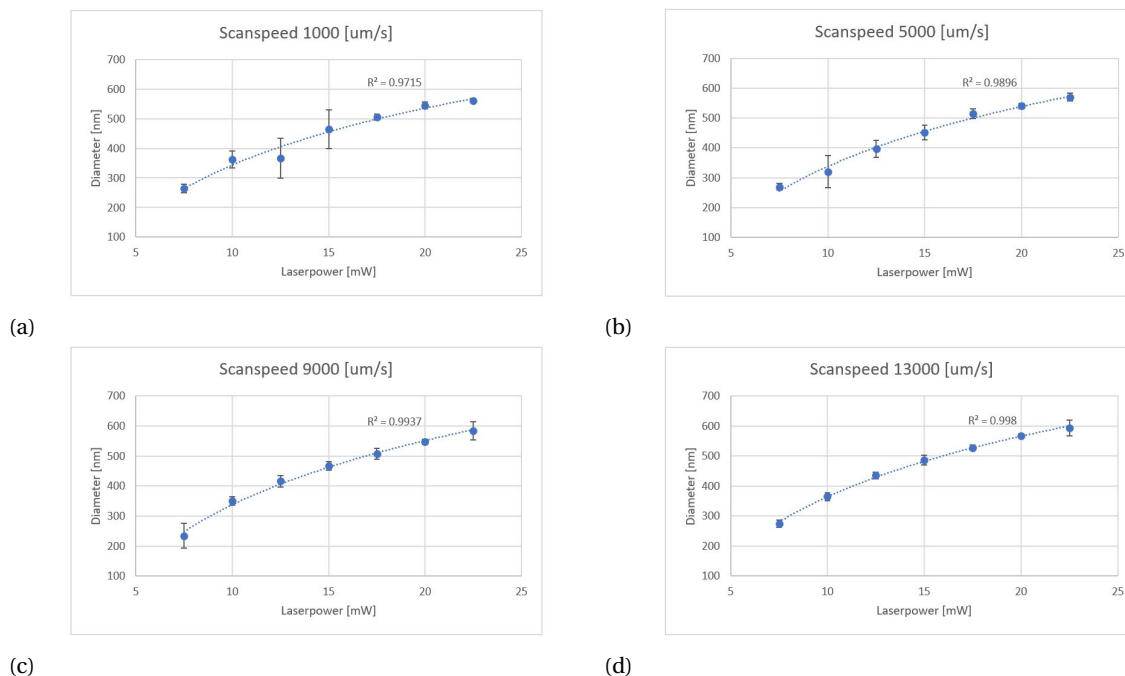
Figure 4.6: Measured mean diameters versus laser power for scan speeds a) 1 mm/s, b) 5 mm/s, c) 9 mm/s and d) 13 mm/s. Error bars indicate standard deviation of the measurements. Logarithmic trend lines show a good fit, with $R^2 = 0.97$ and higher.

Fig. 4.6 shows that the scanning speed, i.e. exposure time, does not influence the diameter as strongly as laser power does. The diameters related to a certain laser power seem to be very similar for varying scanning

speeds. To visualize this the diameters are also plotted versus scanning speed in Fig. 4.7a. Because theory always uses exposure time instead of scanning speed, they are transformed to exposure time (using the approach from Section 2.5) and plotted in 4.7b. We can indeed see that scanning speed or exposure time does not show the correlation to diameter as it should have. The diameter should increase with an increasing exposure time, which is not the case. One possibility is that this is due to the layer-by-layer writing fashion of the pillar arrays. In radical chain polymerization the typical value for the average lifetime of a growing radical lies between 0.1 and 10 seconds [96, 97]. The writing time of a single array layer is shorter than the lifetime of the growing chains, i.e. the material's polymerization chain reaction termination. This causes the effective exposure time to increase, leading to the irregular trend.

(a)   (b)
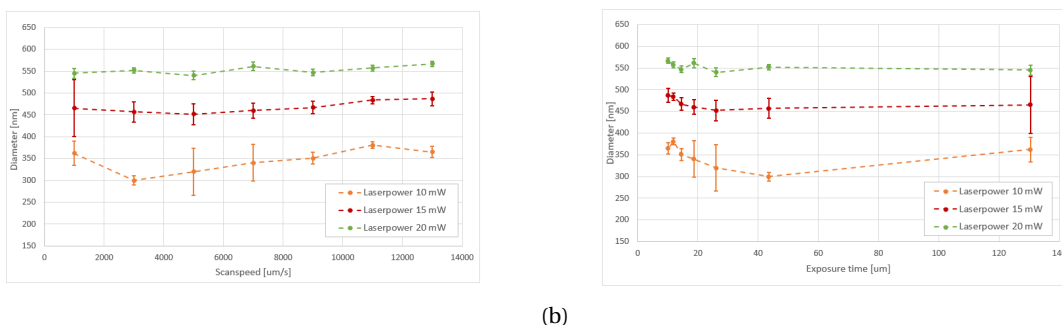
Figure 4.7: Diameter versus scanning speed (a) and exposure time (b).

By writing the pillars in a layer-by-layer fashion we were able to change the writing parameters throughout the pillar itself. This would not be possible with the 'import-STL' function of Describe (Nanoscribe GmbH), that automatically creates a job-file for an imported 3D CAD model. By keeping the design diameter at 100 nm and changing the laser power, pillars were created with varying diameters. By changing the laser power throughout a pillar, the shape of the pillar could be manipulated as shown in Fig. 4.8.

The need for this arose from the fact that small diameter pillars seemed to collapse more than thicker pillars. This approach was used to print pillars with a bigger base diameter and a thinner top diameter, under the premise that those pillars collapsed less. Eventually a completely different approach was taken to avoid pillar collapse by using a critical point drying technique. This is discussed in detail in Chap. 5.

(a)   (b)   (c)
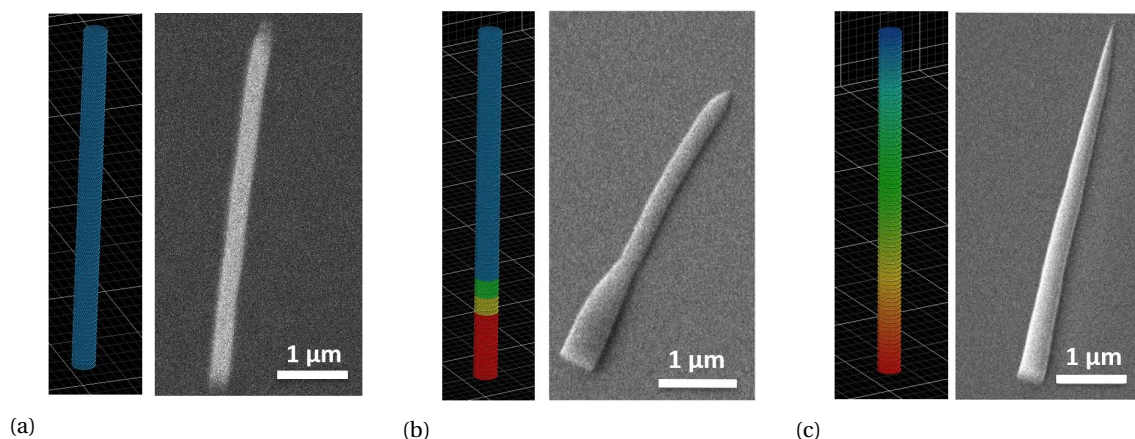
Figure 4.8: Differently shaped pillars by varying the laser power throughout the pillar. On the right of each picture a SEM image of a nanopillar, with on the left of each picture a corresponding schematic view of the laser power within that pillar, red being high and dark green being low laser power. Scale bars are 1 um.

4.5. Reproducibility

Most of the variables in Section 4.4 were kept constant for all experiments. Nonetheless the reproducibility of results was proven very cumbersome. in the first iterations very irregular burning patterns appeared. Low laser powers caused the resin to burn, whereas higher laser power printed the structures without burning. Using identical parameters for a next experiment led again to different results. This has also been reported by Folkertsma et al. who thought this was possibly due to local variations of the concentrations of initiator and monomer within the resin, or due to scattering of the laser within the resin changing the actual intensity [98]. A possibility investigated in this research was the cleanliness of the glass cover slip on which the structures were printed. To clean the glass cover slip, Nanoscribe GmbH advised on a certain cleaning procedure. First the cover slip should be rinsed with acetone and then blow dried. Then it should be rinsed with IPA and again blow dried. By eye it could be seen that the cover slip was still not completely clean. A soft cloth was introduced, to wipe the glass cover slip after each rinsing step. Spending more time on cleaning the glass cover slip, by repeatedly rinsing with acetone and IPA and rubbing with a soft cloth, showed much better results. The irregular burning at low laser powers did not occur afterwards.

The pillar diameter however still varied throughout the experiments when identical writing parameters were used. It is believed that this was being caused by power fluctuations due to minor defects or misalignments occurring in the optical setup. Over time we noticed a decrease in achieved pillar diameter when using the exact same printing parameters. Data spanning several months was combined to visualize this decrease, which is presented in Fig. 4.9. For every month the plotted data was obtained within one week using identical parameters and conditions. Over time, different laser power regions were investigated, causing the variation in data point regions. For the first three months (Fig. 4.9a) the measured diameters were decreasing, meaning that the effective laser power reaching the substrate decreased. When the complete machine was recalibrated by a technician from Nanoscribe GmbH, the diameters became again larger. This led to believe that over time, the effective laser power decreased due to growing misalignments within the optical path. It is therefore important to always do a dose test before a sample has to be printed. It would be also good to look into installing a measurement device to measure the laser power output directly at the sample, before a printing job is started, for calibration.

(a)   (b)
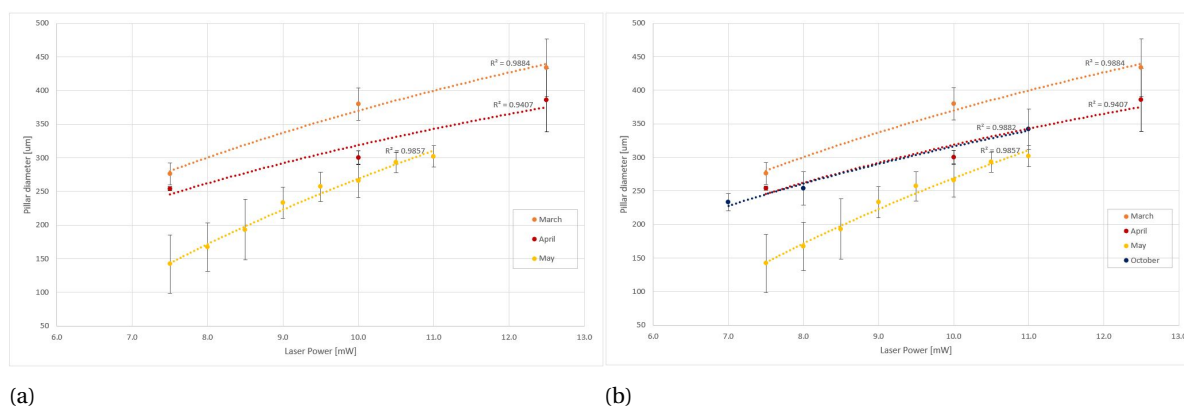
Figure 4.9: Decrease in measured diameter versus laser power spanning three months (a) and an additional month (b) which was after recalibration of the machine by a technician from Nanoscribe GmbH. The diameter decreased over time, but increased again after recalibration. Scanning speed was 3 mm/s for all experiments.

4.6. Conclusions and recommendations

Our approach can be used to directly write nanopillar arrays with varying pillar diameter, height and spacing by tuning writing parameters. Afterwards the Keyence digital microscope can be used as an inspection method to check the uprightness of the nanopillars without the need of coating the sample with Au/Pd. Also we can write shaped nanopillars by varying the laser power throughout the nanopillar.

It is important to carefully clean the glass cover slip to avoid irregular burning at low laser powers. Also a dose test should be performed before a sample is produced, or the laser dose should be measured at the sample for calibration.

Pillar Stability

There are several ways that can cause a nanopillar to collapse. On this length-scale the pillars do not collapse or buckle due to gravity, but rather due to adhesive forces between the pillars or between the pillar and substrate. This is due to scaling laws, meaning that for smaller pillars the ratio of pillar surface area to pillar volume increases, giving more dominance to surface forces. When multiple pillars are spaced very closely together the adhesive forces can pull them towards each other, called lateral collapse. Adhesive force between the substrate and pillar can also pull the pillar down, called ground collapse. Lateral and ground collapse only depend on material properties and pillar geometry. Pillars can however also collapse due to capillary forces when they are immersed in liquid and dried. In this chapter the stability of pillars is investigated. First the theory regarding the different modes of collapse is described, after which this theory is applied to the experiments of our research.

5.1. Theory

5.1.1. Lateral and Ground Collapse

From literature we can find a critical aspect ratio above which the pillars will collapse laterally. For this Glassmaker et al. combined the bending energy of a pillar that is laterally collapsed and its deformation energy with the adhesion energy between laterally collapsed pillars. This was rewritten by Chandra et al., yielding Eq. 5.1 [99, 100].

$$\left(\frac{h}{d}\right)_{c,lat} = \left(\frac{3^{3/4}\pi E s^{3/2}}{2^{1/4}32\gamma_{sv}(1-v^2)^{1/4}d^{1/2}}\right)^{1/3} \tag{5.1}$$

To find the critical aspect ratio above which a pillar will ground collapse, Roca-Cusachs et al. combined the bending energy that a pillar has when it is ground collapsed with the adhesion energy of that pillar with the substrate, yielding Eq. 5.2 [101].

$$\left(\frac{h}{d}\right)_{c,gr} = \frac{\pi^{5/3}}{2^{11/3}3^{1/2}}(1-v^2)^{-1/6}\left(\frac{E}{2\gamma_{sv}}\right)^{2/3}d^{2/3} \tag{5.2}$$

In these equations v is the Poisson's ratio of the pillar material, h is the height of the pillar, d is the diameter of the pillar, s is the lateral spacing between pillars and γ_{sv} is the surface energy of the pillar material.

5.1.2. Collapse due to Capillary Force

Liquids tend to occupy the least amount of space possible. It is less energetically favorable for a molecule to be on an outer surface than to be in the bulk surrounded by other molecules. Therefore a system of molecules tries to form the smallest surface area that is possible, which causes a droplet in air to form a circular shape. This pulling together of molecules is called surface tension, γ_{lg}. On a similar note we can look at solid material. It is again energetically less favorable to be situated at a surface, which causes a bulk of material to stay together. In the bulk the molecules of the material are all bonded together, but at the surface these bonds are nonexistent. There is an excess of energy at the surface, called surface energy γ_{sg}. As these surface energies are between the interfaces liquid-gas and solid-gas, naturally there is also a surface energy between solid-liquid, γ_{sl}. A system of these three phases always tries to minimize the sum of the interfacial energies, combined into Young's equation Eq. 5.3:

$$\gamma_{sg} = \gamma_{sl} + \gamma_{lg}cos(\theta) \tag{5.3}$$

where θ is the contact angle of the liquid. A contact angle of $< 90°$ means that a liquid is attracted to the surface and 'wets' the surface. The surface energy of the solid is stronger than the surface tension of the liquid,

and the solid surface is called hydrophilic. When the contact angle is > 90° the solid surface repels the liquid, and is called hydrophobic. The surface tension can exert different forces on our nanopillars, based on the geometry of the pillar arrays. The two most important forces, as described by Chandra et al. [100], are briefly discussed.

When the pillars are partially immersed in a fluid, with the fluid around the whole circumference of the pillars, the tip of the pillars feel a force due to the capillary meniscus which appears between the pillar tips (Fig. 5.1a). Chandra et al. combined this capillary meniscus interaction force with the elastic restoring force of the pillar and obtained an equation to calculate the critical Young's modulus (Eq. 5.4) for a pillar array with a certain geometry to be stable:

$$E_{crit,cap} = \frac{32\sqrt{2}\gamma_{lg}cos^2\theta h^3}{3d^4}f(r) \tag{5.4}$$

where $f(r)$ is a function that depends on $r = s/d$ (center-to-center spacing / diameter) [102]. The function $f(r)$ is not displayed here because it would not add value.

When the liquid is isolated between pillars, isolated capillary bridges form and give rise to a lateral force on the pillar due to Laplace pressure difference (Fig. 5.1b). Chandra et al. also combined the force that is caused by this Laplace pressure difference with the elastic restoring force of the pillar to obtain the critical Young's modulus (Eq. 5.5) in this case:

$$E_{crit,lap} = \frac{128\gamma_{lg}h^3\left(3hcos\theta + s_{diag}sin\theta + \sqrt{9h^2cos^2\theta + 3hs_{diag}sin(2\theta)}\right)}{3\pi d^3 s_{diag}^2} \tag{5.5}$$

where $s_{diag} = \sqrt{2}s - d$ is the diagonal spacing between two pillars in an array of four.

Chandra et al. used this theory on high density pillar arrays and found that the critical Young's modulus using the Laplace pressure difference approach greatly underestimated the stability of the pillars. When nanopillar arrays dry in an even manner, isolated capillary bridges do not form that often. It was found that the capillary meniscus interactions forces play a much more important role.
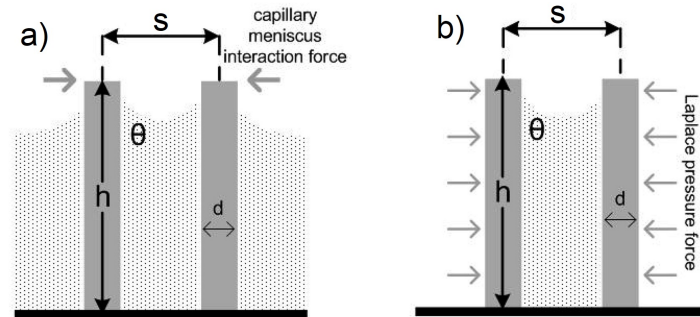
Figure 5.1: The two forces acting on a system of two pillars with liquid a) around the pillars and b) isolated between two pillars, reproduced from [100]

5.2. Applying the theory on the experiments
5.2.1. Stability of pillars printed on glass substrate
The theory is now applied to a couple of important cases. The first case depicts a pillar array of relatively large pillars with a large spacing. The second case depicts a pillar array of smaller pillars spaced densely together. Both were on the borderline of stability when tested for height and spacing, i.e. part of the pillars in that array collapsed and part remained upright. The arrays are shown in Fig. 5.2a-5.2b.

1. Different pillar arrays were printed with increasing height per array. From a 2000 nm height the pillars started to ground collapse.
   Diameter: 250 nm, height: 2000 nm, spacing: 8000 nm.

2. Different pillar arrays were printed with decreasing spacing per array. From a center-to-center (c-2-c) spacing of 400 nm the pillars started to laterally collapse.
   Diameter: 250 nm, height: 1000 nm, spacing: 400 nm.

Using Eq. 5.4 (capillary approach) and Eq. 5.5 (Laplace approach) the critical Young's modulus was calculated for the dimensions in these two cases. The rinsing liquid used was 2-propanol (IPA), with a surface tension of 21.7 mN/m. We do not know the contact angle of this rinsing liquid with the pillar material. Therefore the range from 0° to 90° was used. The results are presented in Fig. 5.4a. We can see that the capillary approach (red) gives similar results for the two distinct cases. Compared to this, the Laplace approach greatly overestimates the pillar stability in case 1, and underestimates the pillar stability in case 2. This makes sense as the Laplace pressure difference will be much bigger for pillars that are close together (case 2) than pillars further apart (case 1). When we assume a conservative contact angle of 40°-60° we can see that the Young's modulus of the material will approximately be 0.1-0.2 GPa. This is around one order of magnitude smaller than was found in literature [74] (see Section 2.3).

(a) Case 1.

(b) Case 2.
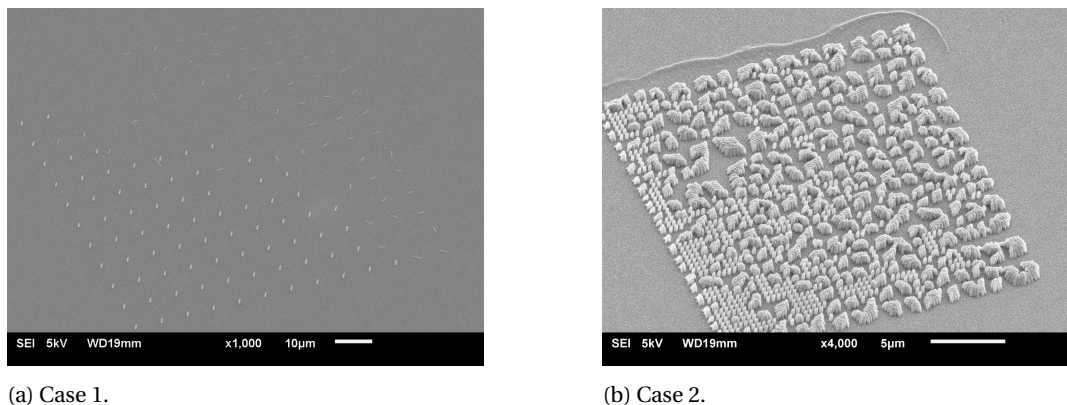
Figure 5.2: Scanning electron images of the pillar arrays showing a) ground collapse and b) lateral collapse.

5.2.2. Stability of pillars printed on a polymer base

The Young's modulus that was found, 0.1-0.2 GPa, does not match the expected value of 1.1-1.3 GPa [74]. From Fig. 5.2a-5.2b we can however see the problem for the previous approach. The pillars are indeed collapsed, either to the ground or laterally to each other, but it is not because their mechanical strength failed. We can see that the collapsed pillars are actually fully detached from the glass substrate. This means that the capillary forces do not bend and collapse the pillars, but overcome the adhesion of the pillar with the glass and collapse them to the ground.

This hypothesis is tested with data from two other experiments. In both experiments the pillars were printed on top of a polymer base and were therefore not attached to the glass. The particular pillar arrays are shown in Fig. 5.3a-5.3b.

3. First a baseplate was written after which the pillars were printed. Due to shrinkage of the polymer the baseplate detached from the glass at the edges, causing also the pillars at the edges to collapse. It can however be seen that the middle pillars are upright and all pillars are still attached to the base.
   Diameter: 380 nm, height: 5000 nm, spacing: 8000 nm.

4. These pillars were accidentally printed on top of a very dense array of smaller pillars. This was such a dense array that the small pillars actually form a baseplate. It can be seen that the pillars not printed on this 'baseplate' are detached, whereas the pillars on the 'baseplate' are still attached. The majority of these still-attached pillars are however collapsed.
   Diameter: 350, height: 6500 nm, spacing: 8000 nm.

When we now use the capillary approach (Eq. 5.4) and plot the critical Young's moduli for the contact angle range 0° to 90°, the results presented in Fig. 5.4b are obtained. Because the pillars in case 3 are still upright, the corresponding critical Young's moduli are taken as a bottom limit of our material's Young's modulus. The pillars in case 4 are on the borderline of full collapse and the results are therefore taken as the reference for our material's Young's modulus. When we again look in the region of 40°-60° contact angle the expected material's Young's modulus is around 0.7-1.7 GPa. This is much more in line with the literature.
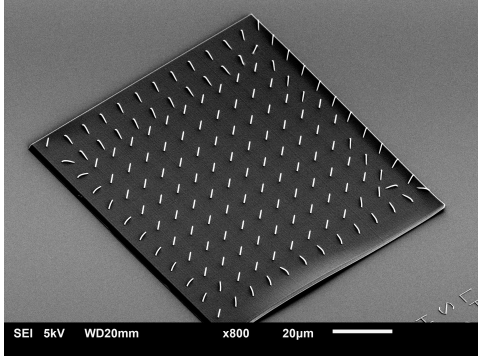
(a) Case 3.
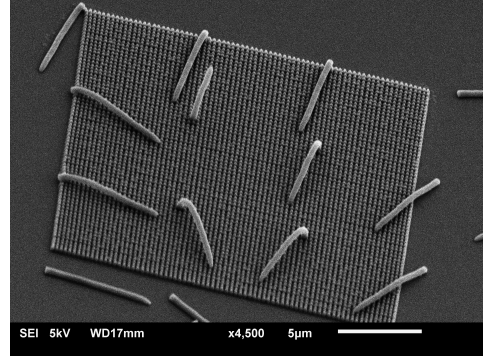
(b) Case 4.

Figure 5.3: Scanning electron images of the pillar arrays.
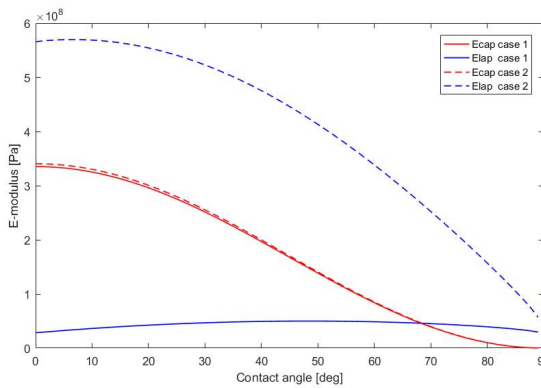
(a)
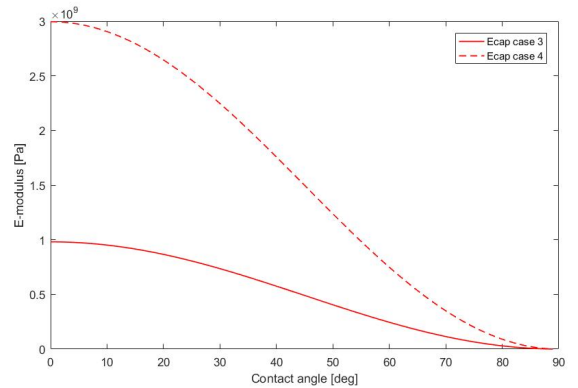
(b)

Figure 5.4: The critical Young's moduli for a) the first two cases based on the capillary meniscus interaction forces and based on the Laplace pressure difference, and b) the third and fourth case based on the capillary meniscus interaction forces.

5.2.3. Evaluating the proposed material properties

From literature the Young's modulus of IP-L 780 was found to be 1.1-1.3 GPa [74]. From the results in the previous section the Young's modulus is approximated to be in the range of 0.7-1.7 GPa. The material's surface energy was approximated to be that of pure Pentaerythritol triacrylate (PETA), found to be 41.2 mN/m [88]. These values are evaluated using Eq. 5.2, calculating the maximum AR before a pillar collapses to the ground. This would be in a situation without capillary forces acting on the structures.

The maximum aspect ratio we obtained during experiments was around 100: a pillar diameter of 250 nm and a height of 25 um. When we use Eq. 5.2 with the values: *d: 250 nm, γ_{sg}: 41.2 mN/m, E = 1.3 GPa*, we obtain a critical aspect ratio of around 80. This is less than the experimental AR. This means that either the Young's modulus should be considerably higher, around 2 GPa, the surface energy should be considerably lower, around 24 mN/m, or more likely a combination of both. To correctly predict the stability of the nanopillars, it is therefore paramount to know the exact material properties.

5.3. Circumventing the capillary forces with critical point drying

To make stable nanopillar arrays that do not collapse due to the capillary forces during drying of the rinsing liquid after printing we used critical point drying. With this method a sample can be dried while experiencing zero surface tension, thus eliminating capillary forces. The working principle of a CPD is explained in Appendix C and the protocol is presented in Appendix D. The effect of this method is visualized in Fig. 5.5. Array 1 in Fig. 5.5a-5.5b has a pillar diameter of 250 nm and a height and spacing of 8 μm. Array 2 in Fig. 5.5c-4.5a has a pillar diameter of 250 nm, height of 1000 nm and spacing 150 nm. It is clearly shown that (most) pillars do not collapse when the CPD was used.

(a) Array 1: without critical point drying.

(b) Array 1: with critical point drying.

(c) Array 2: without critical point drying.

(d) Array 2: with critical point drying.
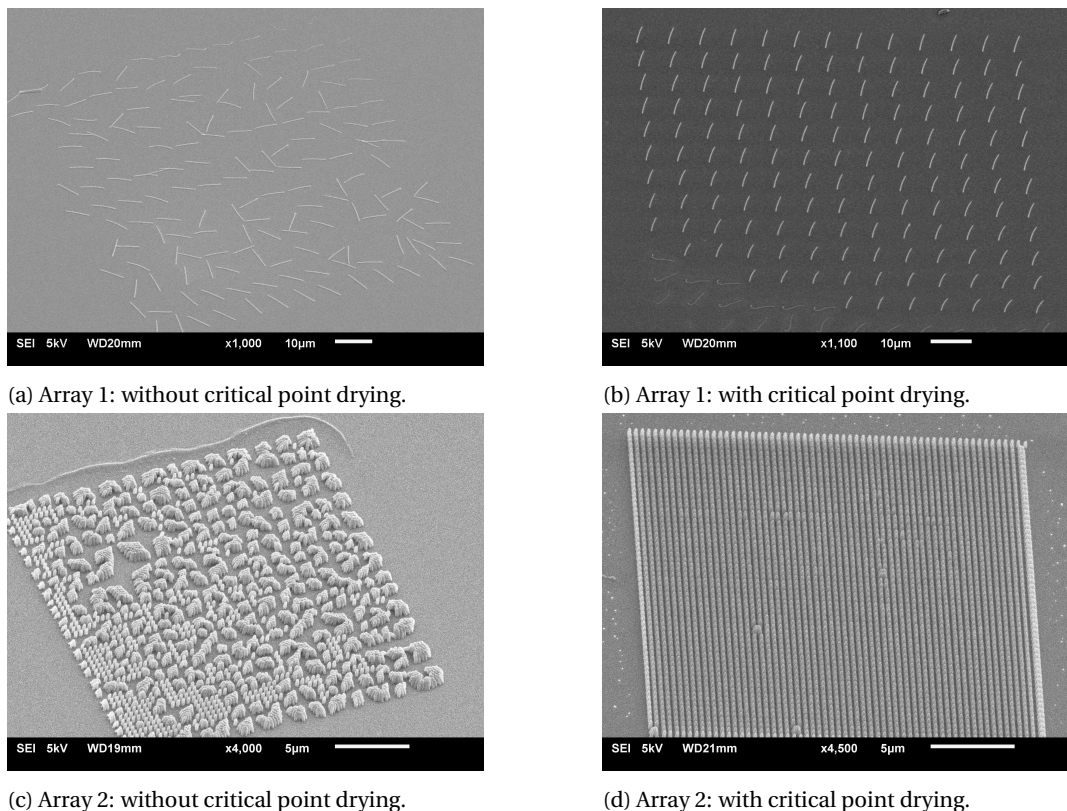
Figure 5.5: Figure shows two different nanopillar arrays, both air dried (a-c) and CPD dried (b-d).

5.4. Conclusions

When capillary forces are exerted on the nanopillars, the general mode of collapse is due to failure of the adhesion to the glass substrate rather than the mechanical strength of the pillars. When the pillars are printed directly on glass, the critical aspect ratio's are therefore much lower than predicted with the theory of Chandra et al. [100]. The capillary forces can however be eliminated by using critical point drying.

The values for the material properties proposed in Section 2.3 seem to be not exactly correct. Because we do not know the exact material properties we can not make good predictions on the stability of nanopillar designs. Therefore further research should be aimed at finding the following properties of IP-L 780: Surface energy γ_{sg}, contact angle with IPA and Young's modulus.

Experimental: Fabrication and Testing of the Microfluidic Chip

Conventional equipment measures the turbidity of a solution to determine the time it takes to form crystals in a liquid and uses this to derive the crystallization induction time. To relate the induction time to certain surface morphologies, a sample containing these morphologies is placed together with the solution in a glass vial and turbidity is measured [11]. Because of the stochastic nature of crystallization, many experiments need to be performed to make a statistical claim [10]. Because of the batch processing of two-photon polymerization (2PP), many samples should be produced which is not convenient. Based on the work of Laffite et al. [48], who also studied the crystallization of calcium oxalate (CaOx), we decided to use a microfluidic chip to perform our crystallization experiments. During this research several microfluidic chip designs have been tried and tested, described in more detail in Appendix E. Eventually a more basic design was proposed that enables us to perform multiple tests on a single chip. With this chip we performed preliminary crystallization experiments as a proof of principle.

6.1. Previous work

Laffite et al. [48] produced a two-inlet microfluidic channel in which calcium and oxalate precursors are mixed by diffusion at the liquid interface to study calcium oxalate (CaOx) crystal phases. Within the microchannel, which has similar dimensions as the human collecting duct (100 μm height and width), they used physiological concentrations and flow rates. The channel requires two inlets, one for each precursor and a single outlet. The precursors are aqueous solutions containing calcium chloride at 12.0 mM and sodium oxalate at 0.40 mM, which corresponds respectively to hypercalciuria and moderate hyperoxaluria commonly found in human kidney stone formers [48]. Both solutions were pumped through the microchannel at 1 μL/min. Within the microchannel they were then able to crystallize CaOx monohydrate (COM) and CaOx dihydrate (COD). This work was used as starting point and we included the kidney surface morphology to add complexity.

6.2. Chip design and fabrication

The microfluidic chip was composed of a polydimethylsiloxane (PDMS) slab containing multiple microchannels, covered by a glass cover slip to create a closed channel in between the PDMS and glass. The glass cover slip contained the structures written with 2PP, which are encapsulated by the microchannel walls. First a mold was produced with a high resolution 3D printer (Envisiontec Micro Plus Hi-res). The mold contained the negative version of the microchannels. PDMS elastomer and curing agent (Sylgard 184, Dow Corning) were mixed in a 10:1 ratio and poured in the mold. The mold was then placed in a desiccator for 30 minutes to remove air bubbles and afterwards placed in an oven at 70 °C for 1 hour to cure. After curing the PDMS was cut with a scalpel around the edges of the mold and peeled out. Holes for the inlets and outlets were punched with a 23G blunt end needle. The chip was assembled by eye in a clean room environment. The nanopillar arrays used in these experiments all contain nanopillars with a diameter of 250 nm - 350 nm, spacing of 8 μm and height of 6 μm - 8 μm. This uncertainty is due to the reproducibility issues as discussed in Section 4.5 and precise dimensions were not necessary for the first experiments. The dimensions do however resemble the primary cilia that are characteristic for the cells that line the collecting duct. Afterwards PE-10 tubing was inserted in the inlets and outlets and the chip was placed in a custom chip holder. This chip holder was made out of a transparent acrylate, laser cut top and bottom part hold together with four bolts and nuts (M5). With this holder we could make a reversible watertight seal between the glass and PDMS. The tubing was then

connected to a dual syringe pump (KD Scientific Legato 111) used to infuse separate fluids into both inlets.

The two precursor solutions enter the microchannel via separate inlets. Our final design, presented in Fig. 6.1, contained eight separate microchannels, each with two inlets and one outlet. The inlet and outlets have a radius of 0.5 mm to be small enough for the placement of multiple neighboring inlets, but still large enough for us to puncture tubing holes by eye. The width of the channels is 150 μm, somewhat larger than the channel width of the design by Laffite et al. This was due to limits we encountered with the 3D printing technique used to fabricate the mold. Because the mold contains a negative version, the channel appears as a protrusion in the mold. When this protrusion was 100 μm wide, it delaminated from the mold during drying. To create more surface area and therefore a better adhesion between the protruded 'channel' and the mold, the width was increased to 150 μm. For removal of the cured PDMS from the mold and to avoid leakage afterwards, it is paramount to have enough distance (a couple of mm) between the walls of the mold and the structures inside the mold. Also there should be enough distance between the individual channels. With trial and error the eight channels were placed in the mold as they appear in Fig. 6.1.
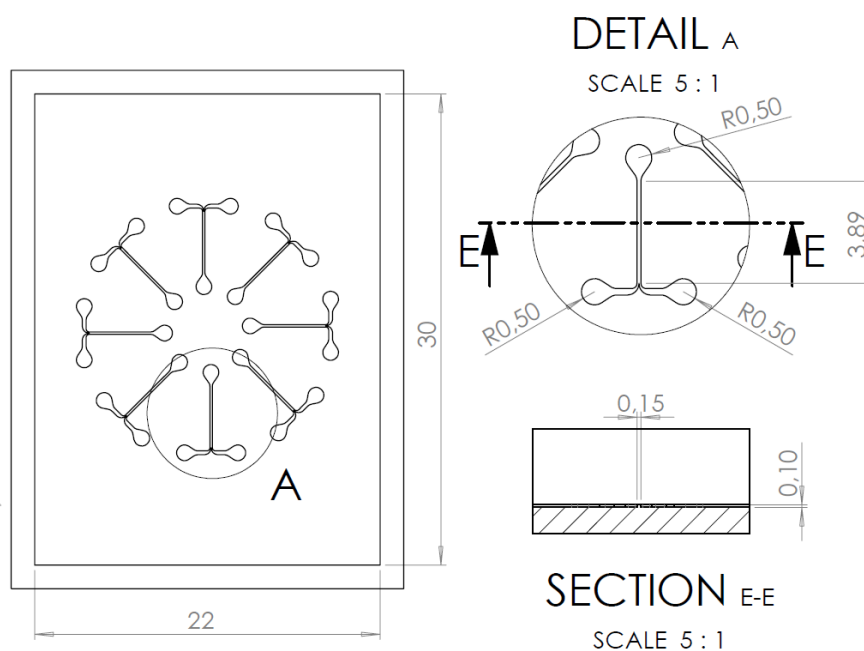
Figure 6.1: Final design of the mold for a microfluidic chip containing 8 separate microchannels. The dimensions are presented in millimeters.

The arrays of nanopillars on the glass cover slip were wider (400 um) than the width of the microchannel (150 um) to account for inaccurate positioning. The cover slip with nanopillar arrays and the microchannel could be aligned by eye. The dummy pillars stuck between the PDMS and glass did not cause any leakage during the following experiments. The complete device is presented in Fig. 6.2, also showing one of the eight microchannels and in the close-up the nanopillar array inside the channel.

6.3. First crystallization experiments and testing of the chip

6.3.1. Flow rates and type of flow

First a flow test was performed to determine if the seal between the PDMS and glass remained watertight. The flow rate was increased from 1 μL/min upwards while the channel was observed with an optical microscope. Up to a flow rate of 200 μL/min no leakage could be observed.

Because of the flow rate used (1 μL/min) and channel dimensions the flow should be laminar. This means that the two fluids flow parallel to each other and only mix through diffusion at the liquid interface. To test the laminar flow of the two inlet fluids, clear demi-water and demi-water colored with blue food coloring
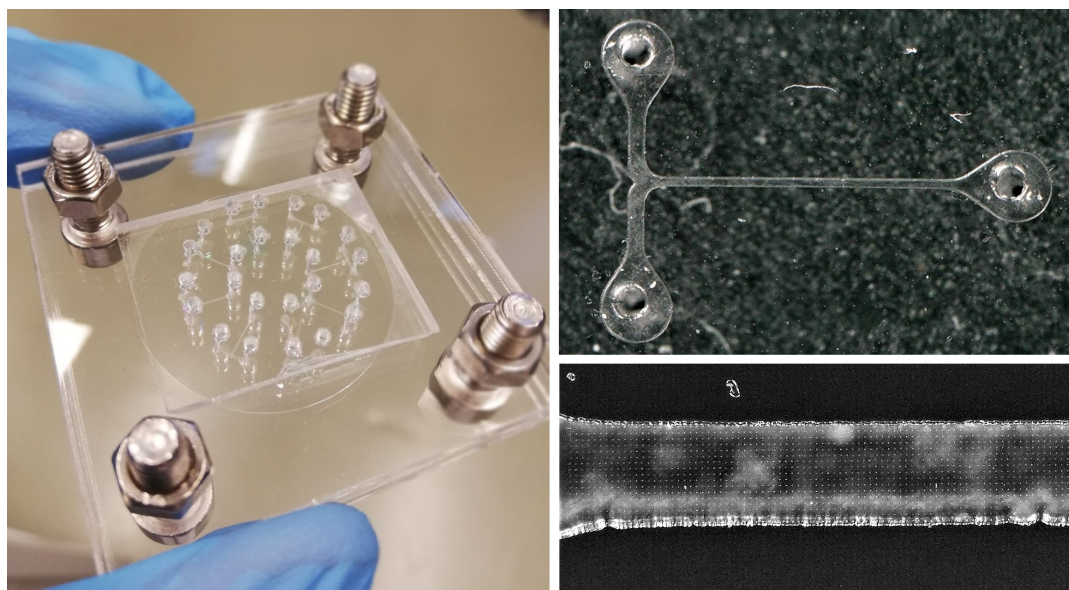
Figure 6.2: The transparent microfluidic device containing eight microfluidic channels (left). One of the eight microfluidic channels with two inlets and one outlet (top right). The array of printed cilia inside the microfluidic channel (bottom right).

were pumped through the channel both at a flow rate of 1 μL/min. The coloring of one fluid provided a visual aid to determine the interface between the two laminar flows. The interface occurred in the middle of the parallel flows, at the junction very distinctly and becoming less noticeable further along the channel due to diffusion (see Fig. 6.3a).

(a)

(b)
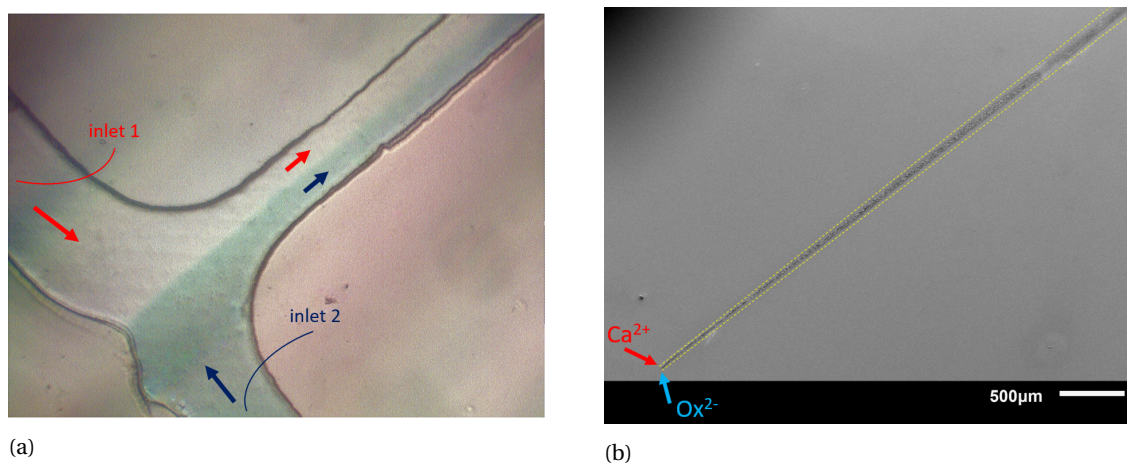
Figure 6.3: Figure a) shows the liquid interface between two laminar flows at flow rates of 1 μL/min. From inlet 1: clear water (red arrows); from inlet 2: blue colored water (blue arrows). Interface between the two flows is seen to be in the middle of the channel and diffusion is shown by the interface becoming less distinct. Figure b) shows the CaOx crystals formed along the length of the microchannel and deposited on the glass cover slip. the conical shape clearly indicates the diffusion of the ions from the start of the channel (lower left corner) along its length (towards the upper right corner).

6.3.2. Proof of principle

After the microchannel was tested for laminar flow and the interface appeared in the middle of the channel, a first experiment was performed to crystallize calcium oxalate. The microchannel was assembled on top of a glass cover slip that contained five nanopillar arrays with a length and spacing of 100 μm. Aqueous solutions of calcium chloride and potassium oxalate at both 8.0 mM were provided by Tsun Wang Yu at the Process & Energy department (P&E dept.) to be used as precursors. Two syringes were filled with the precursors, inserted in the dual syringe pump set to 1 μL/min and connected with PE-10 tubing to the microchannel. The fluids were pumped through the chip for two hours. This resulted in a channel filled with crystals. The chan-

nel was rinsed with ethanol at 1 μL/min to stop the crystallization reaction. The device was disassembled and the crystals on the glass cover slip were observed with an optical microscope and a scanning electron microscope (SEM).

The two precursors, one containing calcium ions, the other oxalate ions, come in contact at the fluid interface and diffusive mixing takes place along the length of the microchannel. CaOx crystals form at the interface. Fig. 6.3b shows a SEM image of the crystals that were formed along the length of the microchannel and deposited on the glass. The microchannel began at the lower left corner of the crystal line and the conical shape clearly indicates the diffusion of the solutions along the length of the channel towards the upper right corner.

Based on the shape of the crystals we could make an educated guess of the crystal phases, i.e. whether the crystal was COM or COD. The shape of our crystals was compared to literature to determine the crystal phase [103, 104]. Almost all crystals seemed to be COM but also an individual COD crystal was spotted, encircled in Fig. 6.4. It is logical that most crystals are COM, as this phase is thermodynamically more stable than COD [103].
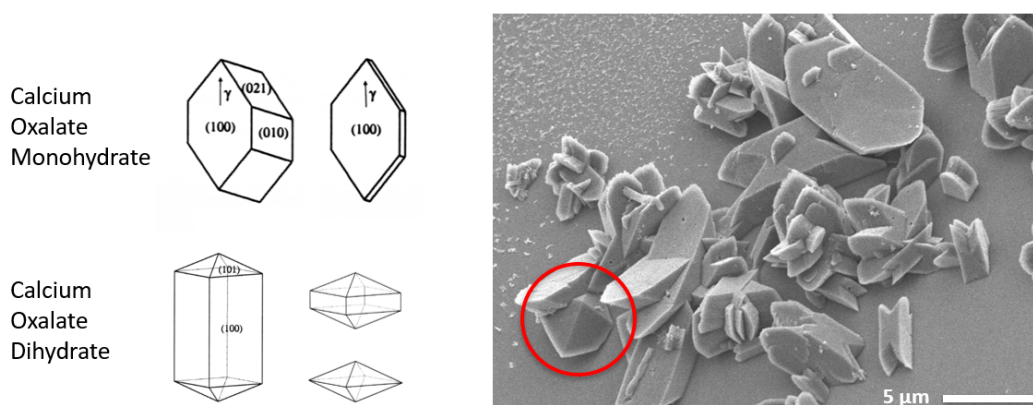
Figure 6.4: SEM image (right) of CaOx crystals formed in the first crystallization experiment. Most crystals are observed to be COM but also an individual COD crystal was spotted, encircled in the image. Crystal structures (left) are reproduced from [104].

6.3.3. Monitoring crystallization to determine induction time

We noticed that the areas with nanopillar arrays contained more crystals than areas without them. This could indicate that more crystals were formed amidst the pillars, but is is probably caused by the nanopillar array acting as a sieve, sifting out crystals that were already formed at another location in the channel and carried along by the fluid flow. We wanted to know whether the nanopillars influence the nucleation of crystals. Therefore in the next rounds of experiments the nanopillars were placed at the junction of the inlets, where the first crystals are formed, in order to avoid the sifting of already formed crystals. Also the transparency of the device was exploited by observing the channel while crystals were forming and a time lapse was made to determine induction times.

New precursors were prepared by Sanan Suleymanli (P&E dept.) with the molarities used in the work by Laffite et al.: aqueous solutions of calcium chloride and sodium oxalate at 12.0 mM and 0.40 mM respectively. A microfluidic chip was assembled that incorporated the nanopillar arrays in the microchannel at the junction of the inlets instead of further along the channel. The microfluidic setup (device + syringe pump) was complemented with the Keyence digital microscope to observe the experiment, capturing an image every 15 seconds. The experiment was run for 25 minutes, as it could be seen that at this time the channel was filled with crystals. Afterwards the images were used to determine when the first crystals were formed, which was at the 11th frame (165 seconds). The first and last image of the time lapse are presented in Fig. 6.5.

6.3.4. Collapsing pillars due to filling of the channel

We could not yet investigate the relation between crystallization rates and different nanopillar arrays, i.e. different surface morphologies. This was due to surface tension of the precursor liquids collapsing the nanopillars when the channel was filled, the exact same problem that occurred during the initial drying of the nanopil-
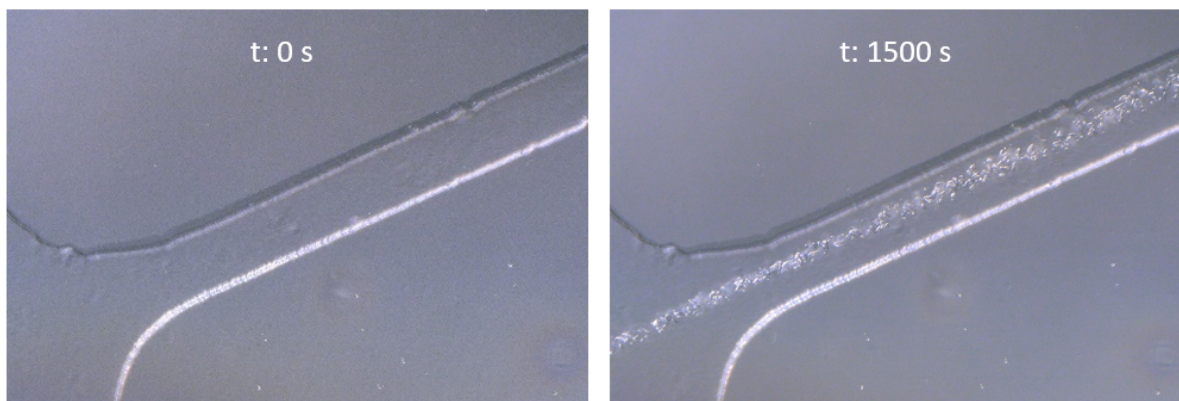
Figure 6.5: First and last frame of the time lapse for the crystallization experiment with aqueous solutions of calcium chloride and sodium oxalate at 12.0 mM and 0.40 mM respectively. After 165 seconds the first crystals were observed. The experiment was run for 1500 seconds, allowing sufficient time to fill the channel with crystals.

lars. The pillars are introduced to yet another liquid-gas phase boundary, i.e. surface tension. A solution to this problem was to fill the channel with ethanol first, then to replace the alcohol with the aqueous (precursor) solution. Alcohols have a lower surface tension than water which could be observed by the shape of the meniscus traveling through the channel. For demi-water is was convex (Fig. 6.6a) and for ethanol concave (Fig. 6.6b). The surface tension is approximately 23 mN/m and 73 mN/m for ethanol and water respectively [105]. The surface energy of the pillar material was assumed to be 41.2 mN/m (see Section 2.3.2). Water has a higher surface tension than the surface energy of the pillar material, causing it to stick together and push the pillars down as it travels through the microchannel. The surface tension of ethanol is lower than the surface energy of the pillar material, meaning it is attracted to the pillars. It pulls on the pillars, but the pulling force is in the opposite direction of the flow. Therefore it only wets the pillar surface and does not push them down.

(a) (b)
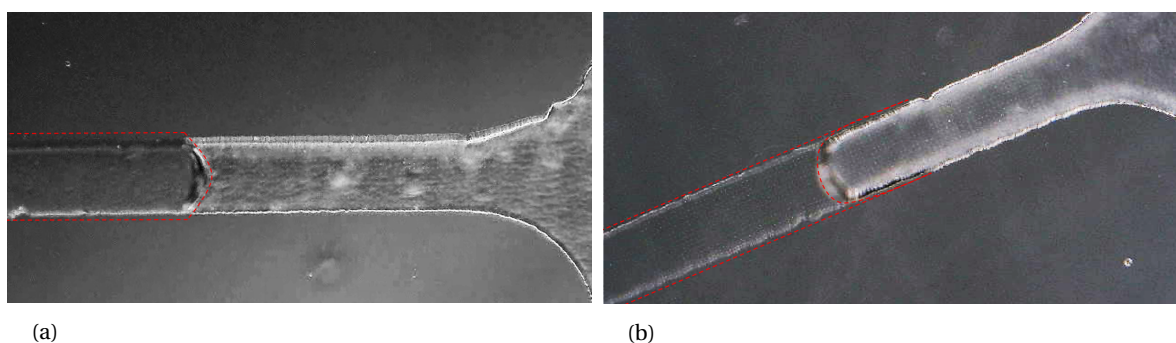
Figure 6.6: Filling the channel with a) demi-water and b) ethanol. The convex meniscus in a) and concave meniscus in b) indicate a higher surface tension for demi-water than for ethanol. The red dotted line is drawn around the fluid to guide the eye.

Although this approach worked well to fill the channel without pillars collapsing, air bubbles posed a big problem not easily solved. Whenever an air bubble traveled through the microchannel, another liquid-gas boundary is introduced. When the channel was filled with ethanol and an air bubble passed through, the phase boundary caused the pillars to collapse after all. This can be explained by the previous statement that ethanol is attracted to the pillars because its surface tension is lower than the surface energy of the pillars. When the air bubble passes through, at the liquid-gas boundary it pulls on the pillars. In this case the pulling force is in the same direction of the flow, causing the pillars to be pulled down. However the attraction of ethanol to its surroundings causes the air bubble to not occupy the full width of the channel. Ethanol sticks to the walls of the microchannel (see Fig. 6.7a), leading to no collapse of pillars at the walls of the channel (Fig. 6.7b).

6.3.5. Crystallization with ethanol in the channel

After filling the channel with ethanol to prevent the pillars from collapsing, syringes with precursor solutions were attached to the inlet tubing. Only some pillars located at the walls of the microchannel remained upright

(a)   (b)
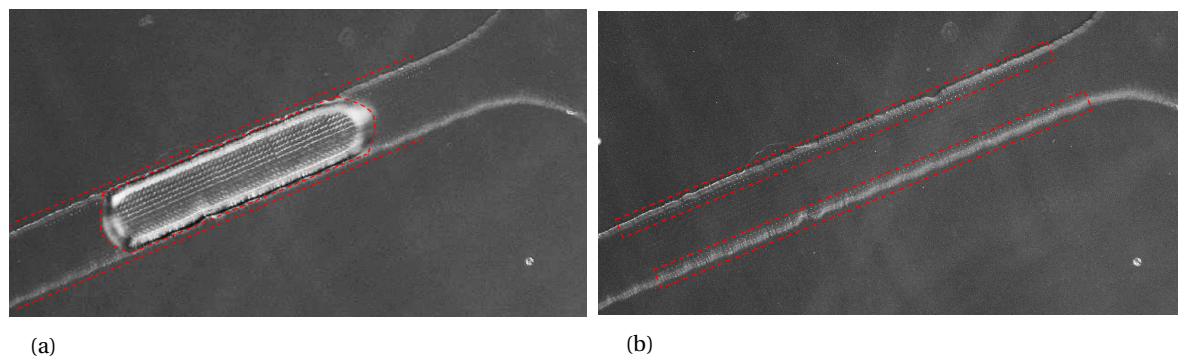
Figure 6.7: a) An air bubbles travels through the ethanol in the microchannel. The red dotted line is drawn around the fluid to guide the eye. The walls remain covered in ethanol. Therefore the pillars at the walls of the microchannel do not collapse, visible inside the red dotted boxes in b).

(see Fig. 6.7b). The precursor solutions were pumped through the tubing and microchannel at 1 μL/min. On entering the microchannel junction and coming into contact with each other, crystals began to form within the whole width of the channel. The solubility of CaOx is much lower in ethanol-water mixtures than in pure water [106], causing immediate crystallization. A result of this was crystallized pillars that did not collapse after drying, presented in Fig. 6.8. Because of the solubility drop of CaOx in ethanol-water mixtures, no ethanol may be present in the channel when the precursors are pumped in.

(a)

(b)
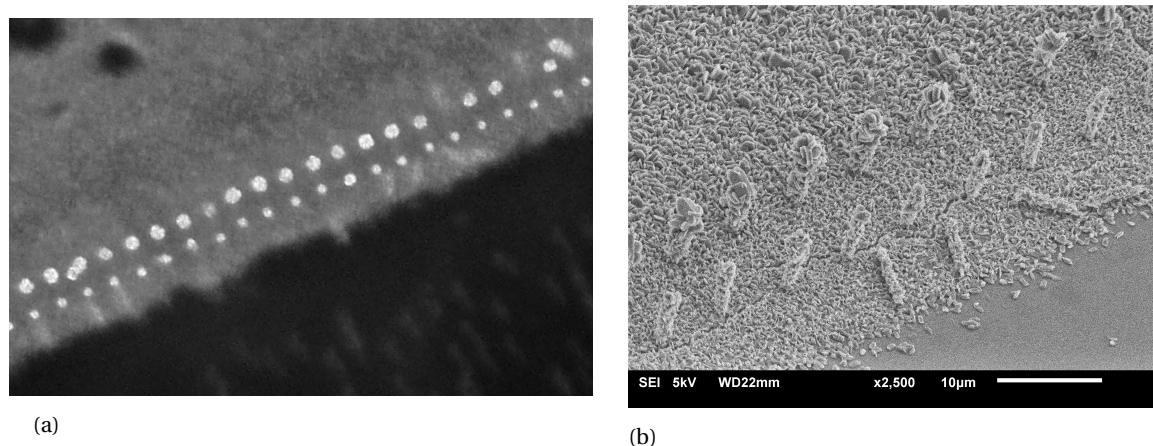
Figure 6.8: Crystallized nanopillars located at the wall of the microchannel due to immediate crystallization of CaOx in an ethanol-water mixture. Optical microscope image in a) and SEM image in b).

6.3.6. Proposed workflow

When ethanol is pumped through the microchannel at first, it should be replaced with water and only when all ethanol is completely rinsed out, the precursors can be introduced. The initial filling with ethanol should be done from the outlet towards the inlets. This is because otherwise the fluid passing through the tubing will not reach the two inlets simultaneously. One inlet will fill first, reach the junction and block the other inlet. This traps an air bubble at the second inlet, which in turn will collapse the nanopillars. After filling with ethanol, it should all be replaced with water before the precursors can be introduced. This is to prevent an ethanol-water mixture to develop which drastically decreases the CaOx solubility. The filling procedure requires disconnecting and connecting different syringes to the tubing. With a practical view it is quite impossible to perform these steps without trapping air in the system. Therefore the setup should be improved with bubble traps, that enable disconnecting and reconnecting of different syringes to the tubing. The setup and filling steps are schematically presented in Fig. 6.9.
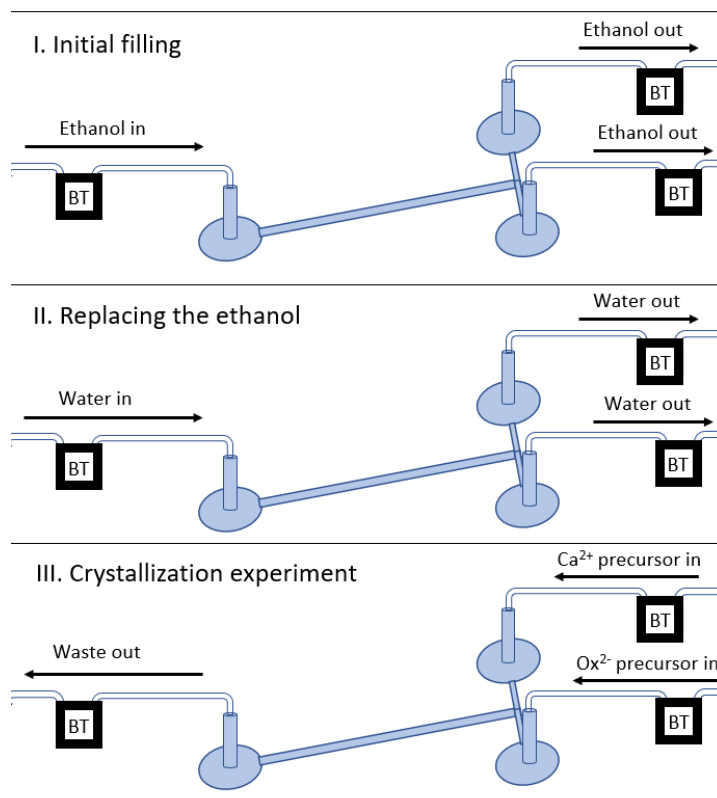
Figure 6.9: Schematic overview of the setup and steps to be taken for a crystallization experiment. The initial filling with ethanol should be done from the outlet towards the two inlets. Then the ethanol should be fully replaced with water before the precursors can be pumped through the microchannel to perform the crystallization experiment. The blocks with 'BT' are the bubble traps to prevent air from entering the system when different syringes are connected to the tubing.

6.4. Conclusions and recommendations

We successfully fabricated a microfluidic device in which we incorporated nanopillar arrays written with two-photon polymerization, and we used this device to crystallize calcium oxalate. We first reproduced the work from Laffite et al. by mixing calcium and oxalate precursors via diffusion in a two-inlet microchannel, and we added complexity by also incorporating biomimicking nephron surfaces in the form of nanopillar arrays. The device was tested to endure flow rates up to 200 μL/min without compromising the watertight seal between the glass and PDMS. In the first experiments we successfully crystallized both calcium oxalate monohydrate (COM) and calcium oxalate dihydrate (COD).

Maintaining the stability of the nanopillars within the channel is challenging but not impossible. It requires however a very different protocol, because the channel should be first filled with ethanol and replaced with water before the precursors can be pumped through. Air bubbles have to be eliminated for all these steps as they cause collapse of the nanopillars on passing through the microchannel. Therefore it is recommended to add bubble traps to the tubing, to allow for disconnecting and reconnecting of different syringes.

<div align="right">Chapter 7</div>

Conclusions and recommendations

Exploiting the opportunities provided by organ-on-chip technology, we designed and manufactured a microfluidic device proposed to increase our understanding of the relation between kidney surface morphology and the crystallization of calcium oxalate, the most common type of kidney stone. Surface morphology was already proved to influence nucleation rates but this has, to our knowledge, never been linked to kidneys and kidney stones.

We used two-photon polymerization (2PP) as a direct fabrication method to fabricate nanopillar arrays that mimic the nephron surface morphology. By varying the process parameters we could define the shape and size of the nanopillars. After optimization of the parameters we were able to write nanopillars with a minimum diameter of 145 nm ± 4 nm, nanopillar arrays with a minimum spacing of 157 nm ± 8 nm and nanopillars with an aspect ratio of up to 100, having a diameter of 254 nm ± 17 and a height of approximately 25 μm. With this we achieved to print nanopillars that 1:1 resemble the primary cilia found in the collecting duct of the human nephron.

We then fabricated a microfluidic device in which we incorporated the nanopillar arrays and we used this device to crystallize calcium oxalate. We first reproduced the work from Laffite et al. by mixing calcium and oxalate precursors via diffusion in a two-inlet microchannel [48] and we added complexity by incorporating the nanopillar arrays to mimic the nephron surface morphology. The device was tested to endure flow rates up to 200 μL/min without compromising its watertight seal. In the first experiments we successfully crystallized both calcium oxalate monohydrate (COM) and calcium oxalate dihydrate (COD).

The 2PP process contains a rinsing and drying step in which capillary forces are introduced to the nanopillars. When capillary forces are exerted on the nanopillars, it was found that the general mode of collapse is due to failure of the adhesion to the glass substrate rather than the mechanical strength of the pillars. When the pillars are printed directly on glass, the critical aspect ratio's are therefore much lower than predicted with the theory that was discussed in Chapter 5. The capillary forces can however be eliminated by using critical point drying. A protocol was composed for the Emitech K850 Critical Point Dryer that was installed for this research.

In multiple chapters we concluded that certain parameters are lacking, preventing us from making good theoretical predictions regarding pillar size and pillar stability. Although we mostly had to depend on experimental results, the theory provided insights and could be used to check trends that were identified during the experiments. To gain a better understanding of the processes we need to link the experimental data to theoretical models. Therefore future research could be aimed at finding and determining the material properties of IP-L 780. The properties that lacked in this research were:

- The TPA cross-section σ_2, threshold radical density ρ_{th}, initiator particle density ρ_0 and threshold energy for polymerization E_{th} to calculate the resolution limits of the material when used with 2PP.

- Surface energy γ_{sg}, contact angle with IPA and Young's modulus to make better predictions on the stability of nanopillar array designs.

Maintaining the stability of the nanopillars within the microchannel when they were reintroduced to liquid also proved to be challenging. It required a new protocol, filling the microchannel first with ethanol and replace this with water before the precursors could be pumped through. Air bubbles had to be eliminated for all steps as they cause collapse of the nanopillars on passing through the microchannel. Therefore it was recommended to add bubble traps to the tubing, to allow for disconnecting and reconnecting of different syringes.

Chapter 8

Reflection

In this chapter I reflect on the work, planning, process, experiments, equipment, guidance and personal growth of the past year's work.

The literature review confirmed to me that I really like, and maybe even need, a broad field to work in. Unlike what I hear from most colleagues, I actually very much enjoyed doing the literature review. I have always liked to read which was beneficial for the amount of papers I studied for this research. The topics were very broad, at the start of the review almost exclusively related to biology and kidney pathology, later more to technology and physics. This variation in topics gave me a lot of energy and motivation to keep reading and learning.

Diving deep into the theory of photon absorption also brought me into the quantum realm. This was a challenging topic and I am glad that Urs was there for me, with whom I could discuss some of the counterintuitive problems that quantum theory brings. For me it was important to understand, but when looking at the bigger picture it did not fit perfectly well within the report itself. Therefore I moved it to the appendix. The photon absorption theory was followed with two-photon absorption and polymerization theory. Here I believe to have shown good analytical skills that I learned during my study. The vast amount of papers were interesting but still needed to be combined into a coherent story. I picked out the important matter and made connections to other literature and also to my own experimental results. I always try to be critical when reading and this led me to find a mistake made in a very big review paper. There were missing terms in one of the equations, used in multiple papers. I spent a couple of days fully committed to solve the equation, and I believe to have found the missing terms. Some of the derivations were difficult and I am grateful that Daniel was there to bounce some ideas off.

The experimental work was also something that I liked. The reproducibility of the print jobs with the Nanoscribe was challenging for my results and frustrating for myself. I discovered however that with very careful cleaning of the substrate, the random burning of structures could me eliminated. In literature I found other reasons for this, but cleaning seemed to do the trick. Also my nanopillars kept collapsing and I performed a lot of experiments and many observations to find the reason for this: surface tension during drying. I read about a solution to avoid surface tension by using a critical point dryer. I found out that PME owned one, put away in storage, and approached Luigi and Rob to explain them the necessity of the machine. Our technicians installed the machine, however I was already more than half way through my project and the protocol had to be figured out first. This also took a long time and late October I finally discovered how to properly use the machine. I believe that, despite the many experiments and time it took, it will add a lot of knowledge and benefits to the department and to other research. Therefore it is time well spent.

During the project I really learned to work effectively, as I set out to do a lot of different things. I know from previous projects and courses that I work best independently, but within a master thesis project this is maybe not always the best approach. Regarding crystallization it was beneficial to reach out to the crystallization group at the Process & Energy Department. After Luigi introduced me to Fatma, the PhD student working in that group, I branched out my contacts and joined the weekly meetings. I learned a lot from them and in return I helped this group by making some microfluidic chips. From this experience I learned to reach out to another department and research group, to find a common goal and collaborate to achieve this goal. I also learned to stay focused at my own work and speak up for myself. Some experiments of the crystallization group had a slightly different aim than mine and I had to make sure that the things I wanted to investigate for my thesis also got the attention. When it came to testing I performed most crystallization experiments myself because this was more time-efficient as I did not have to depend on other people and equipment.

In Section 1.6 my original planning made after the literature review is presented. I achieved my main goals of producing the different surface morphologies and incorporate them into a microfluidic chip. The proof of principle was reached and now we have to continue to link crystallization to the different morphologies. Crystallization study needs many statistical experiments to be performed, therefore it is not remarkable that it could not be achieved within the time frame of this thesis.

After the first month we already decided to combine the second and third main task, which was performing a crystallization study on the surface morphologies and afterwards incorporating them into a microfluidic chip. Based on previous work we decided to incorporate the surface morphologies in a microfluidic chip from the start and use this chip to perform the crystallization studies. With a view on my planning this did not matter too much as I basically just combined these two tasks. However it proved difficult to combine the surface morphologies with the crystallization experiments, something I discussed in detail in Sections 6.3.4 to 6.3.6. I did not anticipate the huge effect that surface tension of liquids posed during this research and it was the largest contributor to experiments not going as planned. However I think that a good outcome was found and we learned a lot about the effects of surface tension and how to circumvent them.

When I started with my literature review I also started as board member of our study association (Dispuut Taylor). I believe that being active within our department and talking to the staff on a regular basis benefited my project. When making my planning I took the other work into account by scheduling 30 hours a week for the project and 10 hours for Taylor. With this distribution of hours and a workload of 50 ECTS, the project would be finished at the end of December. Because I eventually spent more time a week for Taylor, I had to catch up some work in the evenings and weekends. Having a lot of things to do taught me about time management. Almost every week I was making a planning for my short term goals for the upcoming weeks and now and then adjusting them to be more realistic in terms of time. I believe this really helped me to avoid having too much stress and I look back at it being a very fruitful year.

My presentation at the International MicroNanoConference (iMNC 2018) was very exciting and a nice appreciation of my work. Because this presentation was only 10-12 minutes I had to learn to be really concise, both in terms of presenting the work graphically on just a few presentation slides and also in terms of speaking by using concise statements. Something that I have to continue to learn is to be more confident to talk in front of an audience, to be more at ease. It was however a good practice for my presentation skills and a very nice experience.

Looking back at the project as a whole, I learned some of my personal characteristics. First of all I can work effectively whilst sticking to deadlines. I started with a lot of milestones and a very tight schedule and by the end of this research I have reached most of my goals. Secondly I can work independently, as I did not depend much on my supervisors to steer my direction. I learned to manage my own project and chase after the goals I set out to achieve. Thirdly I can be flexible. Around the summer I learned that my daily supervisor, Luigi, was leaving the department and Urs would take up the supervision. I think this transition went rather smoothly and I could continue the work I had set out to do. It even offered me the insights of both Luigi and Urs, which added depth to my work. Also I wanted to include work that did not fit into my own master's program and I therefore reached out and started working with another department. Lastly I learned to think critically, also about my own work. I tried to be involved in the weekly discussions we hold with our research group as well as the crystallization group and discuss the problems I am facing at the moment with my colleagues and the staff.

I am proud of the work and results of this master project and I hope it will bring forth new exciting research.

Photopolymerization and the creation of radicals

A.1. Introduction to Photopolymerization

In photopolymerization a photosensitive resin is used that can contain monomer, oligomer, photoinitiator and/or photosensitizer molecules [68, 70]. By the absorption of light a photoinitiator gets excited, leading to the creation of free radicals in the resin, which in turn trigger a polymerization chain reaction [75]. These radicals carry an unpaired electron and are very reactive. The radical attacks the double carbon bond within the monomer, resulting in a single carbon bond and a radical end. This process is called free radical polymerization. There are also other types of polymerization that can be used depending on the material. The material that is used in this thesis, IP-L 780 (Nanoscribe GmbH), is acryl-based [80]. Acrylates are usually polymerized with free radical polymerization [68], which is schematically illustrated in Fig A.1. In standard stereolithography this chain reaction propagates trough the resin until it is terminated when two radical ends meet. There is however a difference, after the formation of radicals, between local polymerization in 2PP and film polymerization in standard UV-stereolithography. The local polymerization in 2PP has a larger surface area to volume ratio compared to a polymerized film. Dissolved molecular oxygen in the resin inhibits free-radical polymerization, making it a more important factor in terminating the polymerization chain reaction in 2PP than radical-to-radical termination [83].
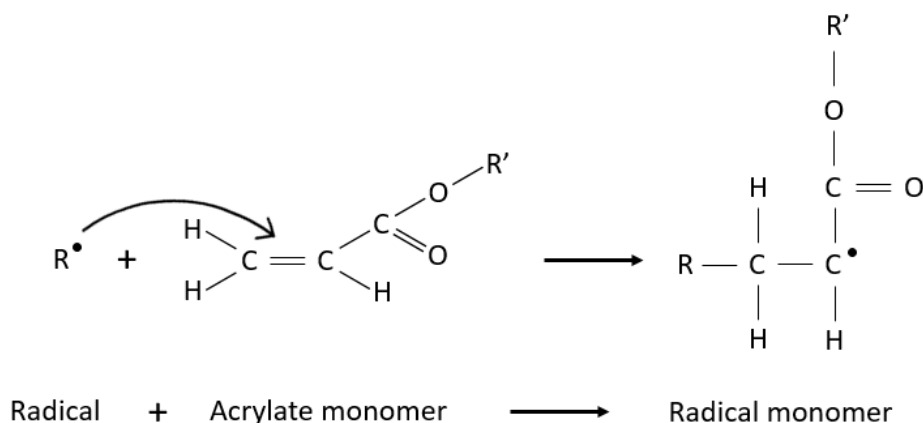
Figure A.1: A molecule with an unpaired electron, the radical, attacks the double carbon bond of an acrylate molecule. The acrylate molecule becomes a radical itself, setting up the polymerization chain reaction.

A.1.1. Photosensitive Molecules

As most monomers and oligomers are not photosensitive by themselves, meaning they do not produce reactive radicals when exposed by light, photoinitiators or photosensitizers are needed in the resin solution. Within their molecular skeleton they contain a part called the chromophore, which is responsible for the molecules color by absorption of particular wavelengths of light [107]. A common chromophore is the benzoyl functional group, which exhibits good photochemical behaviour in the ultraviolet (UV) wavelength range [68]. Benzil is a compound that is build out of two benzoyl groups and derivatives are commonly used as

photoinitiators [108]. Figure A.2 shows the reaction mechanism (α-cleavage) of a molecule that contains the benzoyl funtional group when exposed to UV light, creating two radicals. It is also possible that a photosensitizer is used, which readily absorps light and easily transfers this energy to another molecule via fluorescence [68, 109]. The receiving molecule, often the photoinitiator, then uses this energy to reach an excited state in which it can produce a radical.
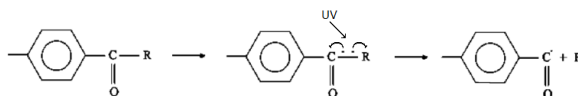
Figure A.2: Reaction mechanism of UV sensitive benzoyl chromophore in a photoinitator when exposed to UV light. The mechanism is called α-cleavage, the homolytic cleavage of the bond. Copied and edited from [68].

A.2. Photon Absorption

Quantum mechanics tells us that an electron can only have discrete values of energy, called energy levels or electronic states. In a molecule or atom, we say that when the molecule or atom is at its lowest energy level, it is at its ground state. When it, or any electron it has, is at a higher energy level than this ground state, we say that it is in an excited state. To illustrate these quantized electronic states, a Jablonski diagram is used (Fig. A.3).

This diagram usually shows a singlet ground state (S(0)), a singlet first excited state (S(1)) and sometimes even a singlet second excited state (S(2)). In a singlet state the electron spin of the excited electron is paired with the ground state electron, as the Pauli exclusion principle states that any pair of electrons in the same energy level must have anti-parallel spin. The singlet states are shown in a Jablonski diagram with thick horizontal lines, representing the different energy levels.

In each energy level, several vibrational energy levels can exist, shown with thinner horizontal lines. Transitions between states can now be indicated with arrows. A straight arrow indicates radiative transitions, by emission or absorption of light (photons), and squiggly arrows indicate nonradiative transitions, e.g. by means of vibrations.

Figure A.3: Jablonski diagram showing the the singlet ground state S(0) and the singlet first excited state S(1). By absorbing the energy of two photons ($2h\nu$) it is lifted from S(0) to S(1). Relaxation from the excited to the ground state can be by emission of fluorescence or by releasing heat.

Bohr's frequency condition (Eq. A.1) shows that during a radiative electronic transition of an atom from one

state to an adjacent energy state, the energy difference ΔE of these states is related to the frequency of the photon that is absorbed or emitted during this transition [110].

$$\Delta E = h\nu \tag{A.1}$$

This condition is a direct consequence of Planck's law (Eq. A.2 [109]), that calculates the energy of a photon:

$$E = h\nu = \frac{hc}{\lambda} \tag{A.2}$$

Here E is the photon energy, h is Planck's constant and ν is the photon frequency which is equal to the speed of light in vacuum c divided by the photon wavelength λ.

A.2.1. Single-Photon Absorption (1PA) and Two-Photon Absorption (2PA)

In the case of single photon polymerization that uses ultraviolet (UV) sensitive material, one UV photon, having a wavelength of around 300 nm, carries enough energy to trigger the electronic transition in the molecule from one energy level to a higher one. Two-photon polymerization makes use of near infrared (IR) light, typically around 780 nm [111]. As this wavelength is close to double the wavelength of UV, Eq. A.2 shows that this photon carries only half the energy compared to a UV photon. To excite the UV sensitive material with near IR photons, the absorption of not one but two photons is therefore needed.

A.2.2. Reaction Mechanism

The absorption of two photons by, in this case a photoinitiator or photosensitizer, can happen sequential and simultaneous. The latter is found to be the dominant mechanism [112]. The first photon is absorbed and the absorbing species is lifted from its ground state to a virtual excited state (Fig. A.3). The lifetime of this virtual state is very short, about 10^{-15} s, so the second photon should arrive within this virtual state lifetime for the species to reach its excited state [68]. This short lifetime is the reason for the need of a femtosecond pulsed laser with very high laser intensities. The excited photoinitiator can now decay back to the ground state and emit the absorbed energy in the form of light or heat or it can generate radicals due to a chemical reaction, which will initiate the polymerization chain reaction.

As mentioned, the atom can transition to another energy level either radiatively or nonradiatively. On absorption of a photon, the atom is excited to the next higher energy level and usually to a higher vibrational energy level as well. It then rapidly relaxes to the lowest vibrational energy level by means of vibrational relaxation (dissipating the energy into vibrational modes of the molecule, resulting in heat). From this excited singlet state the atom can go immediately back to its ground state by emission of fluorescence or by vibrational relaxation (Fig. A.3). Other nonradiative relaxation mechanisms are internal conversion and intersystem crossing. In internal conversion the vibrational state of a higher energy level can couple to a vibrational state of a lower energy level, eventually leading to one of the singlet states by vibrational relaxation. In intersystem crossing the same happens, but the molecular spin state changes. The electron flips its spin. It is now called a triplet state; the excited electron has reversed spin. From this excited triplet state T(1) the atom can go back to the ground state by emission of phosphorescence or vibrational relaxation. In photochemistry the excited triplet state of a molecule can also lead to α-cleavage, breaking a molecular bond and generating radicals (Fig. A.4).

To understand the formation of radicals, molecular orbital theory should be revisited.

A.3. Quantum theory

A.3.1. Wave-particle duality

De Broglie stated that each particle also has a wave nature, known as wave-particle duality. The wavelength of a particle can be calculated if we know its momentum. But with this wave description, according to Heisenberg's uncertainty principle, it is impossible to know the particles position and momentum simultaneously. In quantum physics there is a special function of position and time that can be used to determine everything that is known about the system, the wavefunction $\psi(r, t)$ [113]. To find the particle in a particular state, we can
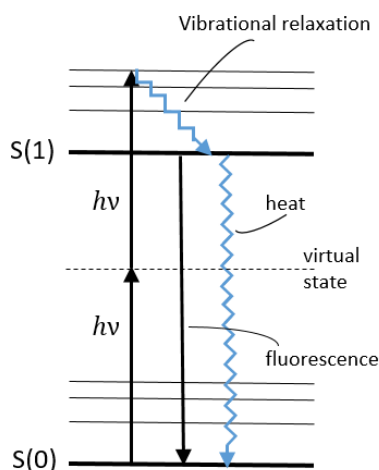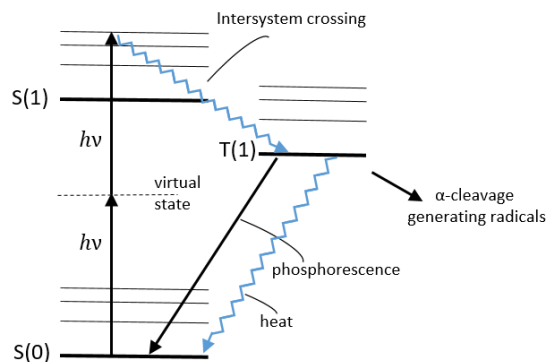
Figure A.4: Jablonski diagram showing the the singlet ground state S(0) and the singlet first excited state S(1). By absorbing the energy of two photons ($2h\nu$) it is lifted from S(0) to S(1). The excited electron flips it spin and goes via intersystem crossing to a triplet excited state T(1). The excited triplet state can now go back to the singlet ground state by emission of phosporescence or vibrational relaxation, or it can generate radicals through α-cleavage.

mulitply the wavefunction $\psi(r,t)$ with its complex conjugate $\psi^*(r,t)$, resulting in $|\psi(r,t)|^2$. This represents the probability density function [113]. With the wavefunction it is possible to obtain physical observables of the system, as each observable has a mathematical operator that can be used on the wavefunction. This is shown in Eq. A.3:

$$Q\psi = q\psi \tag{A.3}$$

where Q is the operator and q the observable value.

To find this wavefunction of physical systems and be able to say something about for example an electrons energy state, we need Schrodingers equation. The time-independent Schrodinger equation is shown in Eq. A.4:

$$-\frac{h^2}{8m\pi^2}\nabla^2\psi + V\psi = E\psi \tag{A.4}$$

where h is the particle momentum, m is the particle mass, V is the potential energy and E is the total energy of the particle. When the potential energy of a system is known, Eq. A.4 can be used to find the corresponding wavefunction.

A.3.2. Energy states

To calculate the energy states of electrons and their atomic orbitals, the Schrödinger equation is solved for an atom with only one electron, hydrogen-like atoms. This equation can be exactly solved, whereas atoms containing multiple electrons can only be approximated. When we assume that the nucleus behaves as a point charge with $+Ze$ charge, where $-e$ is the charge of an electron and Z is the amount of protons in the nucleus (the atoms atomic number), the potential energy of this system is shown in Eq. A.5 [113]:

$$V = -\frac{Ze^2}{e\pi\epsilon_0 r} \tag{A.5}$$

where ϵ_0 is the permittivity of free space and r is the separation between the electron and the nucleus. When we insert this potential energy into the Schrödinger equation, we find the energy in electron volts (eV) of the electron for the different states as shown in Eq. A.6 [113]:

$$E = -\frac{13.6Z^2}{n^2} \tag{A.6}$$

where n is the principal quantum number.

A.3.3. Quantum numbers

Because electron energies are quantized, its corresponding wavefunctions are as well. Because of this, each atomic arbital can be defined by a set of integers (quantum numbers). The principal quantum number is n, which describes the energy of the electron or in other words its shell. This number is always a positive integer. The second quantum number is l, which describes the orbital angular momentum of each electron or in other words its subshell. It can be considered to describe the shape of the subshell. The values of l range from 0 to $n-1$, however the integers are given letters instead of numbers. The letters for l: 1, 2, 3 and 4 are s, p, d and f respectively. The z-component of the orbital momentum is the quantum number m which ranges from $-l$ to l. This can be considered as the orientation of the subshell's shape. The fourth and last quantum number is the spin projection s, which describes the intrinsic angular momentum of the electron. This number is always $-1/2$ or $1/2$, spin down and spin up. Pauli's exclusion principle states that two electrons can not be in the same quantum state, meaning they can not have the same four quantum numbers. Therefore there can only be two electrons in any orbital, one with spin up and the other with spin down.

A.3.4. Atomic orbitals

The orbits of an atom can be very crudely considered as the locations of its electrons. These orbits can be divided into shells and subsequently into subshells (orbitals). The shells are equal to the energy levels of the eletron, the orbitals are the wavefunctions that are found with Schrödinger equation.

To see where the electrons can go inside the shells and corresponding subshells, an electron orbital diagram can be constructed (Fig. A.5). A few rules have to be followed though. The first is that the lowest energy orbitals are filled first, so $n = 1$ is first, which only has one subshell s. In the second shell $n = 2$, subshell s is filled first, then subshell p.

The second rule is the Pauli exclusion principle that was already mentioned. No two electrons can have the same four quantum numbers. The last rule is Hund's Rule [113] which states that orbitals of the same energy, having the same number n and l, are first filled with the highest amount of total spin. They are first filled with electrons that have spin up.
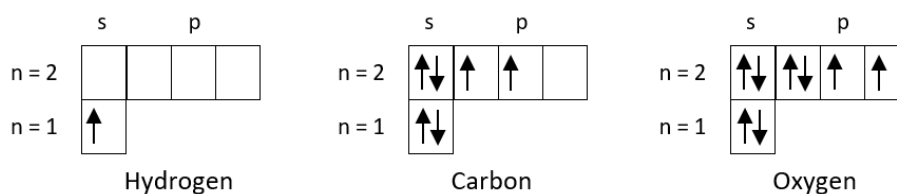
Figure A.5: Electron orbital diagram for hydrogen, carbon and oxygen.

To see what the orbitals actually look like, the Schrodinger equation is rewritten in polar coordinates (Eq. A.7) and then solved [113].

$$\psi_{n,l,m}(r,\theta,\phi) = R_{n,l}(r) Y_{l,m}(\theta,\phi) \tag{A.7}$$

where R is the radial wavefunction and Y the spherical harmonic. Y describes the orbitals of the electrons and they are visualized in Fig. A.6.

A.4. Molecular bonds and radical formation

With linear combinations of atomic orbitals, molecular orbitals can be constructed. When the atomic orbitals of two atoms overlap, in the region shared by these two atoms the electron density will be higher. The electrons of both atoms are shared with each other with the result that each atom now has a full shell. When this happens the total energy of the system decreases, which is why electron sharing is more favorable for atoms. The atoms have formed a covalent bond. The orientation of the atomic orbitals dictates the type of bond, most common being a σ bond (head-on overlap) and π bond (sideways overlap) (Fig. A.7). A double bond between two atoms consists of one σ bond and one π bond. When there is less electron density in the
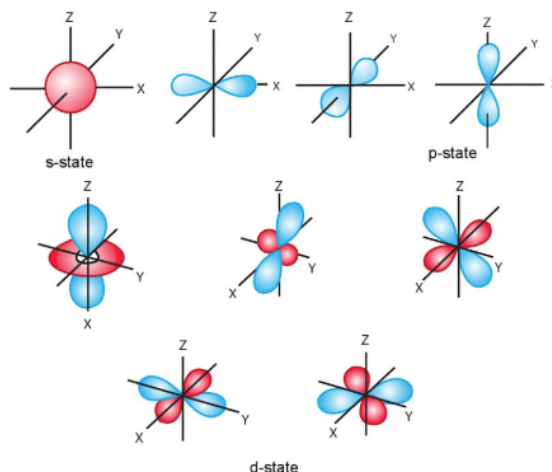
Figure A.6: The spherical harmonic functions for $l = 0$ (s) with $m = 0$; $l = 1$ (p) and $m = -1, 0, 1$; $l = 2$ (d) and $m = -2, -1, 0, 1, 2$, reproduced from [113].

region between two atoms they can also form anti-bonding orbitals, denoted with an asterisk (σ^*, π^*). However anti-bonding orbitals increase the energy of the system in comparison to the individual atoms and is therefore unstable.
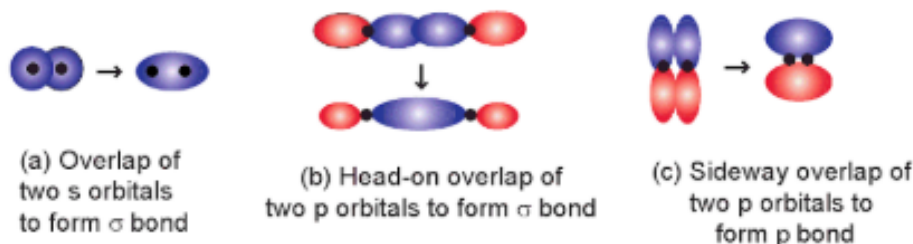
Figure A.7: Overlap of atomic orbitals that form σ and π bonds, reproduced from [113].

The energies that correspond to the bonding and antibonding orbitals increase like:

$$\sigma < \pi < n < \pi^* < \sigma^* \tag{A.8}$$

where n is in this case a pair of unbonded electrons [109]. As can be seen from Eq. A.8, the most energy is needed to transition from a σ bond to a σ^* bond. When there are pairs of unbonded n electrons, the transition from $n \to \pi^*$ takes the least amount of energy. The transition from $\pi \to \pi^*$ takes more energy, but when there are no unbonded n electrons in the molecule this is the most probable transition. The excitation to a π^* bond can also, through internal conversion, lead to a reversal of the electrons spin into an excited triplet state. This excited electron can not immediately go back to its ground state because this requires it to flip its spin yet again. Therefor the triplet state is relatively long (10^{-3} s) compared to the lifetime of a singlet state (10^{-8} s) [109]. Because in a triplet state the electron spin is in parallel to the ground state electron, it can not be in the same orbital anymore. This breaks the molecular bond as was seen in Fig. A.2.

Usually the molecules that are used in photochemistry contain π bonds and have no unbonded n electrons. In these molecules the electronic transitions are always $\pi \to \pi^*$. This causes these molecules to be more prone to break a molecular bond and create radicals. When a double covalent bond is broken into one single covalent bond and two unbonded electrons, it is that π bond that is lost.

Voxel Diameter - Mathematical Derivation

The mathematical derivation for Eq. 2.13.

$$\frac{\partial \varrho}{\partial t} = (\varrho_0 - \varrho)\, \sigma_2 I^2 \quad \text{with} \quad I = I_0 \cdot e^{\frac{-2 r_0^2}{\omega_0^2}}$$

$$\varrho(t) = C_1 \cdot e^{-I_0^2 \cdot e^{-4 \frac{r_0^2}{\omega_0^2}} \sigma_2 \cdot t} + \varrho_0 \qquad \boxed{\rightarrow \varrho(0) = 0 \Rightarrow C_1 = -\varrho_0}$$

$$\varrho - \varrho_0 = C_1 \cdot e^{-I_0^2 e^{-4 \frac{r_0^2}{\omega_0^2}} \sigma_2 \cdot t}$$

$$\ln\left(\frac{\varrho - \varrho_0}{C_1}\right) = -I_0^2 \sigma_2 t \, e^{-4 \frac{r_0^2}{\omega_0^2}}$$

$$\ln\left(\ln\left(\frac{\varrho - \varrho_0}{C_1}\right)\right) = \ln\left(-I_0^2 \sigma_2 t\right) - 4 \frac{r_0^2}{\omega_0^2}$$

$$4 \frac{r_0^2}{\omega_0^2} = \ln\left(\frac{-I_0^2 \sigma_2 t}{\ln\left(\frac{\varrho - \varrho_0}{C_1}\right)}\right)$$

$$4 \cdot r_0^2 = \omega_0^2 \ln\left(\frac{I_0^2 \sigma_2 t}{\ln\left(\frac{C_1}{\varrho - \varrho_0}\right)}\right)$$

$$2 \cdot r_0 = d = \omega_0 \left(\ln\left(\frac{I_0^2 \sigma_2 t}{\ln\left(\frac{C_1}{\varrho - \varrho_0}\right)}\right)\right)^{1/2} \quad \longleftarrow$$

$$d = \omega_0 \left(\ln\left(\frac{I_0^2 \sigma_2 t}{\ln\left(\frac{\varrho_0}{\varrho_0 - \varrho}\right)}\right)\right)^{1/2}$$

Critical Point Dryer

C.1. Introduction

When Scanning Electron Microscopy (SEM) came towards studying the surface morphology of biological samples an issue arose. When (air) drying a biological sample, it can cause damage to the biological structure. This is due to the surface tension at the liquid-air boundary during evaporation. Where the liquid is in contact with material, it pulls against the material. On the length scale of the samples that are to be studied, e.g. biological cells, this surface tension creates considerable forces. The surface tension of liquid to air can be lowered when using other liquids, e.g. acetone instead of water. Still this causes deformations in the air dried samples [105].

Critical point drying is a drying method that exploits a phenomenon first discovered by Dr. Andrews in 1863 [114]. Dr. Andrews found that when bringing carbon-dioxide to a particular temperature and pressure, no distinction between liquid and gas state could be made anymore. He named this point the critical point. On reaching this point, the meniscus between the liquid and gas is seen to flatten out and finally completely vanishes. The surface tension becomes zero and therefore delicate samples can be dried without damaging them.

C.2. The phenomenon

Figure C.1 shows the thermodynamic properties of an arbitrary substance (that contracts on freezing)[115]. Figure C.1a shows the p-v-T plot, whereas C.1b-c are the p-T and p-v projections [115].

The phenomenon we are interested in is called the 'continuity of state', which means that the density of the gas is exactly the same as the liquid. This can be seen in Figure C.1c. The dome shaped region is called the vapor dome and this includes the region where the substance is in a two-phase liquid-vapor state. When following an isothermal from the right side, increasing pressure causes it to go from a saturated vapor state into the vapor dome. The volume is decreasing at an almost constant pressure, and at the left side of the vapor dome the substance is in a saturated liquid state. The isothermal leaving the vapor dome on the left side at an almost vertical direction shows very nicely the incompressiblity of liquid as increasing pressure does not change the volume. When increasing the temperature, the difference in volume between saturated vapor and saturated liquid becomes smaller. At the top of the dome, there is no difference anymore between the two states, and this is called the critical point. This point has a corresponding critical temperature, critical pressure and a particular density. At this critical point the thermodynamic properties of the two states coincide. No distinction can be made between the liquid and vapor state and the surface tension reduces to zero.

Above the critical temperature the substance can not be transformed into liquid, no matter how much pressure is added. Therefor the substance is only called a gas when it is above its critical temperature. Below its critical temperature it is called a vapor, as adding pressure can result it to turn into liquid.

C.3. The procedure

All substances have a unique phase diagram, meaning that different substances have a different critical temperature and pressure. In Table C.1 these critical constants are given for some common substances. When water is used as a medium, the table shows that bringing it to its critical temperature, very high temperatures have to be reached. This can harm the delicate sample that has to be dried. However carbon-dioxide already
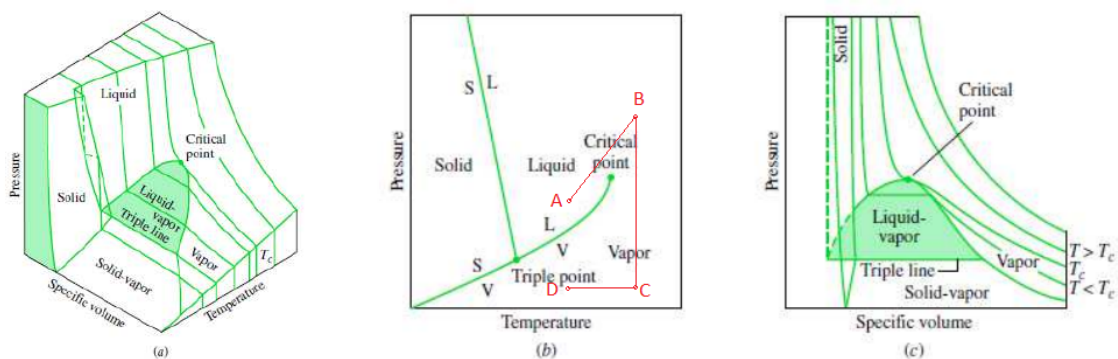
Figure C.1: p-v-T graphs for an arbitrary substance, a) three-dimensional view, b) phase-diagram, c) p-v diagram, reproduced from [115].

reaches its critical point at around 31 °C, which is really convenient and exactly the reason why in critical point drying, carbon-dioxide is used as a medium.

Table C.1: Critical constants, reproduced from [115].

Substance	T_C [°C]	P_C [bar]
Hydrogen	-239.95	13.0
Carbon-dioxide	30.85	73.9
Ethanol	242.85	63.8
Water	374.15	220.9

Usually the sample that has to be critically point dried is submerged in water. Because water is not miscible with carbon-dioxide, an exchange fluid has to be used like ethanol or acetone. When after some steps the sample is fully submerged in the exchange fluid, it in turn can be replaced by liquid carbon-dioxide. The critical point drying procedure can now be initiated.

Figure C.1b shows in red the path that is followed. Point A shows the starting point when the CO2 is in liquid phase. The temperature is increased and with this also the pressure increases. The critical point is reached and the temperature is now kept constant at somewhat above the critical temperature, point B. The pressure is slowly decreased by bleeding out CO2 gas, reaching point C. The temperature can now be decreased to its original value, point D. It can clearly be seen that by following this route the phase boundary line is not crossed, meaning that we circumvented the abrupt phase change from liquid to vapor.

The exact protocol for operation can be found in Appendix D.

Protocol for Emitech K850 Critical Point Dryer

Edited workflow from the Instruction Manual [116].

Author:
R.M.B. Pleeging.
Studentnr: 4216024.
Tel. +31 6 24963387

Last revision: January 3, 2019

D.1. Initial Operations Check

1. Turn on main power.

2. Ensure that the high-pressure **CO2 cylinder valve is closed**. Check that all valves can be opened and closed freely. **Close inlet valve** and **open exhaust valve**. The pressure gauge should read zero. Remove chamber lid by unscrewing the three thumbnuts.

3. Refit the chamber lid, ensuring the 'O' ring is not damaged and is correctly seated. Tighten thumbnuts firmly in **even rotational sequence**.

4. **Switch on heater**. The heater control should illuminate, and the temperature will increase gradually. **Switch off heater** when indications are that it is operating.

5. **Close all valves**, and **open CO2 cylinder valve**. Check for any obvious signs of leaks.

6. **Open cool valve** by a very small amount until a steady hissing of gas is established. The temperature will decrease gradually. **Close cool valve** when indications are that it is operating.

7. **Open inlet valve**. The pressure gauge should read approximately 800psi. **Close inlet valve**, and depressurize the chamber firstly by using the bleed valve and then by using the exhaust valve for quick depressurizing. This will also ensure that the system has been 'flushed through'. **Close the bleed valve** and **the exhaust valve**.

   TEST RUN

8. **Open cool valve** slowly to establish a steady flow.

9. The chamber, after an initial thermal delay, should cool down to +5 °C in approximately 3 minutes. At +5 °C **close cool valve** and the temperature will 'coast' down to approx. +2 °C. By **delicate handling** freezing of the valve can be avoided.

10. **Open inlet valve** slowly, taking approximately 1 minute to fill the chamber to the correct level by observing the meniscus in the viewing window. On filling, the temperature may increase to +5 °C. If it gets any warmer, and any difficulty is experienced with filling, then a small amount of cooling can be applied. The chamber should be filled to the center of the viewing window to filling mark shown. It is **IMPORTANT** to not over fill the chamber, but if the chamber is filled with to little CO2 the critical pressure will not be reached. The key is: enough but not too much.

11. **Close inlet valve** and **switch on heater**. For safety **close CO2 cylinder valve**.

12. After an initial delay the temperature will increase to the control temperature of +35°C, this takes approximately 35 minutes. At this point it will control switching in and out over the range 32 °C to 38 °C and pressure in the range of 1200 to 1300 psi. If the meniscus is observed, it will fall slightly to the lower fill level of the viewing window.

13. At a temperature of approximately 30 °C, and a corresponding pressure of 1100 psi the meniscus will disappear having reached the Critical Point.

14. The system can now be depressurized whilst maintaining the temperature. The **bleed valve** is used for depressurization. The **fine bleed valve** should be closed initially, showing '6.5-7' at the top of the valve (Figure D.1a). The **bleed valve** can now be opened without any gas leaving. For **less delicate specimens** the fine bleed can now be opened, by turning the valve counterclockwise from '7' to '2', resulting in a rate of approximately 100 psi/minute, taking approximately 13 minutes. When the pressure decreases also the bleed rate goes down, and the bleed valve should be adjusted to maintain the rate.

15. For **more delicate specimens** the **fine bleed** should be turned from the closed setting '7' to '1' (Figures D.1a-c), resulting in a rate of approximately 100 psi/2 minute, taking approximately 26 minutes. Also here the pressure decreases as the bleed rate goes down, and the bleed valve should be adjusted to maintain the rate.

16. **Switch off heater**.

17. To shut down the instrument, **close CO2 cylinder valve**. **Open cool and exhaust valves** to ensure depressurization of the lines and the chamber. Make sure the **fine bleed valve** is set back to its closed setting (Figure D.1a).

18. **Switch off main power**.

a)   b)   c)
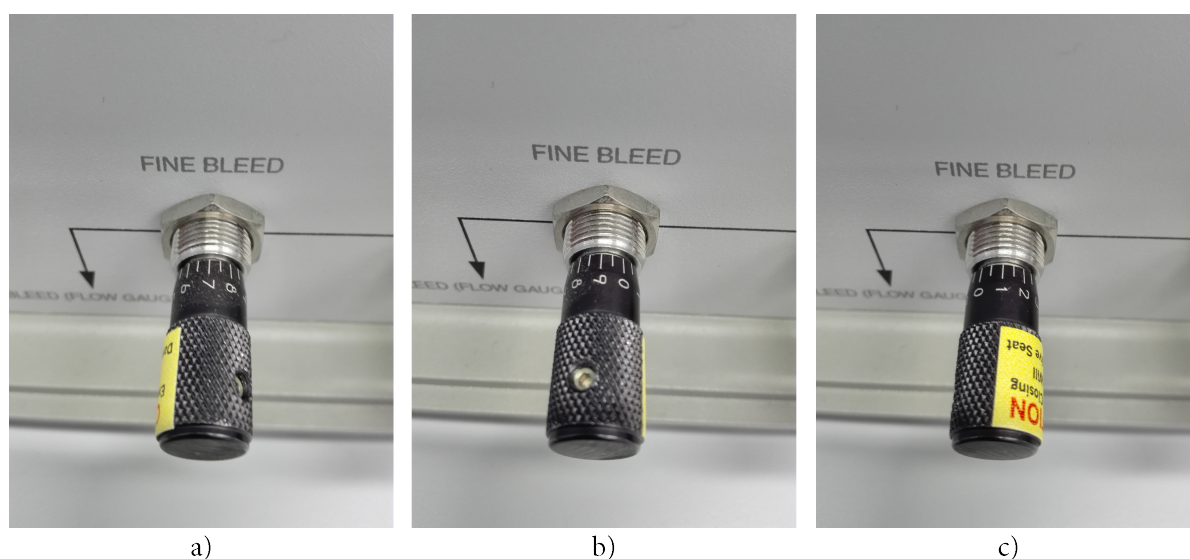
Figure D.1: Fine bleed valve settings, turned counterclockwise to open valve. a) closed valve setting '7', b) intermediate setting '9' for 33 psi/min, c) fine bleed setting '1' for 50 psi/min.

D.2. Critical Point Drying

1. Ensure **all valves are closed**.

2. **Open cool valve** slowly to establish a steady flow. Pre cool the chamber to +5°C and **close cool valve**.

3. **Remove chamber lid** by unscrewing the three thumbnuts. Fill the chamber to the half with the same fluid as your sample is in (ethanol, acetone or IPA).

4. **Load sample holder** with sample, avoiding any unnecessary delay. Make sure the sample is fully covered with fluid to avoid any air drying of the sample.

5. **Refit chamber lid**, ensuring the 'O' ring is not damaged and is correctly seated. Tighten thumbnuts firmly in **even rotational sequence**.

6. **Open inlet valve** and the CO2 level is filled to the top of sight glass.

7. Allow the sample to **soak** for approximately 5 minutes (for very large specimens the soak period should be double). Soaking the sample is very important, **do not skip this step**.

8. The chamber should now be **purged** for approximately 1 minute. To do this, **slowly open the exhaust valve**, observe the meniscus to fall slightly. **Open inlet valve slightly** to compensate and balance the system thereby replenishing the chamber with 'fresh' CO2. As the exchange fluid is denser it will go to the bottom of the chamber which is designed to be top filling bottom draining.

9. Ensure the meniscus is at the center of the viewing window. Repeat the soak as in (7-8).

10. A **further purging** should now be carried out as in (6-8). During the second purging of 1 minute, a check can be made to see that solvent exchange has been achieved: Remove the plastic pipe from the exhaust outlet. Using a soft cloth and place into the stream of gas. The presence of a small damp patch will indicate if solvent is present. If necessary, repeat a soak and purge step. It is very important to remove all liquid, as only a little can ruin your sample. When the solvent seems to be fully exchanged, repeat one soak and purge step to be sure.

11. Ensuring meniscus is at the top of the upper red line. When the chamber is not filled enough, the critical pressure can not be reached. **Close all valves**. For added safety also **close CO2 cylinder valve**.

12. **Switch on heater** and allow stable conditions to be reached of approximately 35 °C and 1250 psi in about 35 minutes. At this point it will control switching in and out over the range 32°C to 38°C and pressure in the range of 1200 to 1300 psi. The meniscus is observed during the heating phase, it may initially rise out of view of the window and then come back into view fall to the lower level of the viewing window (this depends on the ratio of liquid to air space in the chamber). At a temperature of approximately 30 °C, and a corresponding pressure of 1,100 psi the meniscus will disappear having reached the **Critical Point**.

13. The system can now be depressurized whilst maintaining the temperature. The **bleed valve** is used for depressurization. The **fine bleed valve** should be closed initially, showing '6.5-7' at the top of the valve (Figure D.1a). The **bleed valve** can now be opened without any gas leaving. For **less delicate specimens** the fine bleed can now be opened, by turning the valve counterclockwise from '7' to '2', resulting in a rate of approximately 100 psi/minute, taking approximately 13 minutes. When the pressure decreases also the bleed rate goes down, and the bleed valve should be adjusted to maintain the rate.

14. For **more delicate specimens** the **fine bleed** should be turned from the closed setting '7' to '1' (Figures D.1a-c), resulting in a rate of approximately 100 psi/2 minute, taking approximately 26 minutes. Also here the pressure decreases as the bleed rate goes down, and the bleed valve should be adjusted to maintain the rate.

15. **Switch off heater**.

16. **Open chamber lid** and **remove specimen**. In all cases, subsequent treatment should be maintained in dry conditions. **Close chamber lid**.

17. To shut down the instrument, **close CO2 cylinder valve**. **Open cool and exhaust valves** to ensure de-pressurization of the lines and the chamber. Make sure the **fine bleed valve** is set back to its closed setting (Figure D.1a).

18. **Switch off main power**.
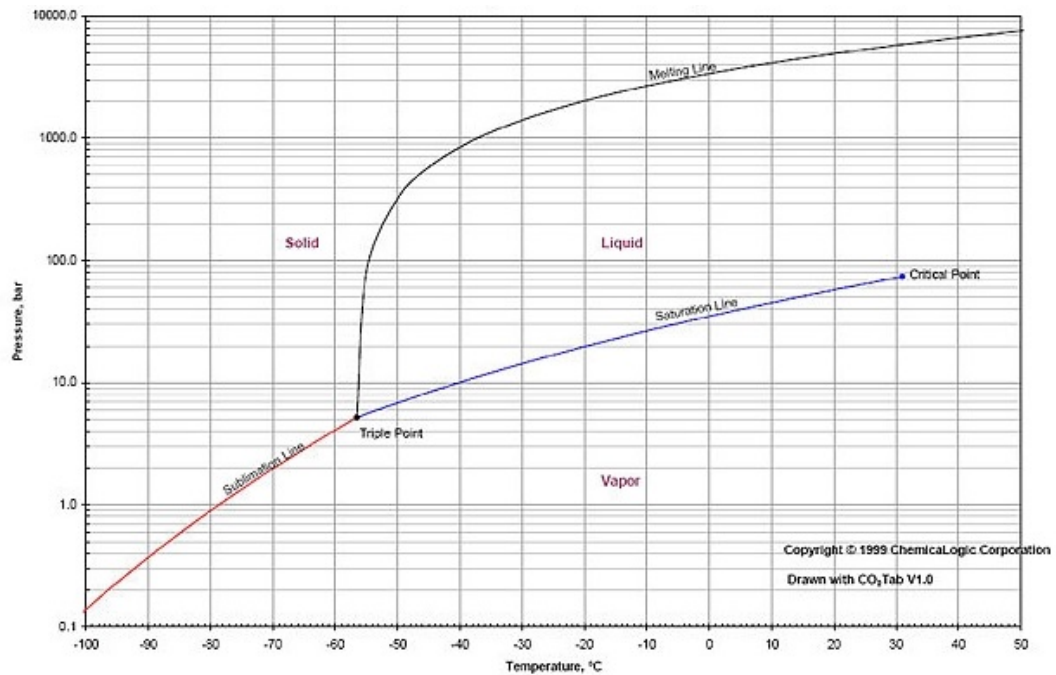
Figure D.2: p-T diagram for CO2, reproduced from [117].
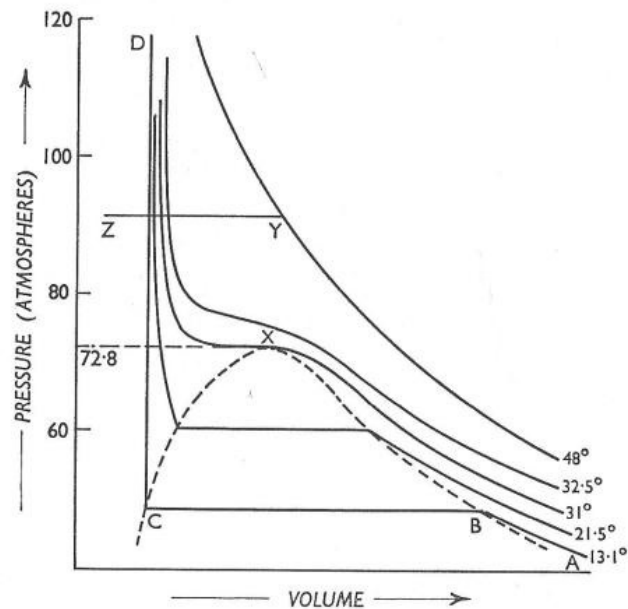
Figure D.3: p-v diagram for CO2, reproduced from [118].

References:
[117]: [online] Appendix A-1: CO2 thermodynamics | Global CCS Institute.
[118] : [online] The Liquefaction of Gases – Part II | carnotcycle.

Other microfluidic chip designs

In the previous work that we used as a starting point (by Laffifte et al. [48]), a microchannel was used in which two precursor solutions were brought in at separate inlets and mixed via diffusion at the liquid-interface in between the two laminar flows. The fluids are continuously pumped through the microchannel and therefore we called this the 'continuous approach'. There is also specialized equipment that measures the turbidity of a solution that is continuously mixed in a glass vial, in order to derive crystallization characteristics like nucleation rates. Although the solution in the vial is mixed, it remains within the vial and therefore we called it the 'batch approach'.

The microfluidic chip was composed of a polydimethylsiloxane (PDMS) microfluidic component and a glass cover slip to create a closed channel in between the PDMS and glass. The glass cover slip contained the structures written with 2PP, which are encapsulated by the microchannel walls. The microfluidic component was made using a 3D printed mold and PDMS soft lithography. The mold contained the negative version of the microchannels. During this research several microfluidic chip designs have been tried and tested, for both the continuous and batch approach. Eventually a more basic design was proposed, very similar to that of the previous work, but that enabled us to perform multiple parallel tests on a single chip. In this appendix the different designs that were produced and tested are discussed.

E.1. Continuous approach

E.1.1. Single-experiment

First it was tried to reproduce the work from Laffite et al. by producing a chip with one channel containing two inlets and one outlet. The design of the first mold (Fig. E.1a) was rather large and could be fitted on a glass microscope slide. The chip was however to be assembled with a glass cover slip that is used in the Photonic Professional Gt (Nanoscibe GmbH). These cover slips were 30 mm in diameter, therefore a smaller mold design was made (Fig. E.1b). Both of these design were tested with a preliminary setup and could be used to reproduce the work by Laffite et al.

(a)   (b)
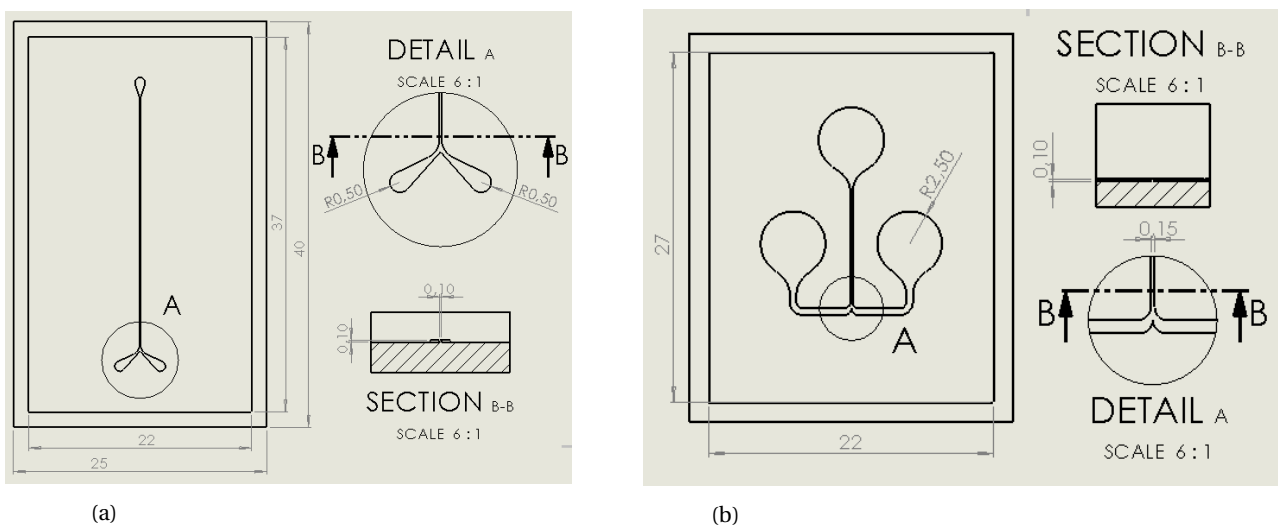
Figure E.1: Drawings of a) the first design and b) the second design that was made smaller to fit on a glass cover slip of 30 mm diameter.

E.1.2. Multi-experiment

To find the relation between different kidney surface morphologies and crystallization, the structures written with two-photon polymerization (2PP) were incorporated in the microchannel. The chip designs as in Fig. E.1 are single-experiment designs, i.e. each chip could only be used for one experiment. The process of writing the structures on the cover slip using 2PP and afterwards dry them in the critical point dryer is time consuming and only one cover slip at a time can be processed. Therefore new designs were tried able to perform multiple experiments on a single chip.

One difficulty with a multi-experiment chip with the continuous approach is that the two precursor solution need to be introduced to each other only in the microchannel. If they are mixed before entering the chip, crystallization occurs prematurely and the exact nucleation times can not be derived. Therefore intricate designs are needed for a chip with multiple channels. In Fig. E.2a the design for a multichannel chip is presented. This design contains four separate channels, each having a junction at the bottom where two precursor solutions can be introduced. Because the solutions can only be mixed in the channel, they need to be separated before entering each junction. This means that for this particular chip with four channels, one of the precursor solution (here the calcium solution) needs to have two separate inlets. The requirement of 'no mixing outside of the channel' bids us to use multiple inlets. With a number of channels n, the number of inlets i that are required follows:

$$i = \frac{n}{2} + 1 \quad \text{for n: even number of channels}$$

$$i = \frac{n+3}{2} \quad \text{for n: odd number of channels}$$

Another design was to use only one inlet for each precursor solution, but still multiple mixing regions are needed for multiple experiments. Each mixing region needs however a separate outlet for the fluid to flow out. This design is presented in Fig. E.2b. Because of the two-dimensional nature of the microfluidic chips, there always remains a choice to be made: having multiple inlets or multiple outlets.

Both designs were tested with two solutions having different colors, clear demi-water and demi-water with blue food coloring, to see if the different solutions did in fact only mix at the designated areas (indicated with the red boxes in Fig. E.2). Multiple chips were prepared with these designs. None of them worked properly. This was probably because the surface of the 3D printed mold, which is replicated in the PDMS after soft lithography, is not perfectly smooth. The chips are designed to be symmetrical, but due to the surfaces not being smooth the fluid does experience different resistance per channel. One path is preferred over another and the fluids do not follow the channels as predicted. This means that the precursors flow through the whole chip, causing them to mix not only at the designated regions but everywhere in the chip.

Because of the surface unevenness of the molds, caused by the 3D printing procedure, the PDMS microfluidic component are also not completely smooth. With a single experiment in one channel at a time it was proven to work, but performing multiple experiments in one chip at the same time was not achieved. Though it was still needed to perform multiple experiments on one chip. Therefore the design of the single microchannel with two inlets and one outlet was used and placed so that multiple channels fitted in one chip. This is presented in Fig. E.3 , also showing the relative size of the glass cover slip and the structures that would be written on it. Four nanopillar arrays could be written on the coverslip and placed inside four microchannels. With that chip we could do eight crystallization experiments, four with structures and four without.

E.2. Batch approach

E.2.1. Single-experiment

The conventional way of obtaining crystallization characteristics, like solubility curves and nucleation rates, is by using machines like Crystalline or Crystal16 (Technobis). A glass vial with a certain solution is inserted in such a machine, after which they detect the number and size of crystals that are being formed. Crystal16 can contain 16 vials at once and measures the turbidity by by monitoring the transmissivity of a red laser that is shown through the vial [119] (see Fig. E.4). Crystalline can hold up to 8 vials and also contains a particle viewer (camera) and real time Raman capabilities [120]. To measure the induction time of a solution when different surface morphologies are introduced, a small sample containing these morphologies is placed in
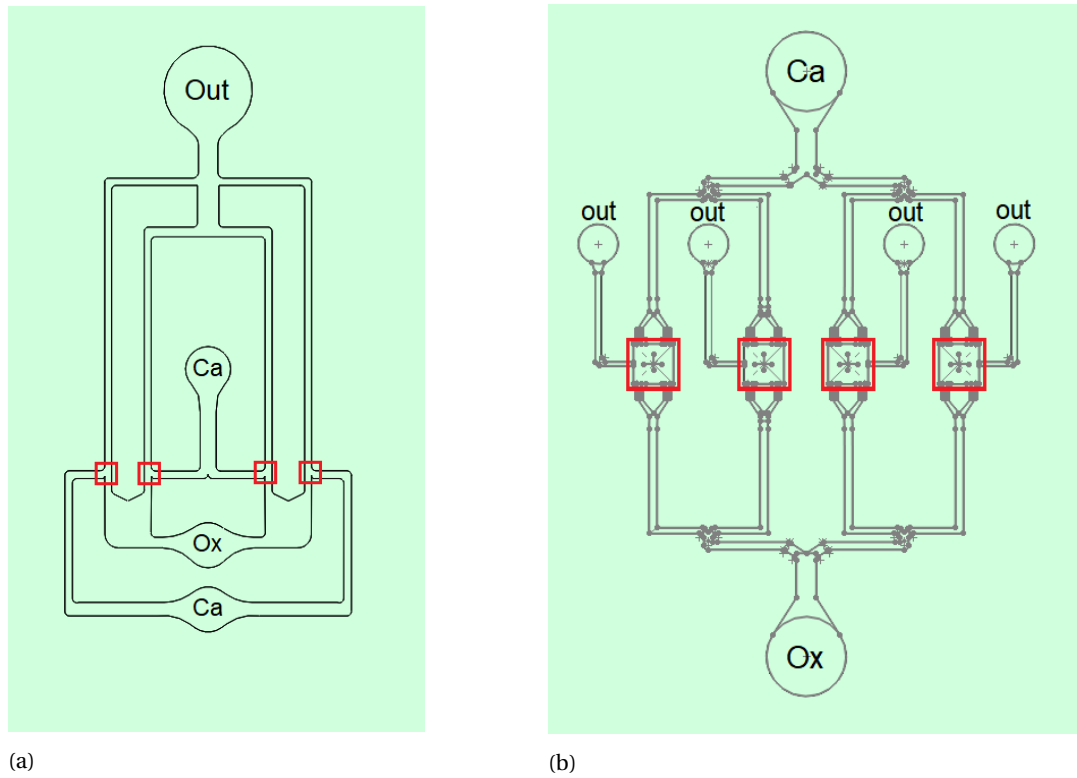
Figure E.2: Snapshots of the 3D CAD designs for a) the multichannel chip and b) the 'mixer'-chip. The red boxes indicate were the two precursors solutions should come into contact, a) at the junction of the microchannels and b) at the 'mixing' region in the middle.
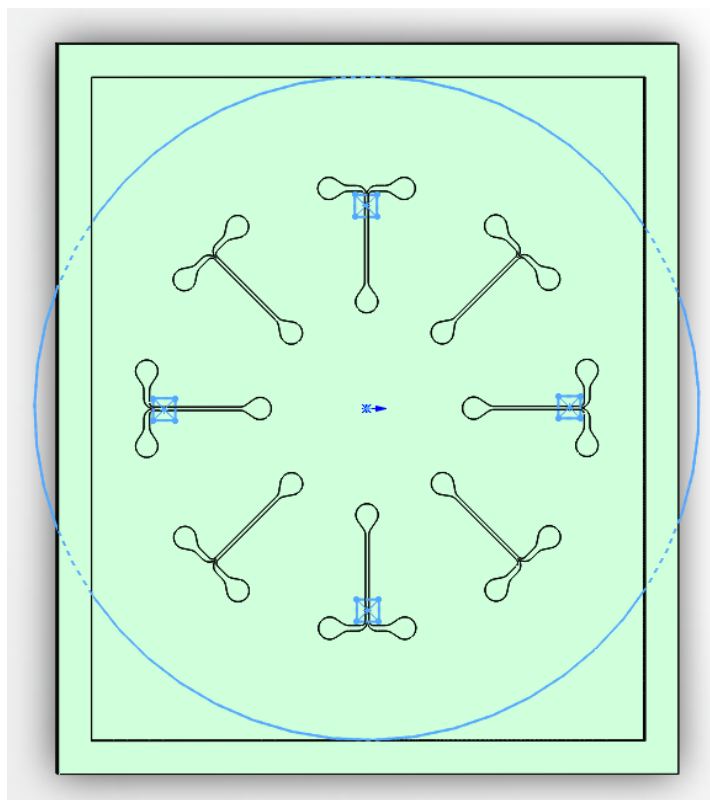
Figure E.3: The design for the final microfluidic chip containing eight separate microchannels, each with two inlets and one outlet. The blue circle represents the glass cover slip on which four nanopillar arrays are printed. These arrays are aligned and placed so that they lie in the microchannels.

the vial and placed inside the machine. This means that for each experiment (one per vial) a sample has to be prepared. Because of the stochastic nature of crystallization, this means that a lot of samples will be needed. Therefore we tried to use this idea and to scale it up.

Figure E.4: Measuring turbdity in a glass vial by measuring the transmissivity of a red laser [119].

E.2.2. Multi-experiment

A PDMS component was made that contains multiple pockets, instead of using individual vials for experiments. This PDMS component we could then combine with the glass cover slip that contained the different morphologies, creating a chip with multiple individual pockets. The design idea is schematically presented in Fig. E.5. The idea was to have the multiple pockets acting as individual vials and use a microscope to observe for the formation of particles. The design was tested with a PDMS component with nine pockets and a glass cover slip containing two nanopillar arrays, both shown in Fig. E.6. This design posed however the following problem. The pockets need to be filled with the two precursor solutions and immediately the glass cover slip with structures should be placed on top of it. The two solutions are thus already mixed before the pockets can be observed with the microscope. Also we are not able to observe multiple pockets simultaneously, so a process had to be designed that enabled observing the pockets in series instead of parallel.

PDMS with pockets   Glass cover slip with 2PP structures   Aligned 'chip'
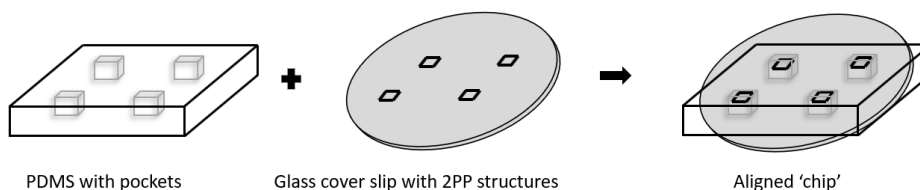
Figure E.5: Design of the 'chip' that contains multiple individual pockets.

A PDMS component was therefore made that contained pockets going all the way through the PDMS. It resembles a screen with multiple holes and PDMS walls in between. This way we could first align the PDMS pockets with the structures and afterwards fill those pockets with the solutions, one by one. The aligned PDMS pocket with a nanopillar array is shown in Fig. E.7. With an optical microscope we could then observe the nanopillar array that was submerged in the precursor solutions and we did see crystals forming. The microscope was focused at the nanopillars on the glass cover slip at the bottom of the pockets. Tiny crystals appeared the focus, their movements strongly resembling Brownian motion, and they settled on the bottom. The crystallization could be observed and captured in real time.

After discussing these results with the crystallization group at the Process & Energy department a flaw in these designs was noticed. In the conventional equipment that uses the glass vials, the precursor solutions are continuously mixed with a build-in mixer. This is a requisite for the crystallization. In our designs the solutions remain static within the pockets and do not get mixed. The first solution is pipetted in the pocket and then the other on top. This creates a liquid interface at which the crystals probably nucleate. They

then sediment to the bottom, something that was also observed in our experiment. Therefore these designs were not usable and the continuous approach was used, as the proof of principle for that design was already accomplished.
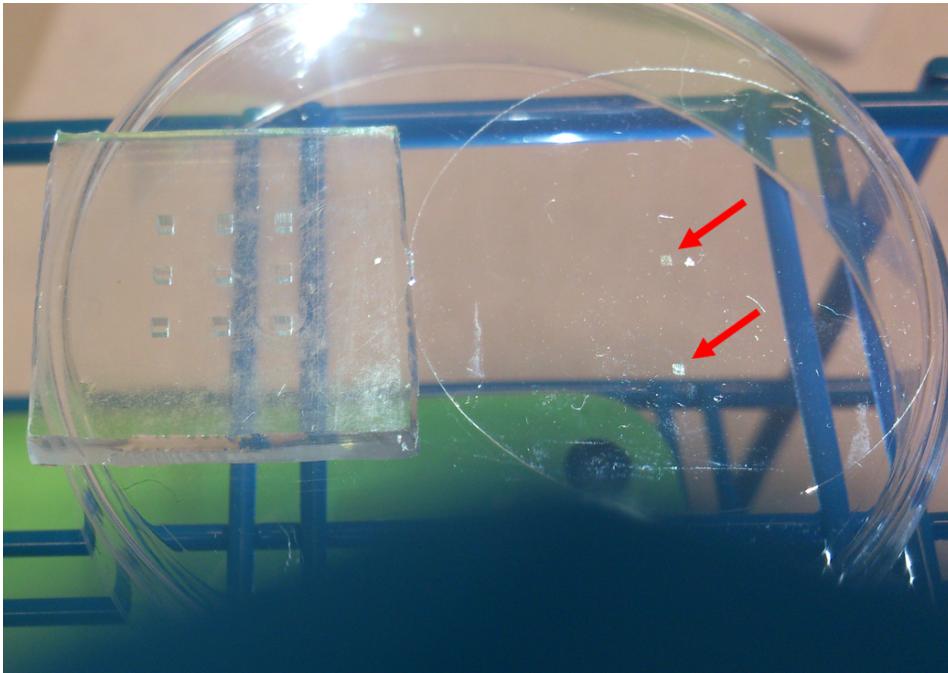
Figure E.6: PDMS component with nine 1 x 1 mm pockets and a glass cover slip with two 600 x 600 μm nanopillar arrays (pointed at with the red arrows).
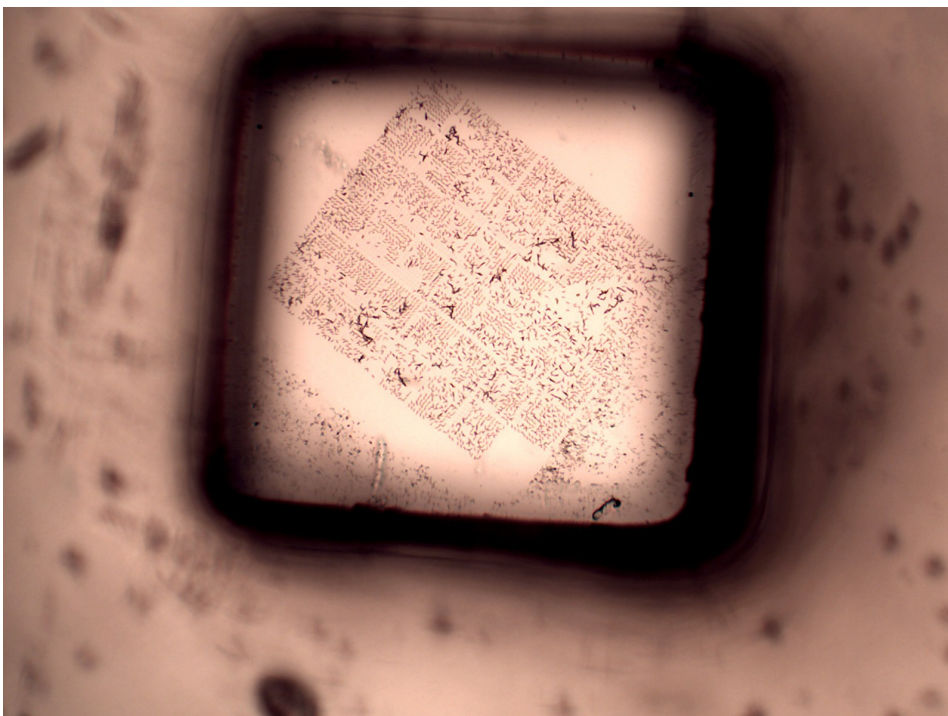
Figure E.7: One of the pockets aligned with a nanopillar array. Pillars were not dried in the critical point dryer for this test and were therefore all collapsed.

Iterations of print jobs for nanopillar arrays

This appendix contains the logbook that was written up during the different iterations made during the optimization of writing and design parameters. It is solely meant to show the design choices that were made during optimization. The data from these iterations was used in the main matter of the report. These iterations only show the path towards our results and is therefore placed in the appendix as a standalone chapter.

F.1. Data analysis: Iteration 0

Diameter100 - Height2500 - S0.1 - H0.02 - LP10-30 - SS1000-9000 - 4x4

A system is made to conveniently name all data. Letters A - Z are used for the scanning speeds used. A is used for a scanning speed (SS) of 1000 and it increases per letter by 2000. Numbers 1-9 are used for the laser power (LP) used. 1 is used for the lowest laser power and it increases per number by 5. As an example, B3 means print parameters LP20 and SS3000, D6 means LP35 and SS7000.

F.1.1. Design and print parameters

Pillar diameter: 250 nm
Pillar height: $1000 - 1500 - 2000 - 2500$ nm (AR $4 - 6 - 8 - 10$)
Slicing: 0.1 μm
Hatching: 0.02 μm
Laser power: $10 - 15 - 20 - 25 - 30 - 35 - 40$
Scanning speed: $1000 - 3000 - 5000 - 7000 - 9000$
Array size: 4 x 4 pillars with 1 μm spacing

F.1.2. Design choices

1. Make the pillar diameter in the design the same as the actual diameter. Find the printing parameters that match the design.

2. Not sure how high we can print pillars, so build them up step by step.

3. Based the laser power range, slicing and hatching on previous work of Abhishek.

4. Make multiple pillars, 16 in this array, to be able to do more measurements with one print job, i.e. more data.

F.1.3. Observations

Trend 1: Laser power versus diameter:
With increasing LP the diameter increases.

Trend 2: Aspect ratio (AR) versus diameter:
Largest difference can be seen between AR 4 and the rest. AR 6, AR 8 and AR 10 have almost the same diameters.

Trend 3: Scanning speed versus diameter:
With increasing SS from 1000 to 7000, the diameter decreases. For SS 9000 this is only seen for AR 4. The other

AR's are almost the same as for SS 7000.

The biggest effect of the different aspect ratios can be seen in the usable range of parameters. The higher AR can collapse (for too low LP) or burn (for too high LP), where the lower AR do not.

Scanning Speed	Usable range LP
1000	15-30
3000	20-35
5000	20-40
7000	25-40
9000	25-40

When looked at the sample with tilted view, it could be seen that the AR4 pillars were actually no pillars at all, but looked more like tiny blebs. Also it could be seen that some rows or columns in the printed array have consistently a weird (not round) shape. They are always the same pillars in each array.

	Scanning Speed 1000			Scanning Speed 3000			Scanning Speed 5000			Scanning Speed 7000			Scanning Speed 9000	
	4	**6**		**4**	**6**		**4**	**6**		**4**	**6**		**4**	**6**
A1: LP 10	(yellow)	(yellow)	B1: LP 10	(yellow)	(yellow)	C1: LP 10	(yellow)	(yellow)	D1: LP 10	(yellow)	(yellow)	E1: LP 10	(yellow)	(yellow)
	8	**10**		**8**	**10**		**8**	**10**		**8**	**10**		**8**	**10**
	(yellow)	(yellow)		(yellow)	(yellow)		(yellow)	(yellow)		(yellow)	(yellow)		(yellow)	(yellow)
	4	**6**		**4**	**6**		**4**	**6**		**4**	**6**		**4**	**6**
A2: LP 15	0.47151	0.5542	B2: LP 15	0.47242	0.5404	C2: LP 15	(yellow)	(yellow)	D2: LP 15	(yellow)	(yellow)	E2: LP 15	(yellow)	(yellow)
	8	**10**		**8**	**10**		**8**	**10**		**8**	**10**		**8**	**10**
	0.56263	0.5849		(orange)	(orange)		(yellow)	(yellow)		(yellow)	(yellow)		(yellow)	(yellow)
	4	**6**		**4**	**6**		**4**	**6**		**4**	**6**		**4**	**6**
A3: LP 20	0.70728	0.7718	B3: LP 20	0.65599	0.70643	C3: LP 20	0.50546	0.59191	D3: LP 20	0.39501	0.51014	E3: LP 20	(yellow)	(orange)
	8	**10**		**8**	**10**		**8**	**10**		**8**	**10**		**8**	**10**
	0.75529	0.7732		0.69201	0.71016		0.59227	0.61282		(orange)	(orange)		(orange)	(orange)
	4	**6**		**4**	**6**		**4**	**6**		**4**	**6**		**4**	**6**
A4: LP 25	0.78918	0.8245	B4: LP 25	0.72036	0.77294	C4: LP 25	0.61554	0.69782	D4: LP 25	0.5815	0.6184	E4: LP 25	0.57385	0.63608
	8	**10**		**8**	**10**		**8**	**10**		**8**	**10**		**8**	**10**
	0.80771	0.8103		0.76784	0.77283		0.69065	0.6978		0.62621	0.62796		0.62652	0.63793
	4	**6**		**4**	**6**		**4**	**6**		**4**	**6**		**4**	**6**
A5: LP 30	0.78201	0.8383	B5: LP 30	0.77879	0.83904	C5: LP 30	0.73638	0.78304	D5: LP 30	0.72267	0.75699	E5: LP 30	0.69061	0.74255
	8	**10**		**8**	**10**		**8**	**10**		**8**	**10**		**8**	**10**
	0.85987	0.8449		0.82081	0.84212		0.78123	0.78917		0.73452	0.733		0.72194	0.72137
	4	**6**		**4**	**6**		**4**	**6**		**4**	**6**		**4**	**6**
A6: LP 35	(red)	(red)	B6: LP 35	0.82029	0.87443	C6: LP 35	0.77591	0.83716	D6: LP 35	0.76101	0.81759	E6: LP 35	0.73522	0.81072
	8	**10**		**8**	**10**		**8**	**10**		**8**	**10**		**8**	**10**
	(red)	(red)		0.86364	0.87965		0.84067	0.85682		0.80188	0.79994		0.79401	0.79703
	4	**6**		**4**	**6**		**4**	**6**		**4**	**6**		**4**	**6**
A7: LP 40	0.89184	(red)	B7: LP 40	0.86856	0.91046	C7: LP 40	0.82115	0.87267	D7: LP 40	0.83411	0.86501	E7: LP 40	0.82495	0.86862
	8	**10**		**8**	**10**		**8**	**10**		**8**	**10**		**8**	**10**
	(red)	(red)		0.8902	(red)		0.87553	0.88898		0.84666	0.84882		0.84874	0.84768

Figure F.1: Dimensions

F.1.4. Discussion

The measurements were done on top view SEM micrographs of each set of parameters. Each micrograph contained the arrays of the 4 AR's for a particular LP and SS. Image analysis software Fiji was used. A macro was written to automatically measure the area of the pillar and copy these results. In excel these areas were converted to diameters. Fiji automatically labels its data, but each SEM micrograph was slightly different causing the data to each time have different labels. For each image I had to personally check which data labels belonged to which AR.

The trends that can be seen were also expected ones. For higher LP there is more energy locally in the resin, polymerizing more material. This causes the diameter to increase. It is also seen that for higher SS the diameter decreases, which follows from the same logic.

In the tilted view we could see that the AR 4 pillars were just tiny blebs, which do not resemble pillars by far.

Also because the shape we want to get in the end is a very high AR pillar, only the measurements for AR 10 are actually interesting.

The measured diameters were much larger than expected. To lower the actual diameters the design diameter can be made smaller or the hatching can be increased. When a bigger hatching distance is used, the laser beam will stay for a shorter amount of time in the particular area which leads possibly to less material to be polymerized. The same logic applies for a smaller design diameter.

It could be seen that always the same row or column of pillars had a weird shape. It could be tried to make bigger arrays, or the spacing between the pillars could be changed. I cannot really find a logical answer to this.

Later I found that this way of measuring pillars is not really accurate. However because it was exactly the same way for this whole job, the trends that could be seen are still usable. Therefor this data and the observed trends are still used for the next iteration.

F.2. Data analysis: Iteration 1
Diameter100 - Height2500 - S0.1 - H0.02 - LP15-30 - SS1000-9000 - 4x4

F.2.1. Design and print parameters
Pillar diameter: 100 nm
Pillar height: 2500 nm
Slicing: 0.1 μm
Hatching: 0.02 μm
Laser Power: 15 – 20 – 25 – 30
Scanning Speed: 1000 – 3000 – 5000 – 7000 – 9000
Array size: 4 x 4 pillars with 8 μm spacing

F.2.2. Design choices
1. Made the design diameter 2.5x smaller (250 nm to 100 nm). Try to see if the actual diameter also gets smaller.

2. Increased the spacing of the pillars to the actual spacing of 8 μm. In the previous job, the pillars in some rows or columns had consistently a weird shape. Hopefully with a bigger spacing this will not happen anymore.

3. Only tried for LP 15 - LP 30, because it seemed that for LP 10 nothing got printed, and above LP 30 the pillars were very large and even burned for low SS.

F.2.3. Observations
Printed the job 3x. The second job got very incoherent results based on the burning of the pillars. Sometimes it burned for LP 15, but not for LP 20 or LP 25. The dimensions are therefore only measured for the first and third print job. The percentages of collapsed and burned pillars are used from all 3 print jobs.

Trend 1: Laser Power versus diameter/height:
With increasing LP the diameter and height also increase.

Trend 2: Laser Power versus percentage collapsed:
The only collapse occurred at LP 15.

Trend 3: Laser Power versus percentage burned:
No trend is spotted, it looks random.

Trend 4: Scanning Speed versus diameter/height:
Only for LP 20 and LP 25, we see a decrease in diameter for increasing SS.

Trend 5: Scanning Speed versus percentage collapse:
No trend is spotted, it looks random.

Trend 6: Scanning Speed versus percentage burn:
No trend is spotted, it looks random.

SS 1000			SS 3000			SS 5000			SS 7000			SS 9000		
A1: LP 15	Dm/Di	hm/hi	B1: LP 15	Dm/Di	hm/hi	C1: LP 15	Dm/Di	hm/hi	D1: LP 15	Dm/Di	hm/hi	E1: LP 15	Dm/Di	hm/hi
	3.057	0.907		2.760	0.965		2.823	0.905		2.763	0.952		2.838	0.976
A2: LP 20	Dm/Di	hm/hi	B2: LP 20	Dm/Di	hm/hi	C2: LP 20	Dm/Di	hm/hi	D2: LP 20	Dm/Di	hm/hi	E2: LP 20	Dm/Di	hm/hi
	4.156	1.044		3.803	1.054		3.617	1.070		3.533	1.085		3.513	1.026
A3: LP 25	Dm/Di	hm/hi	B3: LP 25	Dm/Di	hm/hi	C3: LP 25	Dm/Di	hm/hi	D3: LP 25	Dm/Di	hm/hi	E3: LP 25	Dm/Di	hm/hi
	4.877	1.118		4.343	1.096		4.292	1.130		4.282	1.125		4.176	1.078
A4: LP 30	Dm/Di	hm/hi	B4: LP 30	Dm/Di	hm/hi	C4: LP 30	Dm/Di	hm/hi	D4: LP 30	Dm/Di	hm/hi	E4: LP 30	Dm/Di	hm/hi
	5.221	1.136		4.798	1.214		4.746	1.212		4.872	1.207		4.911	1.181

Figure F.2: Dimensions.

Figure F.3: Amount of collapsed and burned pillars.

F.2.4. Discussion

The weird pillars in some rows or columns did not seem to happen anymore, like it did in the previous job. Also the diameter is smaller, but most of them are still bigger than 250 nm.

There is clearly some randomness regarding the burning of the pillars in relation to the LP. This is also found in literature [98]. It could be caused by multiple factors:

- Dirt on the glass on which is printed. The dirt could absorb energy (heat) when the laser hits it. This in turn makes the dirt become too hot and eventually burn, causing the surrounding resin to also burn.

- The laser has power fluctuations. Because of these fluctuations in power, the expected values can vary, which causes the seemingly random character. However the findings are very random and diverse, so this does not look like the case. This means that the fluctuations should be very large, which is not to be expected.

- The resin contains monomers and photoinitiator in solution. The resin is not the newest and the bottle has been opened multiple times already. Some solvent has possibly already been evaporated, making the resin more concentrated and possibly less homogeneously distributed.

To mitigate this randomness, the glass substrate is to be cleaned very carefully and multiple times. This is to ensure that it is absolutely free of dirt or dust particles. If the random burning still occurs, it could be tried to use a brand new resin.

The height still seems to be alright, so for the next iteration a bigger height can be tried.

F.3. Data analysis: Iteration 2
Diameter100 - Height5000 - S0.1 - H0.02 - LP15-45 - SS1000-13000 - 12x13

F.3.1. Design and print parameters
Pillar diameter: 100 nm
Pillar height: 5000 nm
Slicing: 0.1 μm
Hatching: 0.02 μm
Laser Power: 15 – 20 – 25 – 30 – 35 – 40 – 45
Scanning Speed: 1000 – 3000 – 5000 – 7000 – 9000 – 11000 – 13000
Array size: 12 x 13 pillars with 8 μm spacing (100 x 100 μm)

F.3.2. Design choices
1. Made the array bigger to the size that we are probably going to use in the microfluidic chip, 100 μm x 100 μm.

2. Made the height 2x as big, to 5 μm.

3. The first print job only contained LP 15 – LP 30 and SS 1000 – SS 9000. The beginning of some trends could be spotted, regarding the low LP and low SS in relation to the amount of collapse and burns. To see if these really are trends the array was extended with three more LP (35-40-45) and two more SS (11000-13000).

F.3.3. Observations
The first job ranged from LP 15 – LP 30 and SS 1000 – SS 9000. The second job ranged from LP 25 – LP 45 and SS 5000 – SS 13000. They overlapped 6 parameter sections. The third job included all parameters. Based on these the tables were made.

A lot of difference could be seen between the print jobs. The first one contained a lot of collapsed and burned pillars, the second a lot less, and the third was by far the best. Because this first job looks like a bad job, the collapse and burn percentages are only taken from the second and third job.

Trend 1: Laser Power versus diameter/height:
With increasing LP, the diameter and height also increases. For SS 1000 the height fluctuates a bit.

Trend 2: Laser Power versus percentage collapse:
For increasing LP, less pillars collapse. From LP 30 there is (almost) no collapse anymore.

Trend 3: Laser Power versus percentage burn:
For increasing LP, more pillars burn. This starts at LP 25 and increases.

Trend 4: Scanning Speed versus diameter/height:
SS does not influence the diameter that much, but the height is fluctuating.

Trend 5: Scanning Speed versus percentage collapse:
SS does not influence the amount of collapsed pillars that much.

Trend 6: Scanning Speed versus percentage burn:
SS does not influence the amount of burned pillars that much.

F.3.4. Discussion
There is still a lot of difference between print jobs, mostly in terms of collapsing and burning. Some print jobs are definitely better than others.

	SS 1000 DmDi	hmhi	AR		SS 3000 DmDi	hmhi	AR		SS 5000 DmDi	hmhi	AR		SS 7000 DmDi	hmhi	AR		SS 9000 DmDi	hmhi	AR		SS 11000 DmDi	hmhi	AR		SS 13000 DmDi	hmhi	AR
A1: LP 15	2.641	1.130	19.252	B1: LP 15	2.540	0.926	16.400	C1: LP 15	2.341	0.882	16.958	D1: LP 15	2.323	0.960	18.606	E1: LP 15	2.344	0.887	17.037	F1: LP 15	2.752	0.844	13.807	G1: LP 15	2.754	0.886	14.477
A2: LP 20	3.817	0.946	11.158	B2: LP 20	3.004	0.931	13.951	C2: LP 20	3.198	0.924	13.004	D2: LP 20	3.399	0.952	12.598	E2: LP 20	3.509	0.918	11.776	F2: LP 20	3.810	0.931	10.998	G2: LP 20	3.649	0.911	11.237
A3: LP 25	3.674	1.087	13.317	B3: LP 25	3.864	1.018	11.854	C3: LP 25	3.973	0.958	10.845	D3: LP 25	4.084	0.996	10.971	E3: LP 25	4.163	1.002	10.835	F3: LP 25	4.252	1.012	10.707	G3: LP 25	4.364	1.029	10.613
A4: LP 30	4.653	0.980	9.476	B4: LP 30	4.573	1.038	10.218	C4: LP 30	4.524	1.020	10.145	D4: LP 30	4.598	1.051	10.291	E4: LP 30	4.666	1.050	10.129	F4: LP 30	4.837	1.061	9.871	G4: LP 30	4.867	1.063	9.831
A5: LP 35	5.049	1.080	9.629	B5: LP 35	4.940	1.107	10.087	C5: LP 35	5.137	1.120	9.811	D5: LP 35	5.017	1.090	9.779	E5: LP 35	5.074	1.094	9.706	F5: LP 35	5.416	1.087	9.030	G5: LP 35	5.282	1.103	9.400
A6: LP 40	5.451	1.166	9.623	B6: LP 40	5.522	1.122	9.139	C6: LP 40	5.401	1.163	9.694	D6: LP 40	5.611	1.124	9.011	E6: LP 40	5.472	1.109	9.119	F6: LP 40	5.569	1.130	9.132	G6: LP 40	5.674	1.136	9.011
A7: LP 45	5.610	1.145	9.184	B7: LP 45	5.782	1.134	8.828	C7: LP 45	5.702	1.079	8.514	D7: LP 45	6.257	1.103	7.932	E7: LP 45	5.837	1.151	8.870	F7: LP 45	5.837	1.168	9.002	G7: LP 45	5.930	1.125	8.534

Figure F.4: Dimensions.

		1000	3000	5000	7000	9000	11000	13000
15	Collapse	100.00%	100.00%	100.00%	100.00%	100.00%	100.00%	100.00%
	Burn	0.00%	0.00%	0.00%	0.00%	0.00%	0.00%	0.00%
20	Collapse	23.72%	18.59%	26.28%	18.59%	33.97%	11.54%	14.74%
	Burn	0.00%	0.00%	0.00%	0.00%	0.00%	0.00%	0.00%
25	Collapse	0.00%	0.00%	18.27%	8.01%	9.62%	2.56%	14.74%
	Burn	1.28%	0.00%	0.32%	1.28%	2.56%	0.96%	12.18%
30	Collapse	0.00%	0.00%	3.21%	0.96%	1.92%	0.00%	0.00%
	Burn	4.49%	0.00%	1.28%	1.28%	2.88%	1.60%	1.28%
35	Collapse	0.00%	0.00%	0.00%	0.00%	0.00%	0.00%	0.00%
	Burn	8.33%	10.26%	5.13%	5.13%	6.41%	9.94%	7.05%
40	Collapse	0.00%	0.00%	0.64%	0.00%	0.00%	0.00%	0.00%
	Burn	25.64%	14.74%	21.79%	19.87%	17.63%	26.92%	23.40%
45	Collapse	0.00%	0.00%	0.00%	0.00%	0.00%	0.00%	0.00%
	Burn	83.97%	69.23%	47.44%	50.64%	58.97%	52.56%	46.47%

Figure F.5: Amount of collapsed and burned pillars.

Around LP 30 seems to be the best region where there is not too much collapsed or burned pillars. However LP 30 also means that the diameter lies around 450 nm, which is almost twice as big as the 250 nm that is intended. To reach a diameter of around 250 nm, LP 15 has to be used.

By looking at the relations between LP and diameter, and LP and amount of collapse or burn, no good parameters exist to make a pillar that is 250 nm in diameter that does not collapse or burn. It should be investigated if printing settings can be combined within a pillar to reach al the desired properties. It is believed that a pillar with a larger base will less likely collapse, as can bee seen in the pillars made with larger LP that have a larger diameter. However the upper part of the pillar still should have the right diameter.

Based on the values in the table, we see that a diameter of 250 nm is possible when using a LP of around 15.

F.4. Data analysis: Iteration 3

Diameter100 - Height8000 - S0.1 - H0.02 - LP varying within pillar - SS1000-13000

As we do not exactly know the final diameter we get for each LP, we now speak in LP if we speak about size. For example LP 30 means a larger diameter compared to LP 15.

F.4.1. Design and print parameters

Pillar diameter: 100 nm
Pillar height: 8000 nm
Slicing: 0.1 μm
Hatching: 0.02 μm
Laser Power: varying from 30 to 10 along the pillar
Scanning Speed: 1000 - 3000 - 5000 - 7000 - 9000 - 11000 - 13000
Array size: 12 x 13 pillars with 8 μm spacing (100 x 100 μm)

F.4.2. Design choices

1. The height is again increased to 8 μm. This is the height that the final pillars should be.

2. A new code is written that can build pillars layer by layer. The code for an individual layer is written by a GUI that is created in Matlab (Figure F.6). By stacking these layers a pillar can be made and for every individual layer we can vary printing parameters like LP and SS. In this iteration we will see how varying the LP along the height of the pillar will affect its shape.

3. Different print jobs are created by printing segments of the pillars with different LP. The base is always LP 30, the intermediate segments LP 25 and LP 20 and the top is LP 10 or LP 15. The length of these segments is varied with the different experiments. The range of LP was chosen with data from previous iterations, as in this range the pillars will hopefully not burn and still have a small diameter tip.

4. The first print job made pillars where the LP is varied from LP 30 at the base to LP 10 at the top. The LP is gradually decreased from bottom to top. The second print job made pillars with four equally sized segments: LP 30, LP 25, LP 20 and LP 15. The third print job made pillars with 5 equally sized segments: LP 30, LP 30, LP 25, LP 20 and LP 15. This was done to see the effect of having a longer base made with LP 30 (2/5 against 1/4).
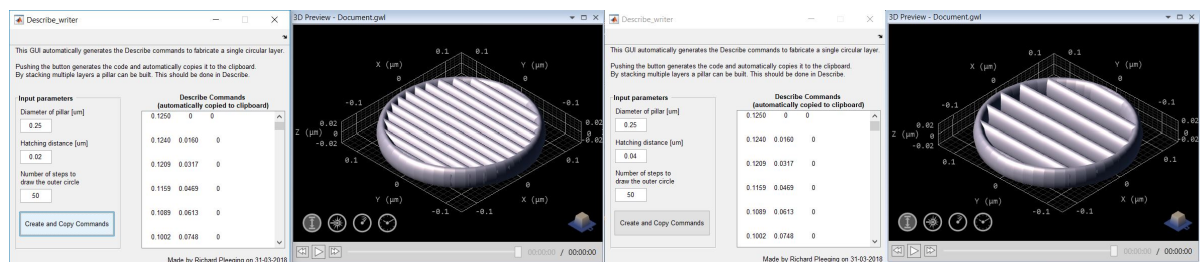
(a)   (b)

Figure F.6: GUI to write a pillar slice with the input for hatching at a) 0.02 μm and b) 0.04 μm.

F.4.3. Observations
Experiment 1: Gradual decrease from LP 30 to LP 10 and SS 1000 to SS 13000.
All pillars are collapsed.

All pillars had the same pointy shape.

Diameter at the base is around 400 nm, in the middle around 300 nm and at the tip around 150 nm.

The length is around 8 μm as it should be.

Figure F.7: Experiment 1.

Experiment 2: pillar divided into 4 segments with LP: 30, 25, 20, 15 and SS 1000 to SS 13000.
Only SS 1000 had 12 pillars standing.

All pillars look the same. However some had a very tiny string at the top, which is probably the smallest LP, that is deconnected at the other pillars.

Diameter at the base is around 400 nm, in the middle 330 and at the tip 250.

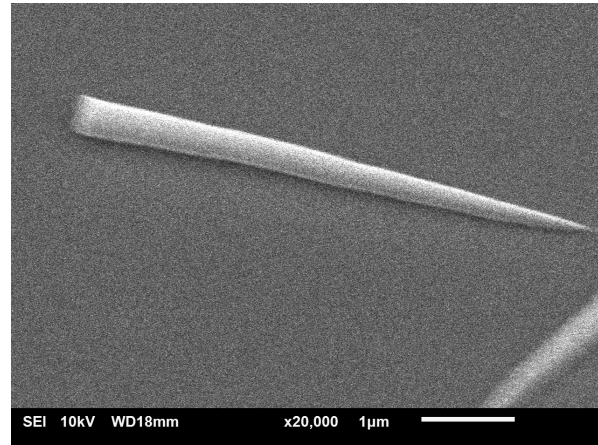The length is around 4.5 μm, so it's missing a substantial part, probably due to a loss of the small tip.
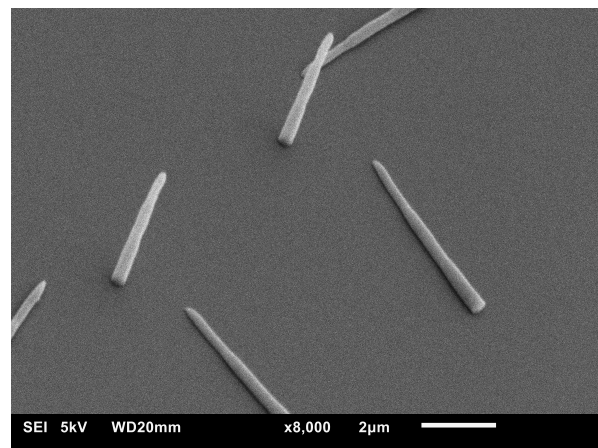
Figure F.8: Experiment 2.

Experiment 3: pillar divided into 5 segments with LP: 30, 30, 25, 20, 15 and SS 1000 to SS 13000.
SS 1000 had 88 upright pillars, SS 3000 had 2 and SS 5000 had 4. All pillars look the same.

Diameter at the base is around 450 nm, and it goes to 350 nm, 270 nm and 200 at the top.

Length is around 7.5 μm, which is about right.
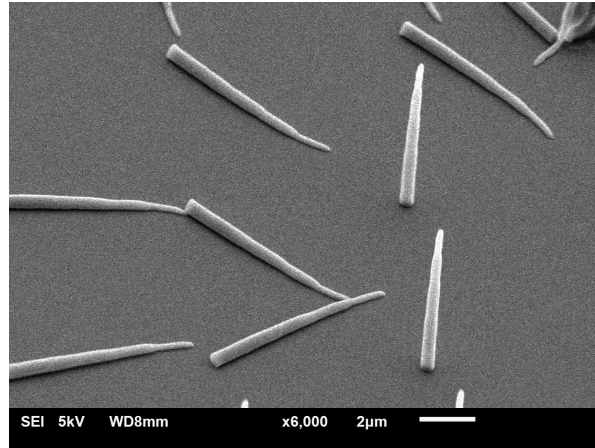
Figure F.9: Experiment 3.

F.4.4. Discussion
It is possible to vary the shape of the pillar by varying the LP along the length.

The range that we are working in (LP 30 to LP 15/10) causes no burned pillars. This was also expected when looking at the data of the previous iterations.

Experiment 3 only varies from experiment 2 by having a longer base of LP30. It can be seen by the amount of pillars that are upright that this leads to less collapse and a more stable pillar. However we want to end up with a pillar that has a diameter of 250 nm along the whole length of the pillar. Therefor we need to know what the best length of the LP 30 base is, and how long we should make the thinner top part.

SS do not seem to matter too much, but we see that most pillars that are not collapsed are in the lower SS.

F.5. Data analysis: Iteration 4

Diameter100 - Height8000 - S0.1 - H0.02 - LPbase30 - different % of pillar with LPtop15 - SS3000

F.5.1. Design and print parameters

Pillar diameter: 100 nm
Pillar height: 8000 nm
Slicing: 0.1 μm
Hatching: 0.02 μm
Laser Power: varying from 30 to 15 along the pillar
Scanning Speed: 3000
Array size: 12 x 13 pillars with 8 μm spacing (100 x 100 μm)

F.5.2. Design choices

1. To know the minimal length of base LP 30 to make the pillar not collapse, different arrays were printed. Each array contained pillars with increasing lengths of LP 15 top parts. They are named for their percentage of pillar length with LP 15 top part. As the base is LP 30, there is a region of 1/10 of the pillar that contains half LP 20 and half LP 25. For example: a 50% pillar is made of 40% LP 30, 5% LP 25 and 5% LP 20, 50% LP 15.

2. The scanning speed is not varied anymore, because previous iterations show that it does not have a significant effect. However, due to minor effects the choice is made to use SS 3000. SS 1000 sometimes did show some burned pillars, even for the lower laser powers. Also in iteration 3, SS 3000 still contained some standing pillars where the higher scanning speeds showed absolutely none.

3. The first print jobs contained pillar heights of 5 μm because additional UV-curing was tried to further cross-link the polymer and add stiffness to the material. Because less pillars collapse for a height of 5 μm than for 8 μm, it was hoped that a better distinction could be made between pillars with additional curing and pillars without. After this 8 μm high pillars were made.

F.5.3. Observations

The first two print jobs contained pillars of 5 μm in height. The first print job was a usual, the second one was given an additional UV treatment for 2 minutes in the Photopol A5406 curing unit (Brilliant Technology 3D) to add stiffness to the material [82, 121]. There seemed to be less collapsed pillars for the 0% - 40% pillars, but further there was no improvement to see between the two print jobs. A third print job was executed with pillars of 8 μm height, which appeared to be the same as the 5 μm high pillars. The difference in percentage of LP 15 could be seen very well on SEM pictures (Figures F.10, F.11, F.12). The diameter of the top part of the pillar again fluctuated, between 230 nm and 200 nm for the print job with height 5 μm and 8 μm respectively. Because we want to fabricate a pillar that is 250 nm, the laser power for the top part still has to be optimized.
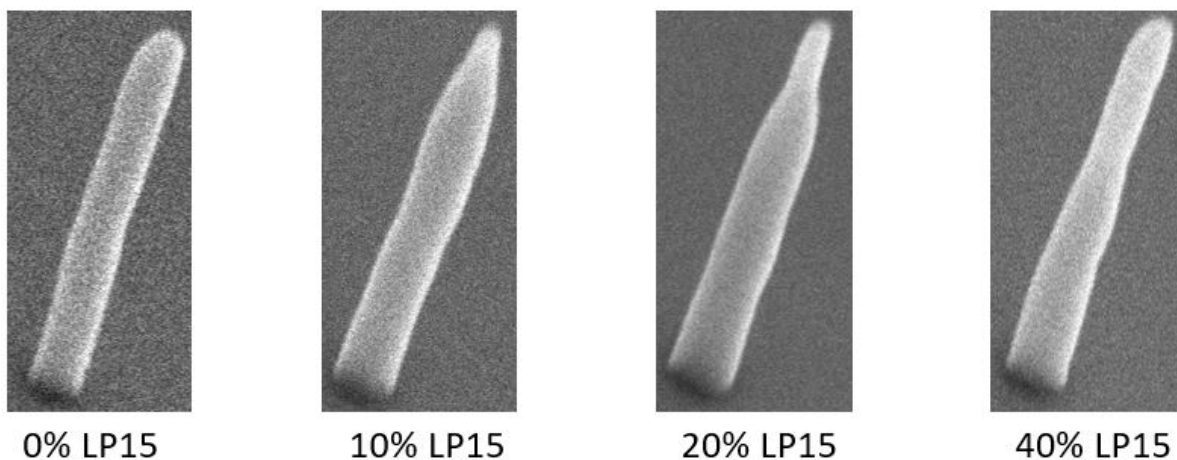
Figure F.10: 0% - 40% of pillar containing LP 15
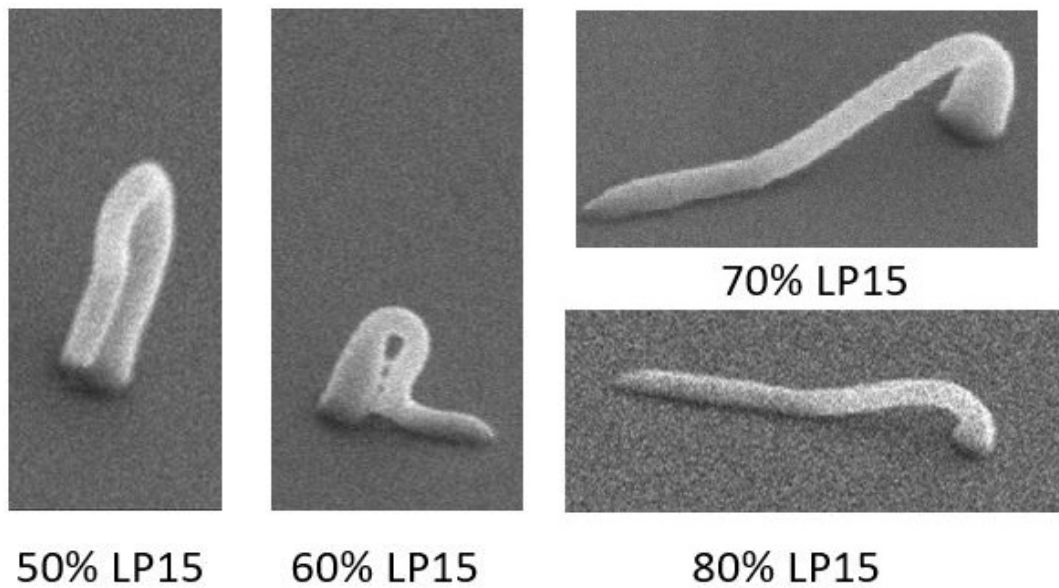
Figure F.11: 50% - 80% of pillar containing LP 15
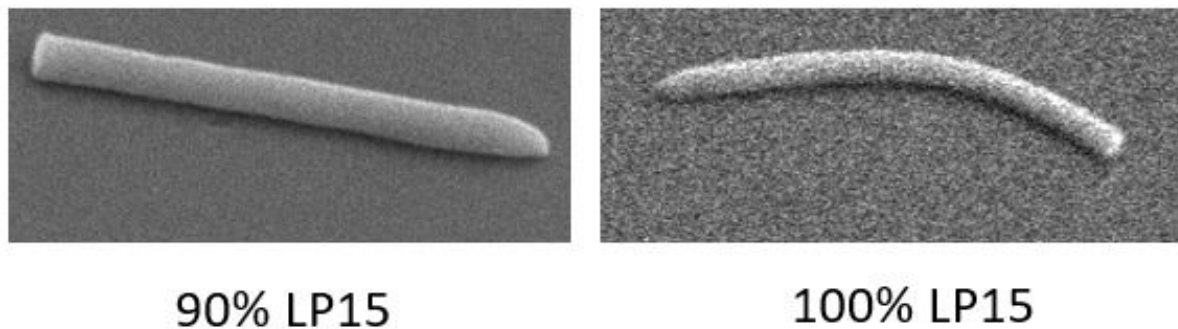
Figure F.12: 90% - 100% of pillar containing LP 15

F.5.4. Discussion

It can be seen that things get interesting from 50% LP 15 pillars. The thin upper segment bends down right at the middle of the 50% LP 15 pillar. For higher percentages of LP 15 it touches the substrate. It is seen that up until 80% LP 15 the base is still attached to the substrate. The pillars of 90% and 100% are fully collapsed and deattached from the substrate. It is interesting that pillars start to collapse from 50% LP 15 but up until 80% are still attached to the substrate.

When we look at the full arrays another interesting thing can be seen. The pillars all seem to collapse in the direction of one point. this causes to believe that the collapsing takes place during drying of the rinsing liquid. To prove this collapse due to capillary forces, the actual drying of the rinsed substrate after printing is done when looking at the pillars with an optical microscope. The liquid can be seen to evaporate, and at the liquid-air boundary it can be seen that the pillars get pulled down. After this, literature was found that supports this phenomena. In literature it is found that when making such high AR structures, there is a need for a drying method that circumvents capillary forces. One method is freeze drying, but another more common method is critical point drying (CPD). Things are set in motion to get a CPD installed. Until then, further iterations are done to get the LP exactly right to obtain a pillar with a diameter of 250 nm.

F.6. Data analysis: Iteration 5

Diameter100 - Height8000 - S0.1 - H0.02 - LPbase30 - top 80% of pillar with LP15-22

F.6.1. Design and print parameters

Pillar diameter: 100 nm
Pillar height: 8000 nm
Slicing: 0.1 μm
Hatching: 0.02 μm
Laser Power: at the base 30, top 80% 15-16-17-18-19-20-21-22
Scanning Speed: 3000
Array size: 12 x 13 pillars with 8 μm spacing (100 x 100 μm)

F.6.2. Design choices

1. To have sufficient pillar length to do diameter measurements, the pillars that were printed were from 80% upwards.

2. In previous iteration the top part of the pillars were printed with LP 15. This lead to diameters of 200-230 nm. Because we want to fabricate a pillar with a diameter of 250 nm, slightly higher LP should be used.

3. The first print job was performed with a top pillar LP 15, 16 and 17. This led to diameters ranging from 100 nm to 160 nm, which is twice as small as should be.

4. The second print job used top pillar LP 15, 16, 17, 18, 19 and 20. Still 250 nm was not reached.

5. The third print job printed the top part of the pillars with LP 18, 19, 20, 21 and 22. This time the pillars were almost right but mostly a bit too big.

F.6.3. Observations

Like all previous print jobs, per sample the dimensions really differ. The diameter increases with laser power for each print job, but the range is always different. In Figure F.13 the values for the diameter are plotted against there corresponding LP.

Because the temperature in the room seems to play a role (on a day the temperature was 28 °C and nothing printed anymore), this iteration also the temperature was noted down. Also before every print job the laser is calibrated and the maximum power scaling is noted down (Figure F.14). Still there is no explanation why the dimensions vary so much per print job.
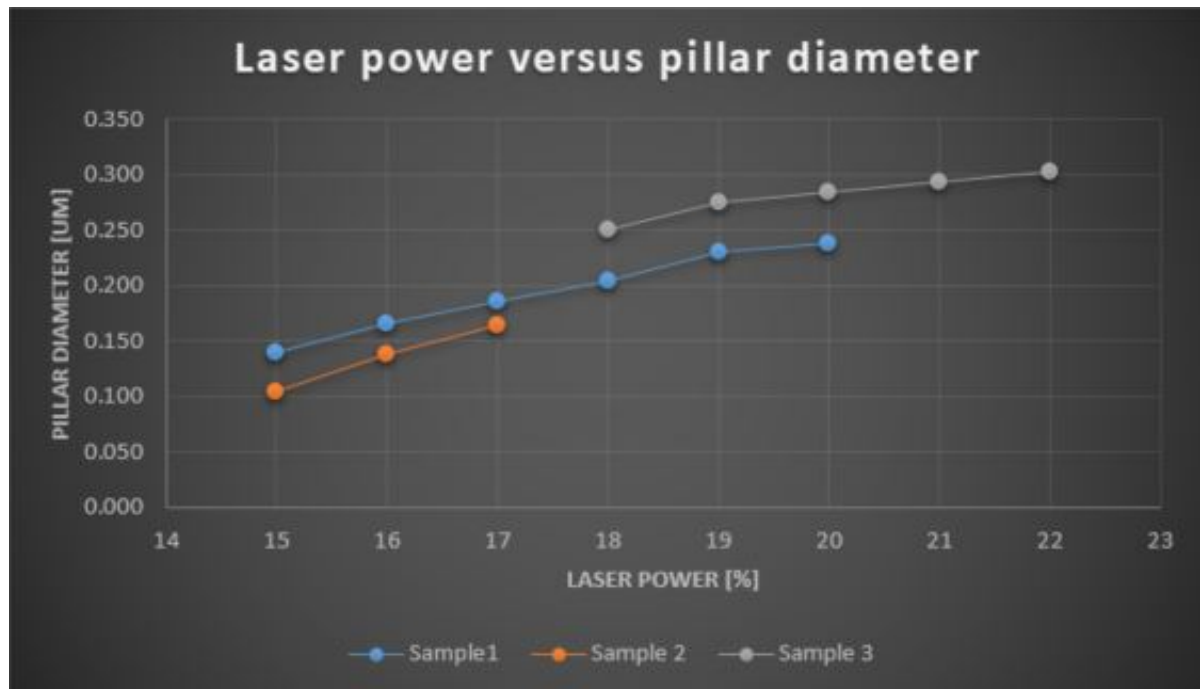
Figure F.13: Dimensions of the top with different LP.

Sample 1	Maximum Powerscaling 1.25				Temperature 20 C			
Laser Power	15	16	17	18	19	20	21	22
D pillar	0.139	0.166	0.186	0.205	0.231	0.238		

Sample 2	Maximum Powerscaling 1.23				Temperature 19 C			
Laser Power	15	16	17	18	19	20	21	22
D pillar	0.105	0.139	0.164					

Sample 3	Maximum Powerscaling 1.25				Temperature 20 C			
Laser Power	15	16	17	18	19	20	21	22
D pillar				0.251	0.275	0.284	0.293	0.302

Figure F.14: Dimensions of the top with different LP.

Appendix G

Kidney Stone Types

In this appendix a short description of the different types of kidney stones can be found, with the information obtained from [26].

Calcium stones

Within the range of calcium kidney stones, two different crystals can be found.

1) Calcium oxalate crystal forms out of calcium and oxalic acid. It comes in two forms, calcium oxalate monohydrate (COM) and calcium oxalate dihydrate (COD). With high levels of oxalate in the urine, COM forms more often and is mechanically harder than COD, which makes it more resistant to lithotripsy, the medical procedure in which it is tried to pulverize stones. There are different causes for the formation of calcium oxalate stones, categorized into systemic diseases and apparently spontaneous (idiopathic).

2) Calcium phosphate crystal forms out of calcium and phosphoric acid. With this crystal the acidity of the urine is important. Phosphate in an aqueous solution can exist in different forms, depending on the acidity of the solution. In normal urine, the pH is around 6, and the dihydrogen phosphate ion is most common, leaving the ion with a minus 1 charge. This is not enough to form a crystal with the calcium ion having a plus 2 charge. But when the urine gets more alkaline, the phosphate ion exists in its hydrogen phosphate form, leaving it a charge of minus 2 and making it possible to bond with a calcium ion. So these crystals form in persons with a more alkaline urine than normal. When one phosphate ion bonds to one calcium ion, the crystal is called brushite (BR). This can convert to hydroxyapatite (HA), having two phosphate ions to one calcium ion. Also here there can be different causes: crystals forming due to systemic diseases and idiopathic stone forming.

Struvite stones

Struvite is a magnesium ammonium phosphate and it can not be produced by the body itself. Ammonia-producing bacteria do. These bacteria usually live in the soil, where they transform the urea excreted from mammalian animals into usable substances for plants. As we are mammals as well, our urine contains a lot of urine. Those soil bacteria can get into the urinary tract, where they produce struvite crystals. Those crystals in turn form struvite stones.

Uric Acid stones

Uric acid (UA) is a metabolic breakdown product of DNA and RNA. It does not need another atom to form a crystal. It all depends on the acidity of the urine it resides in. In urine with a neutral or high pH, urate will have a minus one or minus two charge respectively. This makes it soluble in water. But in an acidic solution, both charge sites of urate are occupied leaving the ion with a zero charge, making it insoluble. This type of stone is thus almost completely dependent on the acidity of the urine, which makes it a typical stone for people suffering from certain diseases.

Cystine stones

Cystine is the product of two cysteine amino acids bonded together. Cysteine on its own is very soluble because it has a negative charge. But when two are bonded together, there is no net charge on the molecule and cystine crystallizes out of the solution. This type of stone only forms in people with cystinuria, a genetic kidney disease. This disease causes certain amino acids, among which cysteine, to enter the urine in huge amounts.

Other stones

There are also rare substances that can crystallize and form stones in the kidneys. These usually involve stones formed in people with certain diseases, stones formed from crystallized anti-viral drugs or stones formed due to rare metabolism diseases.

Bibliography

[1] Victoriano Romero, Haluk Akpinar, and Dean G Assimos. Kidney stones: a global picture of prevalence, incidence, and associated risk factors. *Reviews in urology*, 12(2-3):e86–96, 2010.

[2] Elaine M Worcester and Fredric L Coe. Calcium Kidney Stones. *The New England Journal of Medicine*, 36310363(2):954–63, 2010.

[3] Christopher S Saigal and Geoffrey Joyce. Direct and indirect costs of nephrolithiasis in an employed population: Opportunity for disease management? *Kidney International*, 68:1808–1814, 2005.

[4] J. Shah and H. N. Whitfield. Urolithiasis through the ages. *BJU International*, 89(8):801–810, 2002.

[5] Ahmet Tefekli and Fatin Cezayirli. The history of urinary stones: in parallel with civilization. *TheScientificWorldJournal*, 2013:423964, nov 2013.

[6] Dongeun Huh, Yu-suke Torisawa, Geraldine A. Hamilton, Hyun Jung Kim, and Donald E. Ingber. Microengineered physiological biomimicry: Organs-on-Chips. *Lab on a Chip*, 12(12):2156, 2012.

[7] Anke Hoppensack, Christian C. Kazanecki, David Colter, Anna Gosiewska, Johanna Schanz, Heike Walles, and Katja Schenke-Layland. A Human In Vitro Model That Mimics the Renal Proximal Tubule. *Tissue Engineering Part C: Methods*, 20(7):599–609, 2014.

[8] Kyung-Jin Jang, Ali Poyan Mehr, Geraldine A. Hamilton, Lori A. McPartlin, Seyoon Chung, Kahp-Yang Suh, and Donald E. Ingber. Human kidney proximal tubule-on-a-chip for drug transport and nephrotoxicity assessment. *Integrative Biology*, 5(9):1119, aug 2013.

[9] Ryan D Sochol, Navin R Gupta, and Joseph V Bonventre. A Role for 3D Printing in Kidney-on-a-Chip Platforms. *Current Transplantation Reports*, 3(1):82–92, mar 2016.

[10] Ying Diao, Allan S. Myerson, T. Alan Hatton, and Bernhardt L. Trout. Surface design for controlled crystallization: The role of surface chemistry and nanoscale pores in heterogeneous nucleation. *Langmuir*, 27(9):5324–5334, 2011.

[11] Ying Diao, Takuya Harada, Allan S. Myerson, T. Alan Hatton, and Bernhardt L. Trout. The role of nanopore shape in surface-induced crystallization. *Nature Materials*, 10(11):867–871, 2011.

[12] Saladin. *Anatomy and Physiology: The Unity of Form and Function.* McGraw-Hill, 5th edition, 2009.

[13] T Lazar. Histology and Cell Biology: An Introduction to Pathology. *Tissue and Cell*, 34(6):5–8, dec 2002.

[14] Zhaopeng Du, Yi Duan, QingShang Yan, Alan M Weinstein, Sheldon Weinbaum, and Tong Wang. Mechanosensory function of microvilli of the kidney proximal tubule. *Proceedings of the National Academy of Sciences of the United States of America*, 101(35):13068–73, aug 2004.

[15] Q. Zhang. Cystic Kidney Diseases: All Roads Lead to the Cilium. *Physiology*, 19(4):225–230, 2004.

[16] Harald Hücker, Hartmut Frenzel, and Dieter Skoluda. Scanning electron microscopy of the distal nephron and calyx of the human kidney. *Virchows Archiv B Cell Pathology*, 18(1):157–164, 1975.

[17] P Guo, A. M Weinstein, and S Weinbaum. A hydrodynamic mechanosensory hypothesis for brush border microvilli. *Am J Physiol Renal Physiol*, 279:F698–F712, 2000.

[18] H. Kojima, A. Ishijima, and T. Yanagida. Direct measurement of stiffness of single actin filaments with and without tropomyosin by in vitro nanomanipulation. *Proceedings of the National Academy of Sciences*, 91(26):12962–12966, 1994.

[19] Cécile Sauvanet, Jessica Wayt, Thaher Pelaseyed, and Anthony Bretscher. Structure, Regulation, and Functional Diversity of Microvilli on the Apical Domain of Epithelial Cells. *Annu. Rev. Cell Dev. Biol*, 31: 593–621, 2015.

[20] Mahito Kikumoto, Masashi Kurachi, Valer Tosa, and Hideo Tashiro. Flexural Rigidity of Individual Microtubules Measured by a Buckling Force with Optical Traps. *Biophysical Journal*, 90(5):1687–1696, 2006.

[21] David B. Wells and Aleksei Aksimentiev. Mechanical properties of a complete microtubule revealed through molecular dynamics simulation. *Biophysical Journal*, 99(2):629–637, 2010.

[22] F Oster, D Murray, and M Odell. the Formation of Microvilli. *UCLA Symposium Series: Animal Forms*, 1985.

[23] Hiroshi Sakaguchi and Yasunosuke Suzuki. Fine structure of renal tubule cells. *Keio Journal of Medicine*, 7, 1958.

[24] S Weinbaum, P Guo, and L You. A new view of mechanotransduction and strain amplification in cells with microvilli and cell processes. *Biorheology*, 38(2-3):119–142, 2001.

[25] Julia Gorelik, Andrew I Shevchuk, Gregory I Frolenkov, Ivan A Diakonov, Max J Lab, Corne J Kros, Guy P Richardson, Igor Vodyanoy, Christopher R W Edwards, David Klenerman, and Yuri E Korchev. Dynamic assembly of surface structures in living cells. *Proceedings of the National Academy of Sciences of the United States of America*, 100(10):5819–22, may 2003.

[26] Fredric L Coe. Types of Kidney Stones: a Primer, 2016.

[27] Adriano Ramello, Corrado Vitale, and Martino Marangella. Epidemiology of Nephrolithiasis. *Primer on the Metabolic Bone Diseases and Disorders of Mineral Metabolism: Eighth Edition*, 13 Suppl 3:856–859, 2000.

[28] W.G Robertson and M Peacock. Calcium Oxalate Crystalluria and Inhibitors of Crystallization in Recurrent Renal Stone-Formers. *Clinical Science*, 43:499–506, 1972.

[29] Dik J. Kok, Jolein A. Iestra, Cornelius J. Doorenbos, and Socrates E. Papapoulos. The Effects of Dietary Excesses in Animal Protein and Sodium on the Composition and the Crystallization Kinetics of Calcium Oxalate Monohydrate in Urines of Healthy Men. *Journal of Clinical Endocrinology and Metabolism*, 71 (4):861–867, oct 1990.

[30] W.G. Robertson. Kidney Models of Calcium Oxalate Stone Formation. *Nephron Physiology*, 98(2):p21–p30, 2004.

[31] Dirk J Kok and Saeed R Khan. Calcium oxalate nephrolithiasis, a free or fixed particle disease. *Kidney International*, 46:847–854, 1994.

[32] C.F Verkoelen and A Verhulst. Proposed mechanisms in renal tubular crystal retention. *Kidney International*, 72(1):13–18, jul 2007.

[33] Andrew P Evan, James E Lingeman, Fredric L Coe, Joan H Parks, Sharon B Bledsoe, Youzhi Shao, Andre J Sommer, Ryan F Paterson, Ramsay L Kuo, and Marc Grynpas. Randall's plaque of patients with nephrolithiasis begins in basement membranes of thin loops of Henle. *Journal of Clinical Investigation*, 2003.

[34] Andrew P Evan. Histopathology predicts the mechanism of stone formation. *AIP Conf Proc of Ann Int Urolithiasis Research Symposium*, 900:15–25, 2007.

[35] Alexander Randall. the Origin and Growth of Renal Calculi. *Annals of surgery*, 105(6):1009–1027, jun 1937.

[36] A. Randall. The etiology of primary renal calculus. *International Abstract of Surgery*, 71:209–240, 1940.

[37] Alexander Randall. Papillary Pathology as a Precursor of Primary Renal Calculus 1 1Read at the American Urological Association in Buffalo, N. Y. on June 25, 1940. *The Journal of Urology*, 44(5):580–589, nov 1940.

[38] R K Low and M L Stoller. Endoscopic mapping of renal papillae for Randall's plaques in patients with urinary stone disease. *The Journal of urology*, 158(6):2062–4, dec 1997.

[39] Nicole L Miller, Daniel L Gillen, James C Williams, Andrew P Evan, Sharon B Bledsoe, Fredric L Coe, Elaine M Worcester, Brian R Matlaga, Larry C Munch, and James E Lingeman. A formal test of the hypothesis that idiopathic calcium oxalate stones grow on Randall's plaque. *BJU international*, 103(7): 966–71, apr 2009.

[40] Nicole L Miller, James C Williams, Andrew P Evan, Sharon B Bledsoe, Fredric L Coe, Elaine M Worcester, Larry C Munch, Shelly E Handa, and James E Lingeman. In idiopathic calcium oxalate stone-formers, unattached stones show evidence of having originated as attached stones on Randall's plaque. *BJU international*, 105(2):242–5, jan 2010.

[41] D Turnbull. Kinetics of Heterogeneous Nucleation. *The Journal of Chemical Physics*, 18(36):198–1103, 1950.

[42] Michael Ashby, Hugh Shercliff, and David Cebon. *Engineering , Science , Processing and Design*. Butterworth-Heinemann, 2010.

[43] Byron D. Gates, Qiaobing Xu, Michael Stewart, Declan Ryan, C. Grant Willson, and George M. Whitesides. New approaches to nanofabrication: Molding, printing, and other techniques. *Chemical Reviews*, 105(4):1171–1196, 2005.

[44] Aránzazu del Campo and Eduard Arzt. Fabrication approaches for generating complex micro- and nanopatterns on polymeric surfaces. *Chemical Reviews*, 108(3):911–945, 2008.

[45] Peter X. Ma. Biomimetic materials for tissue engineering. *Advanced Drug Delivery Reviews*, 60(2):184–198, 2008.

[46] Holger Becker and Claudia Gärtner. Polymer microfabrication technologies for microfluidic systems. *Analytical and Bioanalytical Chemistry*, 390(1):89–111, 2008.

[47] Chaoqun Zhang, Daniel A. Mcadams, and Jaime C. Grunlan. Nano/Micro-Manufacturing of Bioinspired Materials: a Review of Methods to Mimic Natural Structures. *Advanced Materials*, 28(39):8566, 2016.

[48] G. Laffite, C. Leroy, C. Bonhomme, L. Bonhomme-Coury, E. Letavernier, M. Daudon, V. Frochot, J. P. Haymann, S. Rouzière, I. T. Lucas, D. Bazin, F. Babonneau, and A. Abou-Hassan. Calcium oxalate precipitation by diffusion using laminar microfluidics: toward a biomimetic model of pathological microcalcifications. *Lab Chip*, 16(7):1157–1160, 2016.

[49] Cesare de Martino, Carmelo B. Bruni, Marinella Bellocci, and Pier Giorgio Natali. Spontaneous leptospiral infection of the rat kidney. An ultrastructural study. *Experimental and Molecular Pathology*, 10 (1):27–38, feb 1969.

[50] M A Venkatachalam, D B Jones, H G Rennke, D Sandstrom, and Y Patel. Mechanism of proximal tubule brush border loss and regeneration following mild renal ischemia. *Laboratory investigation; a journal of technical methods and pathology*, 45(4):355–65, oct 1981.

[51] J C Møller, E Skriver, S Olsen, and A B Maunsbach. Ultrastructural analysis of human proximal tubules and cortical interstitium in chronic renal disease (hydronephrosis). *Virchows Archiv. A, Pathological anatomy and histopathology*, 402(3):209–37, 1984.

[52] T. Steen Olsen, N. F. Wassef, H. Steen Olsen, and H. E. Hansen. Ultrastructure of the Kidney in Acute Interstitial Nephritis. *Ultrastructural Pathology*, 10(1):1–16, jan 1986.

[53] Kai Sandvold Beckwith, Simon P. Cooil, Justin W. Wells, and Pawel Sikorski. Tunable high aspect ratio polymer nanostructures for cell interfaces. *Nanoscale*, 7(18):8438–8450, apr 2015.

[54] H. Masuda and K. Fukuda. Ordered Metal Nanohole Arrays Made by a Two-Step Replication of Honey-comb Structures of Anodic Alumina. *Science*, 268(5216):1466–1468, 1995.

[55] Hideki Masuda, Kouichi Yada, and Atsushi Osaka. Self-ordering of cell configuration of anodic porous alumina with large-size pores in phosphoric acid solution. *Japanese Journal of Applied Physics, Part 2: Letters*, 37(11 PART A):9–12, 1998.

[56] Johnson Matthey and Ward Hill. Cellular growth of highly ordered porous anodic ® lms on aluminium. *Journal of Materials science letters*, 7(2):291–294, 1998.

[57] Moon Kee Choi, Hyunsik Yoon, Kyunghee Lee, and Kyusoon Shin. Simple Fabrication of Asymmetric High-Aspect-Ratio Polymer Nanopillars by Reusable AAO Templates. *Langmuir*, 27(6):2132–2137, mar 2011.

[58] Woo Kyung Cho and Insung S. Choi. Fabrication of hairy polymeric films inspired by Geckos: Wetting and high adhesion properties. *Advanced Functional Materials*, 18(7):1089–1096, 2008.

[59] Y Li, H W Ng, B D Gates, and C Menon. Material versatility using replica molding for large- scale fabrica-tion of high aspect-ratio, high density arrays of nano-pillars Enhancement of the thermo-mechanical properties of PDMS molds for the hot embossing of PMMA microfluidic devices Material ver. *Nan-otechnology*, 25(285303), 2014.

[60] Ying Zhang, Chi Wei Lo, J. Ashley Taylor, and Shu Yang. Replica molding of high-aspect-ratio polymeric nanopillar arrays with high fidelity. *Langmuir*, 22(20):8595–8601, 2006.

[61] Mukti Aryal, Fatih Buyukserin, Kamil Mielczarek, Xiao-Mei Zhao, Jinming Gao, Anvar Zakhidov, and Wenchuang (Walter) Hu. Imprinted large-scale high density polymer nanopillars for organic solar cells. *Journal of Vacuum Science & Technology B: Microelectronics and Nanometer Structures*, 26(6): 2562–2566, 2008.

[62] W. Chen, Z. Diao, J. H. Dirks, F. Geiger, and J. Spatz. Enhanced Optical Transmittance by Reduced Reflectance of Curved Polymer Surfaces. *Macromolecular Materials and Engineering*, 302(9):1700072, sep 2017.

[63] Kyoung Je Cha, Jung Min Hong, Dong Woo Cho, and Dong Sung Kim. Enhanced osteogenic fate and function of MC3T3-E1 cells on nanoengineered polystyrene surfaces with nanopillar and nanopore arrays. *Biofabrication*, 5(2):25007–12, 2013.

[64] Chiung Wen Kuo, Jau Ye Shiu, Fan Ching Chien, Shih Min Tsai, Di Yan Chueh, and Peilin Chen. Poly-meric nanopillar arrays for cell traction force measurements. *Electrophoresis*, 31(18):3152–3158, aug 2010.

[65] Weitao Jiang, Biao Lei, Hongzhong Liu, Dong Niu, Tingting Zhao, Bangdao Chen, Lei Yin, Yongsheng Shi, and Xiaokang Liu. Fabrication of directional nanopillars with high-aspect-ratio using a stretching imprint process with a microcavity mold. *Nanoscale*, 9(6):2172–2177, 2017.

[66] Cholho Lee, Kyung-Hoon Han, Kwon-Hyeon Kim, and Jang-Joo Kim. Direct formation of nano-pillar arrays by phase separation of polymer blend for the enhanced out-coupling of organic light emitting diodes with low pixel blurring. *Optics Express*, 24(6):A488, 2016.

[67] Nina Buch-Månson, Arnaud Spangenberg, Laura Piedad Chia Gomez, Jean Pierre Malval, Olivier Sop-pera, and Karen L. Martinez. Rapid prototyping of polymeric nanopillars by 3D direct laser writing for controlling cell behavior. *Scientific Reports*, 7(1):9247, aug 2017.

[68] Kwang Sup Lee, Ran Hee Kim, Dong Yol Yang, and Sang Hu Park. Advances in 3D nano/microfabrication using two-photon initiated polymerization. *Progress in Polymer Science (Ox-ford)*, 33(6):631–681, 2008.

[69] Michael Röhrig, Michael Thiel, Matthias Worgull, and Hendrik Hölscher. 3D Direct laser writing of nano- and microstructured hierarchical gecko-mimicking surfaces. *Small*, 8(19):3009–3015, oct 2012.

[70] Christopher N. LaFratta and Tommaso Baldacchini. Two-photon polymerization metrology: Characterization methods of mechanisms and microstructures. *Micromachines*, 8(4):101, mar 2017.

[71] Xin Q. Brown, Keiko Ookawa, and Joyce Y. Wong. Evaluation of polydimethylsiloxane scaffolds with physiologically-relevant elastic moduli: Interplay of substrate mechanics and surface chemistry effects on vascular smooth muscle cell response. *Biomaterials*, 26(16):3123–3129, 2005.

[72] H. Schmid and B. Michel. Siloxane polymers for high-resolution, high-accuracy soft lithography. *Macromolecules*, 33(8):3042–3049, 2000.

[73] Jiali Gao, Le Guan, and Jinkui Chu. Determining the Young's modulus of SU-8 negative photoresist through tensile testing for MEMS applications. *Proc. SPIE 7544, Sixth International Symposium on Precision Engineering Measurements and Instrumentation*, 7544:754464–754467, 2010.

[74] Enrico Domenico Lemma, Francesco Rizzi, Tommaso Dattoma, Barbara Spagnolo, Leonardo Sileo, Antonio Qualtieri, Massimo De Vittorio, and Ferruccio Pisanello. Mechanical Properties Tunability of Three-Dimensional Polymeric Structures in Two-Photon Lithography. *IEEE Transactions on Nanotechnology*, 16(1):23–31, 2017.

[75] Yusuf Yagci, Steffen Jockusch, and Nicholas J Turro. Photoinitiated polymerization: Advances, challenges, and opportunities. *Macromolecules*, 43(15):6245–6260, 2010.

[76] Shoji Maruo, Osamu Nakamura, and Satoshi Kawata. Three-dimensional microfabrication with two-photon-absorbed photopolymerization. *Optics Letters*, 22(2):132, 1997.

[77] Kwang Sup Lee, Dong Yol Yang, Sang Hu Park, and Ran Hee Kim. Recent developments in the use of two-photon polymerization in precise 2D and 3D microfabrications. *Polymers for Advanced Technologies*, 17(2):72–82, 2006.

[78] Maria Göppert-Mayer. Über Elementarakte mit zwei Quantensprüngen. *Annalen der Physik*, 401(3): 273–294, jan 1931.

[79] Nanoscribe GmbH and Fabian Kohler. 3D micro-printing by Direct Laser Writing; General introduction and application examples, 2017.

[80] Nanoscribe GmbH. Safety Data Sheet IP-L 780 Photoresist. Technical report, Nanoscribe GmbH, 2014.

[81] Samuel Clark Ligon, Robert Liska, Jürgen Stampfl, Matthias Gurr, and Rolf Mülhaupt. Polymers for 3D Printing and Customized Additive Manufacturing. *Chemical Reviews*, 117(15):10212–10290, aug 2017.

[82] J.S. Oakdale, J Ye, W Smith, and J Biener. A post-print UV curing method for improving the mechanical properties of prototypes derived from two-photon polymerization. *Optics Express*, 24(24):27077–27086, 2016.

[83] Jonathan B. Mueller, Joachim Fischer, Frederik Mayer, Muamer Kadic, and Martin Wegener. Polymerization Kinetics in Three-Dimensional Direct Laser Writing. *Advanced Materials*, 26(38):6566–6571, 2014.

[84] J. Heitz, C. Plamadeala, M. Wiesbauer, P. Freudenthaler, R. Wollhofen, J. Jacak, T. A. Klar, B. Magnus, D. Köstner, A. Weth, W. Baumgartner, and R. Marksteiner. Bone-forming cells with pronounced spread into the third dimension in polymer scaffolds fabricated by two-photon polymerization. *Journal of Biomedical Materials Research - Part A*, 105(3):891–899, 2017.

[85] Kwang-Sup Lee, Dong-Yol Yang, Sang Hu Park, and Ran Hee Kim. Recent developments in the use of two-photon polymerization in precise 2D and 3D microfabrications. *Polymers for Advanced Technologies*, 17(2):72–82, feb 2006.

[86] PubChem Open Chemistry Database. Pentaerythrityl triacrylate, 2018. URL `https://pubchem.ncbi.nlm.nih.gov/compound/19042{#}section=Top`.

[87] PubChem Open Chemistry Database. 7-Diethylamino-3-thenoylcoumarin, 2018. URL `https://pubchem.ncbi.nlm.nih.gov/compound/342536{#}section=Top`.

[88] Lieng-Huang. Lee. *Adhesive Chemistry : Developments and Trends.* Springer US, 1985.

[89] Andréa Azevedo Lazarin, Ana Lucia Machado, Camila Andrade Zamperini, Amanda Fucci Wady, Denise Madalena Palomari Spolidorio, and Carlos Eduardo Vergani. Effect of experimental photopolymer- ized coatings on the hydrophobicity of a denture base acrylic resin and on Candida albicans adhesion. *Archives of Oral Biology*, 58(1):1–9, jan 2013.

[90] J. Serbin, A. Egbert, A. Ostendorf, B. N. Chichkov, R. Houbertz, G. Domann, J. Schulz, C. Cronauer, L. Fröhlich, and M. Popall. Femtosecond laser-induced two-photon polymerization of inor- ganic–organic hybrid materials for applications in photonics. *Optics Letters*, 28(5):301, mar 2003.

[91] Xiaoqin Zhou, Yihong Hou, and Jieqiong Lin. A review on the processing accuracy of two-photon poly- merization. *Citation: AIP Advances*, 5:30701, 2015.

[92] Bo Tan, Krishnan Venkatakrishnan, and Alexander Makaronets. Effects of pulsewidth on two-photon polymerization. *Designed Monomers and Polymers*, 16(2):145–150, 2013.

[93] Daniel S., Leonardo De, Adriano J. G. Otuka, Vinicius Tribuzi, and Cleber R. Two-Photon Polymerization Fabrication of Doped Microstructures. In *Polymerization*. InTech, sep 2012.

[94] Nanoscribe GmbH. User Manual Photonic Professional GT, 2015.

[95] Federico Bella, Elena Daniela Ozzello, Stefano Bianco, and Roberta Bongiovanni. Photo- polymerization of acrylic/methacrylic gel–polymer electrolyte membranes for dye-sensitized solar cells. *Chemical Engineering Journal*, 225:873–879, jun 2013.

[96] G Odian. *Principles of Polymerization.* John Wiley & Sons, Inc., 3rd editio edition, 1991.

[97] C Decker. Laser-induced curing of functional polymers. *Designed Monomers and Polymers*, 1(1):47–64, 1998.

[98] Laura Folkertsma, Kaihuan Zhang, Mark A Hempenius, G Julius Vancso, Albert Van Den Berg, and Mathieu Odijk. Comparison of three types of redox active polymer for two photon stereolithography. *Polymers for Advanced Technologies*, 2017(December 2016):28–31, 2017.

[99] N J Glassmaker, A Jagota, C.-Y Hui, and J Kim. Design of biomimetic fibrillar interfaces: 1. Making contact. *J. R. Soc. Interface*, 1:23–33, 2004.

[100] Dinesh Chandra and Shu Yang. Stability of high-aspect-ratio micropillar arrays against adhesive and capillary forces. *Accounts of Chemical Research*, 43(8):1080–1091, 2010.

[101] Pere Roca-Cusachs, Félix Rico, Elena Martínez, Jordi Toset, Ramon Farré, and Daniel Navajas. Stability of microfabricated high aspect ratio structures in poly(dimethylsiloxane). *Langmuir*, 21(12):5542–5548, 2005.

[102] Dinesh Chandra. *Capillary Force in High Aspect-Ratio Micropillar Arrays.* PhD thesis, University of Pennsylvania, 2009.

[103] H. El-Shall, Jin-hwan Jeon, E. A. Abdel-Aal, S. Khan, L. Gower, and Y. Rabinovich. A study of primary nu- cleation of calcium oxalate monohydrate: I-Effect of supersaturation. *Crystal Research and Technology*, 39(3):214–221, 2004.

[104] Walter P. Hartl, Helmut Klapper, Bruno Barbier, Hans Jürgen Ensikat, Richard Dronskowski, Paul Müller, Gertrud Ostendorp, Alan Tye, Ralf Bauer, and Wilhelm Barthlott. Diversity of calcium oxalate crystals in Cactaceae. *Canadian Journal of Botany*, 85(5):501–517, 2007.

[105] Quorum Technologies. *Technical Brief - Critical Point Drying.* Quorum Technologies, 2 edition, 2009.

[106] Justina A. Molzon, Joan M. Lausier, and Anthony N. Paruta. Solubility of Calcium Oxalate in 1-Alkanols and Ethanol-Water Mixtures. *Journal of Pharmaceutical Sciences*, 67(5):733–735, may 1978.

[107] H. G. O. Backer. Fabian, J., Hartmann, H.: Light Absorption of Organic Colorants-Theoretical Treatment and Empirical Rules. 245 S., 76 Abb., 48 Tab., Berlin-Heidelberg-New York: Springer-Verlag. 1980. (Reactivity and Structure - Concepts in Organic Chemistry 12) Leinen, 1. *Journal für Praktische Chemie*, 324(2):350–351, 1982.

[108] Hardo Siegel and Manfred Eggersdorfer. Ketones. *Ullmann's Encyclopedia of Industrial Chemistry*, 2000.

[109] A Ravve. Chemistry of photocurable Compositions. Technical report, Springer, 2006.

[110] B. L. Van Der Waerden. *Sources of Quantum Mechanics*. North-Holland Publishing Co., Amsterdam, 1967.

[111] Gwilym Williams, Matthew Hunt, Benedikt Boehm, Andrew May, Michael Taverne, Daniel Ho, Sean Giblin, Dan Read, John Rarity, Rolf Allenspach, and Sam Ladak. Two-photon lithography for 3D magnetic nanostructure fabrication. *Nano Research*, pages 1–10, jul 2017.

[112] Kwang-sup Lee, Prem Prabhakaran, Jinsoon Park, Ran Hee Kim, Namchul Cho, Dong-yol Yang, Sang Hu Park, Tae Woo Lim, and Son Yong. Recent Advances in Two-Photon Lithography. 2014.

[113] Wee Shong. Chin, Chorng Haur. Sow, and Andrew T. S. Wee. *Science at the nanoscale : an introductory textbook*. Pan Stanford Publishing, 2010.

[114] James Thomson. The Continuity of the Gaseous and Liquid States of Matter. *Nature*, 1870.

[115] Michael J. Moran, Howard N. Saphiro, Daiisie D. Boettner, and Margaret B. Bailey. *Fundamentals of Engineering Thermodynamics*. Butterworth-Heinemann, 2011.

[116] Quorum Technologies. K850 Critical Point Drier Instruction Manual, 2012.

[117] Appendix A-1: CO2 thermodynamics | Global CCS Institute, 2018. URL `https://hub.globalccsinstitute.com/publications/co2-liquid-logistics-shipping-concept-llsc-\T1\textendash-business-model-report/appendix-1-co2`.

[118] The Liquefaction of Gases – Part II | carnotcycle, 2018. URL `https://carnotcycle.wordpress.com/2014/03/04/the-liquefaction-of-gases-part-ii/`.

[119] Technobis. Crystal16 - Crystallization Systems, . URL `https://www.crystallizationsystems.com/crystal16`.

[120] Technobis. Crystalline - Crystallization Systems, . URL `https://www.crystallizationsystems.com/Crystalline`.

[121] Julia Purtov, Andreas Verch, Peter Rogin, and René Hensel. Improved development procedure to enhance the stability of microstructures created by two-photon polymerization. *Microelectronic Engineering*, 194:45–50, jul 2018.